EXPERIMENTS AND MODEL DEVELOPMENT OF A DUAL MODE, TURBULENT JET IGNITION ENGINE

By

Sedigheh Tolou

A DISSERTATION

Submitted to
Michigan State University
in partial fulfillment of the requirements
for the degree of

Mechanical Engineering—Doctor of Philosophy

2019

ABSTRACT

EXPERIMENTS AND MODEL DEVELOPMENT OF A DUAL MODE, TURBULENT JET IGNITION ENGINE

By

Sedigheh Tolou

The number of vehicles powered by a source of energy other than traditional petroleum fuels will increase as time passes. However, based on current predictions, vehicles run on liquid fuels will be the major source of transportation for decades to come. Advanced combustion technologies can improve fuel economy of internal combustion (IC) engines and reduce exhaust emissions. The Dual Mode, Turbulent Jet Ignition (DM-TJI) system is an advanced, distributed combustion technology which can achieve high diesel-like thermal efficiencies at medium to high loads and potentially exceed diesel efficiencies at low-load operating conditions. The DM-TJI strategy extends the mixture flammability limits by igniting lean and/or highly dilute mixtures, leading to low-temperature combustion (LTC) modes in spark ignition (SI) engines.

A novel, reduced order, and physics-based model was developed to predict the behavior of a DM-TJI engine with a pre-chamber air valve assembly. The engine model developed was calibrated based on experimental data from a Prototype II DM-TJI engine. This engine was designed, built, and tested at the MSU Energy and Automotive Research Laboratory (EARL).

A predictive, generalized model was introduced to obtain a complete engine fuel map for the DM-TJI engine. The engine fuel map was generated in a four-cylinder boosted configuration under highly dilute conditions, up to 40% external exhaust gas recirculation (EGR).

A vehicle simulation was then performed to further explore fuel economy gains using the fuel map generated for the DM-TJI engine. The DM-TJI engine was embodied in an industry-based vehicle

to examine the behavior of the engine over the U.S. Environmental Protection Agency (EPA) driving schedules. The results obtained from the drive cycle analysis of the DM-TJI engine in an industry-based vehicle were compared to the results of the same vehicle with its original engine. The vehicle equipped with the DM-TJI system was observed to benefit from ~13% improvement in fuel economy and ~11% reduction in CO_2 emission over the EPA combined city/high driving schedules. Potential improvements were discussed, as these results of the drive cycle analysis are the first-ever reported results for a DM-TJI engine embodied in an industry-based vehicle.

The resulting fuel economy and CO_2 emission were used to conduct a cost-benefit analysis of a DM-TJI engine. The cost-benefit analysis followed the economic and key inputs used by the U.S. EPA in a Proposed Determination prepared by that agency. The outcomes of the cost-benefit analysis for the vehicle equipped with the DM-TJI system were reported in comparison with the same vehicle with its base engine. The extra costs of a DM-TJI engine were observed to be compensated over the first three years of the vehicle's life time. The results projected maximum savings of approximately 2400 in 2019 dollars. This includes the lifetime-discounted present value of the net benefits of the DM-TJI technology, compared to the base engine examined. In this dollar saving estimate, the societal effects of CO_2 emission were calculated based on values by the interagency working group (IWG) at 3% discount rate.

To my Mother and my Father

"I am so close, I may look distant.
So completely mixed with you, I may look separate.
So out in the open, I appear hidden.
So silent, because I am constantly talking with you."

\- Rumi

ACKNOWLEDGEMENTS

First and foremost, I would like to acknowledge my PhD adviser Professor Harold Schock for his continuous support over the course of last five years. Dr. Schock accepted me as his PhD student, while my resume did not reflect much of engine-related research. He trusted my eagerness to learn and gave me an opportunity to grow. I will be, forever, thankful for this opportunity. I found myself and learned to trust my capabilities through his leadership. I learned from him through his comments at various times, not only in regard to me but also when it came to others. I completely understood that there is nothing as “my bad” and you are allowed to make “small mistakes,” as long as you learn from them. I learned that you should find the person to trust and after that, you should allow them to guide you in the right direction. I learned that the path may have its own ups and downs. However, you will be fine at the end if you have chosen the right person to trust. Dr. Schock, I am truly grateful for having you as my adviser and I will never forget the journey we had together.

I am very grateful to Dr. Matt Brusstar of the U.S. EPA who was not officially my adviser but did not put forward anything less than an adviser. I will never forget our first one-by-one meeting, as he walked me through the reality of life. He taught me to raise my level of acceptance if I wish to accomplish anything in life. He and his to-the-point comments shed light on so many of my mind questions. When it comes to him, I will never know which one is going to win, his depth of knowledge or his eagerness to teach. Thank you, Matt. You have been a true mentor to me.

I would like to thank Professor Thomas Voice for having served both as a member of my PhD committee and the primary adviser for my PhD specialization in “Environmental Policy.” Dr. Voice clearly saw my needs to define the right project which was worth the effort. I could never guess, such a blessing this experience will turn out to be. I truly enjoyed our conversations in the realm of policy which introduced me to a completely new scenery. Dr. Voice, thank you for believing in me.

I am grateful to my other committee members: Professor Guoming (George) Zhu for his clarifying suggestions on combustion zone modeling and engine simulations. Dr. Zhu, your suggestions have always rung a bell in my mind and for that and so many other things, I am truly thankful. Professor Farhad Jaberi for having taught me three graduate courses and for having served as a member of my PhD committee. I have always admired his depth of knowledge in model development and numerical simulations. Dr. Jaberi, thanks for teaching me all those exciting materials.

I am wholeheartedly grateful to Thomas Stuecken for his support, always being there, and technical knowledge. Tom could always propose a novel, exciting way for testing a phenomenon. Tom, you have been a true friend and I have learned a lot from you. I never understood how one person could be this much knowledgeable and, at the same time, 100-percent down-to-earth. I will never forget our times together, Mr. Bubble!

Furthermore, I want to acknowledge Kevin Moran, Brian Rowley, John Przybyl, and Brian Deimling for their help in setting up the experiments. I could not have finished the work if you had not been there to help. I would also like to Thank Jennifer Higel for her wonderful depiction of realities. Jen, thanks a lot for your prompt response and for always willingness to help. A special thanks goes to the current and former graduate students: Dr. Ravi Teja Vedula, Dr. Ali Kharazmi, Dr. Ruitao Song, Sabah Sadiyah Chowdhury, Cyrus Atis Arupratan, Yidnekachew Ayele, Yifan Men, Shen Qu, Christine Li, and Prasanna Chinnathambi. Thank you all for your support. It has been such a journey and I have learned from every one of you. Sabah, particularly thank you for all the emotional support and tolerating me crashing into your computer. I know it has been just a few months, but you are already one of my favorites.

My PhD project was supported by the U.S. EPA, Tenneco Inc., and the State of Michigan under Grant Number 83589201. I would like to thank Dr. Yong Sun and Adam Kotrba of Tenneco Inc. for their technical support. I am also grateful to so many people at the U.S. EPA National Vehicle and Fuel Emissions Laboratory (NVFEL) including: Mark Stuhldreher, Thomas Veling, Donald Dennis, Aaron Hula, Dr. Bob Giannelli, Dr. Andrew Moskalik, Ray Kondel, and Greg Davis. I could say something about every one of you, but it would take pages! I strongly believe that I could not have finished the project if I had not learned from each and every one of you. Thank you, all.

I have been extremely fortunate to learn from Jeff Alson (U.S. EPA), while working on my policy project. He has been the source to all I have learned in this regard. Jeff with his lifetime experience and knowledge was tremendously calm and patient, as he shaped my understanding of this new world. Thank you, Jeff.

I will be, forever, grateful for the help of Dr. Gloria Helfand (U.S. EPA). She has been a sudden blessing in the sky. I massively enjoyed her comments and suggestions, as she reviewed my final report of the policy project. Thank you, Gloria. You are amazing.

I want to also thank Paul Dekraker (U.S. EPA) for his help on the drive cycle analysis using the EPA ALPHA model. My drive cycle analysis would not have been completed if you had not been there to carefully explain every bit of details I needed to know. Thank you, Paul.

I am also thankful to my peers at UoM: Christina Reynolds, Justin Koczak, and Niket Prakash. I truly enjoyed our monthly meetings at NVFEL. I learned from you and grew with you. A special thanks also goes to Niket for walking me through the EPA ALPHA model. Thank you, guys!

Finally, I would like to thank my family – my extended family, my in-laws, my parents, my sister, Elaheh, my brother-in-law, Arjang, my wonderful nephew whom I miss dearly, Kian, and my husband, Hamid – for their love and support at different stages of my studies. Elaheh, my dearest sister, I promise I would not miss all the tea times any more. Thank you for holding my place and not giving it up easily. I specially want to thank my parents for believing in me to pursue my dreams. None of this would have happened if they had not gone through ups and downs of this journey with me. Thank you, you have been, always and forever, my strongest shoulder to hold on. Hamid, my best friend and partner in life, I have been the most fortunate to have you alongside me through this seemed-to-be endless journey at times. Thanks for always being there, no matter what!

TABLE OF CONTENTS

LIST OF TABLES

LIST OF FIGURES

CHAPTER 1

INTRODUCTION

1.1 Background and Motivation

Transportation consumes 70% of all U.S. petroleum use annually, contributing 1.8 gigatons of carbon dioxide (CO_2)-equivalent greenhouse gas (GHG) emissions [1]. Transportation is the United States' second biggest source of CO_2 emission, with 27% of U.S. totals [1,2]. Worldwide energy demands for transportation are predicted to rise substantially as the economy grows and the growing middle class aims to access more transportation [3]. The question then arises: what is the mobility for the future? Over the past decade or so, there has been a dramatic focus on electric vehicles (EVs) as a solution toward energy demands in the mobility system. However, are EVs going to take over internal combustion (IC) engines and if so, how fast will that happen? John Heywood briefly responds to this question in MIT News on April 18, 2018. He says [4]: "Electric vehicles are certainly going to play a useful role moving forward, but right now it is really difficult to estimate how big a role they will eventually play."

Transportation is a complex system consisting of all different modes of travel. It includes inland surface transport, sea transport, air transport, and transport through pipelines. Among all, the combination of light-duty vehicles, medium-duty/heavy-duty trucks, and commercial light trucks accounts for 78% of the total energy consumed in the transportation sector in year 2010. This consumption is projected to mildly decrease to 70% by the year 2050 [5]. Figure 0.1 represents the energy consumption by travel mode in quadrillion British thermal units for the years 2010 through 2050.

Additionally, the consumption of motor gasoline and distillate fuel oils (which includes diesel fuels and fuel oils) combined accounts for 82% of total energy consumed in the transportation sector in the year 2010, with a projection of 70% in the year 2050 as the use of alternative fuels increases [5]. Figure 0.2 displays the transportation sector consumption by fuel type in quadrillion British thermal units for the range of years reported by the Energy Information Administration (EIA) in their Annual Energy Outlook (AEO) 2018 [5].

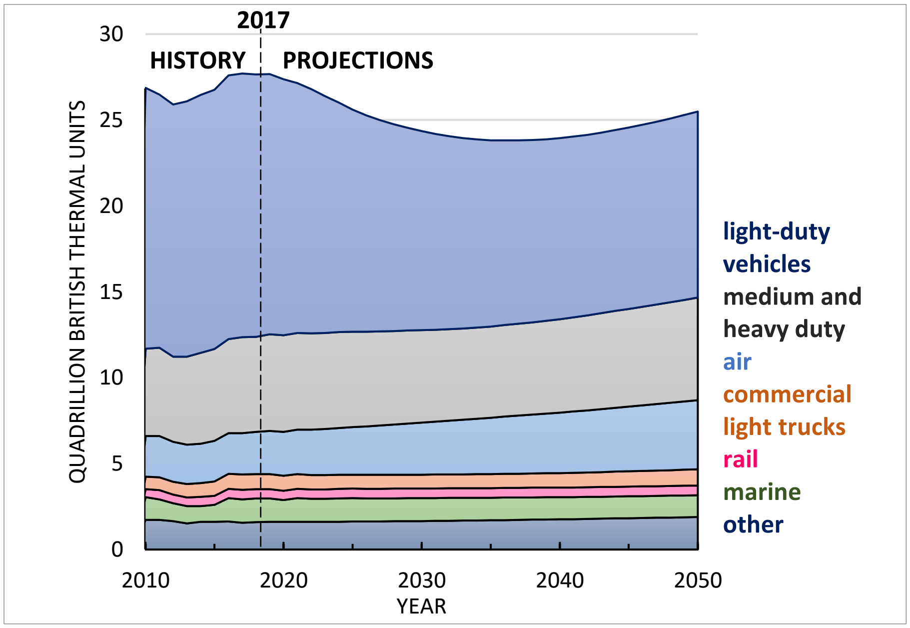

Figure 0.1 Energy consumption by travel mode, quadrillion British thermal units. The chart is directly taken from the EIA's AEO 2018 [5].

Figure 0.3 shows light-duty vehicle sales by fuel type, millions of vehicles, for the years 2010 to 2050 (projected value). As one can see, although the combined share of sales attributable to gasoline and flex-fuel vehicles declines (from 95% in 2017 to 78% in 2050), gasoline vehicles remain the dominant vehicle type through 2050 based on current predictions [5]. Flex-fuel vehicles use gasoline blended with up to 85% ethanol.

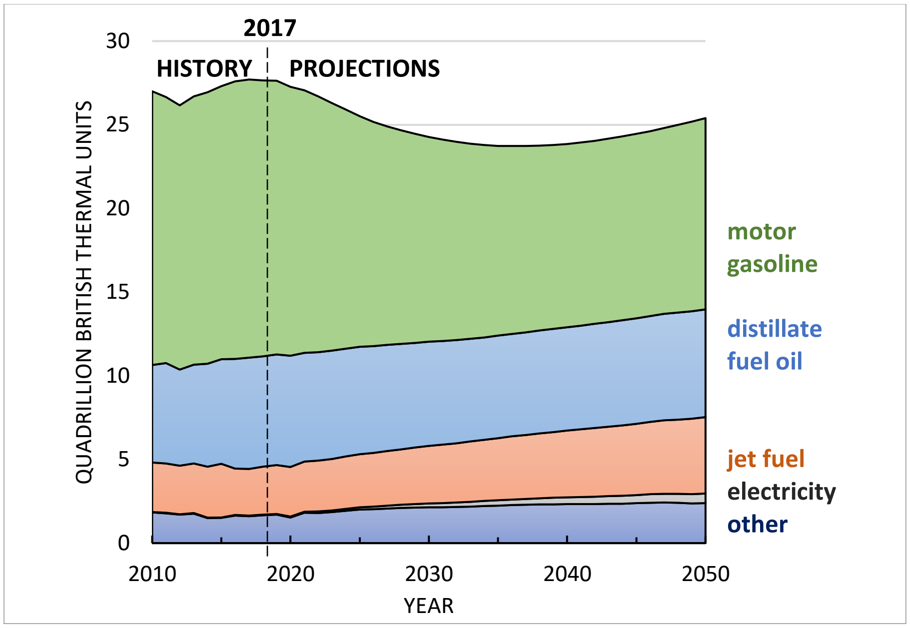

Figure 0.2 Transportation sector consumption by fuel type, quadrillion British thermal units. The chart is directly taken from the EIA's AEO 2018 [5].

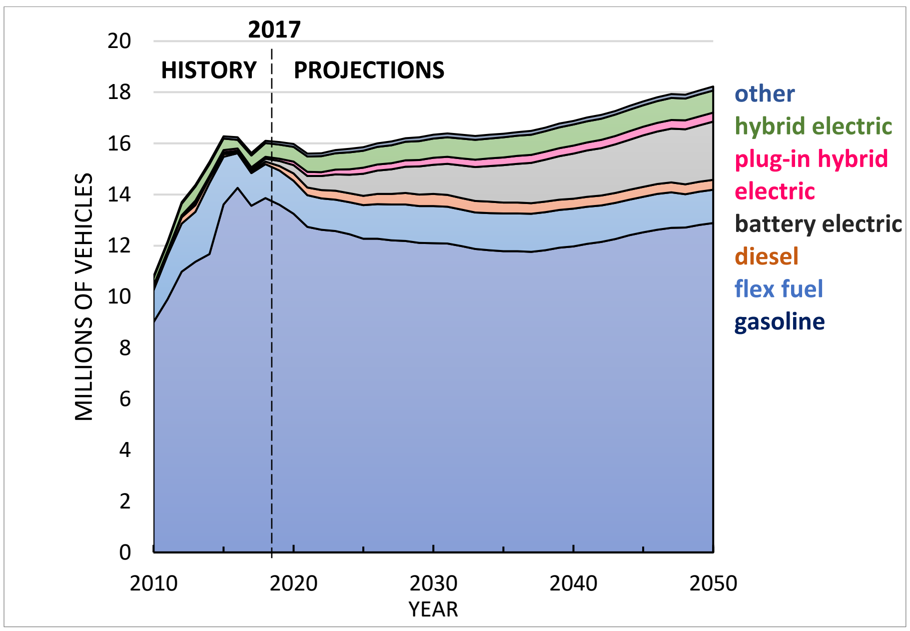

Figure 0.3 Light-duty vehicle sales by fuel type, millions of vehicles. The chart is directly taken from the EIA's AEO 2018 [5].

As statistics demonstrate, the number of vehicles powered by a source of energy other than traditional petroleum fuels, including electric vehicles, will increase as time passes. However, it seems that vehicles run on liquid fuels will be the major source of transportation for years to come. Thus, improving fuel economy of gasoline and diesel vehicles plays an important role toward reducing the environmental impacts on air quality and health, GHG emissions, and national oil dependency; all of which are caused as negative side effects of transportation powered by petroleum-derived fuels.

The Department of Energy (DOE) reports several approaches and technology improvement in their quadrennial technology review of 2015 for light duty (LD) and heavy-duty vehicles (HDVs) [1]. Tables 0.1 and 0.2 present the predicted gains in both GHG and petroleum reduction for different approaches studied.

Table 0.1 DOE prediction for GHG and petroleum benefits caused by advanced technologies in HDVs [1].

HDV	GHG Benefit	Petroleum Benefit	Timing
Combustion	25%	25%	Near
Systems	20%	20%	Near

Table 0.2 DOE prediction for GHG and petroleum benefits caused by advanced technologies in LDVs [1].

LDV	GHG Benefit	Petroleum Benefit	Timing
Combustion	25%	25%	Near
Systems	20%	20%	Near
Advanced Materials	20%	20%	Mid
Electrification	80%	80%	Mid
Fuel Cell	80%	80%	Long

As one can see, combustion improvement has been listed as one of the two near-term advances in technology toward reduction of both GHG and petroleum consumption. Advanced combustion strategies can be obtained through highly dilute and low-temperature combustion (LTC) modes in internal combustion (IC) engines. The Dual Mode, Turbulent Jet Ignition (DM-TJI) system is a distributed combustion technology to achieve LTC modes in spark ignition (SI) engines. The DM-TJI engine demonstrated the potential to provide diesel-like efficiencies and engine-out emission which can be controlled using a three-way catalytic converter.

Currently, there is not a model capable of estimating the fuel consumption and emission for a DM-TJI engine over standardized city/highway driving cycles. A driving cycle is a fixed schedule of a vehicle operation, defined in legislation, to test the real-world operation of the vehicle. In this dissertation, the path from engine experiments toward model development of a DM-TJI engine is described. The focus of this study is to project the fuel consumption and CO_2 emission for a vehicle equipped with the DM-TJI combustion technology over real-world driving cycles.

1.2 Structure of Dissertation

The dissertation is organized as follows. Chapter 2 describes a study done on a set of data collected from a 2013 Ford Escape 1.6-Liter EcoBoost® turbocharged gasoline direct injection (GDI) engine, tested at the U.S. Environmental Protection Agency (EPA). A zero-dimensional (0D) combustion model was developed and validated for the GDI engine operated at a wide range of loads and speeds. This study is believed to act as a foundation for future work to compare the combustion behavior of a production-based GDI engine with that of a DM-TJI engine.

Chapter 3 includes experiments and model development of a DM-TJI engine. Engine experiments were conducted on a single-cylinder DM-TJI engine at Michigan State University. A zero-dimensional/one-dimensional (0D/1D) engine simulation was performed using GT-SUITE/GT-POWER and the model developed was calibrated based on experimental data. The calibrated engine system model was further studied to propose a predictive, generalized model for a DM-TJI engine. An engine fuel map was, then, generated using the generalized model for the DM-TJI engine covering a wide range of loads and speeds.

In Chapter 4, the engine fuel map, generated by the predictive, generalized model in Chapter 3, was translated into vehicle fuel consumption and CO_2 emission over light-duty vehicle driving cycles. The drive cycle analysis was conducted using the U.S. EPA advanced light-duty powertrain and hybrid analysis (ALPHA) vehicle simulator tool.

Chapter 5 describes a cost-benefit analysis which was performed based on the results obtained from vehicle simulation using the EPA ALPHA model. This chapter is concluded with the comparison between the results of the cost-benefit analysis for a vehicle equipped with the DM-TJI system and those of the same vehicle with a production-based GDI engine.

The dissertation ends with concluding remarks and recommended steps for future work in Chapter 6.

1.3 Specific Aims

The specific aims for each of the chapters in this dissertation are summarized below.

Chapter 1:

- Briefly discuss the ongoing needs to improve brake efficiency of internal combustion (IC) engines.

Chapter 2:

- Develop a zero-dimensional (0D) combustion model for a gasoline direct injection (GDI) engine.
- Set the ground for future work where the combustion behavior of a production-based GDI engine would be compared to that of a Dual Mode, Turbulent Jet Ignition (DM-TJI) engine.

Chapter 3:

- Numerically predict the ancillary work requirement to operate the DM-TJI system.
- Map the path from engine experiments toward model development of a DM-TJI engine with a pre-chamber air valve assembly.

- Propose a predictive, generalized model for a DM-TJI engine, with minimal experimental input.
- Generate a complete fuel map for the DM-TJI engine in a boosted highly-dilute configuration

Chapter 4:

- Demonstrate a general understanding of the U.S. EPA ALPHA model.
- Predict fuel economy and CO_2 emission for a vehicle equipped with the DM-TJI combustion technology and compare the results obtained with those of the same vehicle with its original engine.

Chapter 5:

- Map the path to conduct a cost-benefit analysis following the methodology taught by the U.S. EPA in their "Proposed Determination on the Appropriateness of the Model Year 2022-2025 Light-Duty Vehicle Greenhouse Gas Emissions Standards under the Midterm Evaluation: Technical Support Document."
- Perform the cost-benefit analysis of a vehicle equipped with the DM-TJI combustion technology and compare the results obtained to those of the same vehicle with its original engine.

Chapter 6:

- Conclude and recommend the steps for future work.

CHAPTER 2

COMBUSTION MODEL FOR A HOMOGENEOUS TURBOCHARGED GASOLINE DIRECT INJECTION ENGINE

2.1 Introduction

In recent years, a range of different technologies has been under consideration to improve the fuel economy of gasoline engines and reduce exhaust emissions. Among these, gasoline direct injection (GDI) engines have shown significant market acceptance [6,7]. Therefore, a large portion of light-duty vehicle developments leans toward achieving higher thermal efficiency and lower exhaust emissions using GDI engines. Recent GDI engines include substantial technology developments [8] such as:

- Higher compression ratio
- Charge dilution using exhaust gas recirculation (EGR)
- Tumble enhancement
- Higher ignition energy
- Late intake valve closure timing (Miller cycle)

Direct injection of the fuel into the combustion chamber decreases the charge temperature, resulting in higher volumetric efficiency and less knock tendency at higher compression ratios. These characteristics lead to higher thermal efficiency and power output for GDI engines which facilitate engine downsizing. GDI engines can be designed to operate in both homogeneous and lean stratified modes of operation. Homogeneous charge is obtained through early intake injection of the fuel. Stratified charge, on the other hand, is attained as a result of a late fuel injection during compression stroke. This causes a local fuel-rich mixture in the vicinity of the spark plug, surrounded by a globally fuel-lean mixture in the combustion chamber. At engine low-to mid-load operation, the homogeneous mode with its higher combustion stability lacks the advantage of lower pumping work compared to the lean stratified mode. Combustion stability is challenging to obtain in lean stratified mode due to high cycle-to-cycle variability of in-cylinder charge motion and quenching of the flame. Today, however, the majority of engines operate in homogeneous mode of operation.

2.2 Objective

The importance of GDI engines in current and future markets is identified, and it is worthwhile to develop predictive combustion models that allow the engine developers to find optimal operating conditions. There have been several published numerical and experimental investigations on GDI engines. Fuel economy and exhaust emissions were numerically and/or experimentally studied under different injection strategies and advanced injection systems [9–12]. Berni et al. examined the effects of water/methanol injection as knock suppressor on a downsized GDI engine [13]. Simulations of in-cylinder charge motion, spray development, and wall impingement in GDI engines were performed by Lucchini et al. and Fatouraie et al. [14,15]. Cho et al. investigated the combustion and heat transfer behavior in a single-cylinder GDI engine [16]. The aforementioned studies cover a wide variety of subjects. However, the current author did not find any in-depth investigation on the zero-dimensional combustion model of a GDI engine.

Burnt et al. and Egnell conducted a single-zone heat release analysis on direct-injection diesel engines [17,18]. Dowell and colleagues meticulously evaluated the heat release modeling of modern high-speed diesel engines [19]. Lindström et al. reported an empirical combustion model for a port fuel injection (PFI) spark ignition engine [20]. Hellström et al. and Prakash et al. [21,22] have done studies on the combustion model of spark-assisted compression ignition (SACI) engines. Spicher et al. showed GDI development potentialities and compared the heat release behavior of PFI and GDI engines [23]. Huegel et al. investigated the heat transfer of a single-cylinder GDI engine with a side study on the heat release behavior of the engine in both homogeneous and stratified modes of operation [24]. Results obtained in the current study well agree with the works done by Spicher and Huegel describing heat release behavior and consequently the combustion model of a GDI engine.

The primary goal of this chapter is to develop a zero-dimensional (0D) combustion model which can be used towards the whole-cycle simulation of a GDI engine. However, the study covers a preliminary heat release analysis of a Dual Mode, Turbulent Jet Ignition (DM-TJI) engine and compares the results obtained with those of the GDI engine. The results for the heat release analysis of the DM-TJI engine in comparison with the GDI engine are presented in a short section at the end of this chapter, Section 2.6.

This chapter is organized as follows. The experimental arrangement is first described. After that the numerical approach and model development are explained, followed by the section providing the numerical results using experimental data and the discussion of the results. A short section, at the end of this chapter, covers the preliminary results for the heat release behavior of a DM-TJI engine and compares the combustion characteristics of current homogeneous turbocharged GDI engine with those of the DM-TJI engine. Conclusions are drawn in the last section.

2.3 Experimental Arrangement

2.3.1 Experimental Setup

Experimental data was collected from a 2013 Ford Escape 1.6-Liter EcoBoost® turbocharged GDI engine. To make use of the stock engine and vehicle controllers, the engine was tethered to its vehicle located outside the test cell. Details of the test site, vehicle tether information, engine setup, engine systems including intake/exhaust, charge air cooling, cooling system, oil system, and front end accessory drive (FEAD) can be found in the work done by Stuhldreher and colleagues [25]. Engine specifications are listed in Table 2.1.

Table 2.1 Engine specifications.

Vehicle (MY, Make, Model)	2013 Ford Escape
Engine (Displacement, Name)	1.6 L EcoBoost®
Rated Torque	240 N-m @ 1600-5000 RPM
Rated Power	180 hp @ 5700 RPM
Compression Ratio	10:1
No. of Cylinders	4
Firing Order	1-3-4-2
Fuel Injection	Common rail
Fuel Type	LEV III regular gasoline

2.3.2 Data Set Definition

The data logged included engine torque, fuel flow rate, air flow rate, pressures, temperatures, in-cylinder pressure, and OBD/extended proportional-integral-derivative (PID) controller area network (CAN) data.

2.3.3 Data Collection Procedure

Two data acquisition systems were used. The first was an A&D Technology iTest Test System Automation Platform for low-frequency data at a rate of 10 Hz. The second was an A&D Technology Combustion Analysis System (CAS) for high-frequency data acquisition. CAS was sampled at 0.1 crank angle resolution and calculated results were transmitted to iTest at 10 Hz rate.

The engine with its associated engine control unit (ECU) operates under original equipment manufacturer (OEM) specific protection modes. These protection modes limit the engine operation in a test cell, especially at higher loads as engine temperatures reach the safety thresholds. To obtain experimental data, two test procedures were used to compensate for the protection modes.

The first procedure was used for the loads below ~70% of the maximum rated torques at which the engine temperatures remain within the safety thresholds. During this procedure, a set of selected parameters was used as stability criteria. These parameters included fuel flow, torque, and turbine inlet temperature. The settling time ranged from 20 seconds to 30 seconds at different loads and speeds.

The second procedure was used to obtain high-load data which go beyond OEM safety thresholds. It should be noted that in real-world driving the engine does not remain at high-load operating conditions for more than a few seconds. Thus, the quasi-steady-state values were of interest for the high-load operating points beyond the OEM safety thresholds. This second procedure started with the engine being set to the desired speed and a load of 10 N-m. The data logger was triggered on and the load stepped to the desired value. The data was logged for 20 seconds in total before the engine was brought back to the cool-down mode of 1500 rpm and 10 N-m.

Table 2.2 Loads, speeds and corresponding case numbers.

		Load (N-m)		
		60	**120**	**180**
Speed (RPM)	**1500**	1	2	3
	2000	4	5	6
	2500	7	8	9
	3000	10	11	12
	3500	13	14	15
	4000	16	17	–
	4500	18	19	–

Details of these test procedures can be found in the study by Stuhldreher et al. [25]. A total of 50 cycles was used for the current study at each operating condition. Table 2.2 shows all the cases studied here. It should be noted that the engine was always operated at stoichiometric condition.

2.4 Numerical Approach and Model Development

The current study performed a zero-dimensional/one-dimensional (0D/1D) simulation with a single-zone thermodynamic analysis of the cylinder. Engine modeling can be broadly separated into two different categories, 0D/1D engine simulation tools and high-fidelity three-dimensional (3D) modeling platforms. The 0D/1D simulation tools are used for engine studies and optimizations, when computationally expensive 3D simulations are impractical. More information on different approaches in engine modeling can be found in Section 3.5, under “Modeling Platform” (3.5.1).

2.4.1 Heat Release Analysis

The single-zone analysis applied in the current work considered the change in sensible internal energy (first term on the right-hand side of Equation 2.1), work done by the piston motion (second term); and heat transfer from in-cylinder gas to the walls ($Q_{h.t}$). The effects of blow-by and crevices were assumed to be negligible. The energy equation is written as [26,27]:

$$\frac{dQ_{ch}}{dt} = \frac{1}{\gamma - 1} V \frac{dp}{dt} + \frac{\gamma}{\gamma - 1} p \frac{dV}{dt} + \frac{dQ_{h.t}}{dt} \tag{2.1}$$

where, Q_{ch} is the apparent total heat release in kJ; γ is the specific heat ratio; V is the in-cylinder volume in m^3; p is the in-cylinder pressure in kPa; and $Q_{h.t}$ is the heat transfer to the walls in kJ.

2.4.1.1 Net Heat Release

The summation of change in sensible internal energy and work done by the piston is commonly called net heat release. When the in-cylinder pressure and volume are known, net heat release can be calculated if the dependency of specific heat ratio, or gamma, on temperature is well defined. In general, gamma is a function of both temperature and mixture composition. However, as Chang et al. showed [28], ignoring the gamma dependency on mixture composition leads to a negligible error. They reported a third-order polynomial gamma dependency on temperature as a result of curve-fitting at a median air/fuel ratio. This polynomial (Equation 2.2) was used in the current work.

$$\gamma = -9.97 \times 10^{-12} T^3 + 6.21 \times 10^{-8} T^2 - 1.44 \times 10^{-4} T + 1.40 \tag{2.2}$$

where, γ and T are specific heat ratio and temperature, respectively.

Average in-cylinder temperature was determined from the ideal gas law using the total mass trapped in the cylinder at the intake/exhaust valve closing (IVC/EVC), the in-cylinder pressure at each crank angle, and the corresponding in-cylinder volume. This temperature was believed to be close to the mass-averaged cylinder temperature during combustion, since the molecular weights of burned and unburned mixtures are basically the same [26]. Trapped in-cylinder mass can be calculated as a summation of trapped air, fuel, internal exhaust gas recirculation (EGR), and external EGR in the combustion chamber. There was no external EGR for any of the cases under study. Thus, the term was set to zero.

The internal EGR was calculated using the Yun and Mirsky correlation [29]. An iterative algorithm was used to find gamma and in-cylinder temperature at IVC. The in-cylinder temperature at IVC can be calculated as a weighted average of intake temperature and exhaust temperature at intake pressure as follows [20].

$$T_{exh}^{*} = T_{exh}\left(\frac{p_{int}}{p_{exh}}\right)^{(\gamma-1)/\gamma} \tag{2.3}$$

$$x_r = \frac{V_{EVC}}{V_{EVO}}\left(\frac{P_{EVC}}{P_{EVO}}\right)^{1/\gamma} \tag{2.4}$$

$$T = (1 - x_r)T_{int} + x_r T_{exh}^{*} \tag{2.5}$$

where, T_{exh}^{*} is the exhaust temperature at intake pressure; T_{exh} is the exhaust temperature; p_{exh} is the exhaust pressure; V is the in-cylinder volume; and x_r is the internal residual gas fraction. In addition, subscripts int, EVC, and EVO denote intake, exhaust valve closing, and exhaust valve opening; respectively.

2.4.1.2 Heat Transfer Model

The GT-POWER WoschniGT heat transfer model was used to simulate the heat transfer term in the energy equation of the heat release analysis. WoschniGT closely matches the classical Woschni correlation without swirl. The most important difference lies in the treatment of heat transfer coefficients when the intake and exhaust valves are open, and intake inflow velocities and exhaust backflow velocities increase the in-cylinder heat transfer. The heat transfer coefficient in the WoschniGT correlation is calculated as follows.

$$h_{c\,Woschni} = \frac{K_1 p^{0.8} w^{0.8}}{B^{0.2} T^{K2}} \tag{2.6}$$

where, $h_{c\,Woschni}$ is the convective heat transfer coefficient in $\mathrm{W}/\mathrm{m^2K}$; p is the in-cylinder pressure in kPa; w is the average cylinder gas velocity in $\mathrm{m/s}$; B is the cylinder bore in m; and T is the in-cylinder temperature in K. Additionally, k_1 and k_2 are given constants as 3.01 and 0.50, respectively. The average cylinder gas velocity is calculated in Equation. 2.7.

$$w = C_1 \overline{S}_p + \frac{C_2 (V_d T_r)}{P_r V_r}(p - p_m) \tag{2.7}$$

where, $\bar{S}_p$ is the mean piston speed in m/s; V_d is the displacement volume in m^3; T_r is the working fluid temperature prior to combustion in K; P_r is the working fluid pressure prior to combustion in kPa; V_r is the working fluid volume prior to combustion in m^3; p is the in-cylinder pressure in kPa; and p_m is the motoring in-cylinder pressure at the same angle as p in kPa.

The c_1 and c_2 are constants calculated as below, Equations 2.8 and 2.9.

$$C_1 = 2.28 + 3.90 \min\left(\frac{\text{Net mass flow into cylinder from valves}}{\text{Trapped Mass} * \text{Engine Frequency}}, 1\right) \tag{2.8}$$

$$C_2 = \begin{cases} 0 & \text{During cylinder gas exchange and compression} \\ 3.24\text{E} - 3 & \text{During combustion and expansion} \end{cases} \tag{2.9}$$

After calculation of the heat transfer coefficient using WoschniGT formulation (Equations 2.6, 2.7, 2.8, 2.9), the rate of in-cylinder heat transfer can be calculated as below, Equation 2.10. Since there was no temperature data available for the piston, head, and liner of this Ford EcoBoost® engine, the temperature profiles were extracted from the work by Huegel et al. on a single-cylinder GDI engine [24]. A heat transfer multiplier (HTM) was used to adjust the heat transfer term, assuming the combustion efficiency as 99.9% with no blow-by or crevice losses.

$$\frac{dQ_{h.t}}{dt} = HTM\ h_c \begin{pmatrix} A_{piston}(T - T_{wall,\ piston}) + \\ A_{head}(T - T_{wall,\ head}) + \\ A_{liner}(T - T_{wall,\ liner}) \end{pmatrix} \tag{2.10}$$

where, $Q_{h.t}$, HTM, h_c, A, and T represent the in-cylinder rate of heat transfer, the heat transfer multiplier, the heat transfer coefficient, the surface area, and the in-cylinder temperature; respectively.

2.4.1.3 Start of Combustion

Several approaches can be found in the literature to define start of combustion (SOC). Reddy et al. studied determination of SOC based on first and second derivative of in-cylinder pressure [30]. Hariyanto et al. applied the wavelet analysis to define SOC of a diesel engine [31]. Shen et al. and Bitar et al. defined SOC as the start for the dynamic stage of combustion, which corresponds to the transition between compression and expansion processes; using a pressure-volume (P-V) diagram [32,33]. Katrašnik et al. developed a new criterion to determine SOC [34]. Their study mathematically demonstrated the delay in SOC prediction using the first and second derivatives of in-cylinder pressure. They proposed a SOC criterion based on the local maximum of third derivative of in-cylinder pressure with respect to crank angle. Determination of SOC using wavelet analysis requires the engine vibration data which was not available. Additionally, Hariyanto et al. showed a high degree of correlation between the results from their wavelet analysis and the SOC criterion of the Katrašnik group. The accuracy of SOC determination methods based on the P-V diagram depends on a level of judgment in defining SOC as the point in which the straight portion of compression stroke deviates from its averaged path.

The current work used the SOC criterion by Katrašnik group. Signal preparation for in-cylinder pressures was done using a MATLAB filtering algorithm called “filtfilt.” This algorithm performs a zero-phase forward and reverse filtration. Design specifications were set to a third-order Butterworth filter with a 0.1 normalized cutoff frequency for the 3 dB point, corresponding to 450 Hz – 1350 Hz for different speeds. The ignition delay was defined as the difference between spark timing and calculated SOC for the range of speeds and loads studied.

2.4.2 Combustion Model

Ivan Wiebe was one of the pioneers to connect the rate of combustion to chain chemical reactions in an internal combustion engine [21,35]. In real combustion systems, chain reactions progress sequentially and in parallel with reactions involved in the formation of intermediate species called "active centres" [35]. Active centres, which were referred to as effective centres by Wiebe, initiate effective reactions which result in the formation of combustion products. The well-known Wiebe function was developed on the basis of this concept [35].

The current work demonstrates a two-stage heat release phenomenon for the studied GDI engine. Thus, a single Wiebe function is not suitable to capture the heat release characteristics of the engine wherein pre-mixed combustion is followed by a diffusion-like combustion. "Diffusion-like" combustion here is characterized with the slow-rate combustion as a result of either mixture inhomogeneity or wall impingement. The mixture inhomogeneity can arise due to locally fuel-rich regions, thereby leading to a slow-rate combustion. The wall impingement, on the other hand, can result from fuel film deposition or flame hitting the wall. The deposited fuel film can evaporate in the course of combustion, resulting in the second stage of heat release. Also, the heat losses when the flame reaches the chamber walls would slow down the rate of combustion.

The current study used a double-Wiebe function to fit the results of heat release calculation; see Equation 2.11.

$$
\begin{aligned}
x_b(\theta) = \; & alpha\left\{1 - exp\left[-a\left(\frac{\theta - \theta_0}{\Delta\theta_1}\right)^{m_1+1}\right]\right\} \; + \\
& (1 - alpha)\left\{1 - exp\left[-a\left(\frac{\theta - \theta_0}{\Delta\theta_2}\right)^{m_2+1}\right]\right\}
\end{aligned} \tag{2.11}
$$

where, $a = -\ln 0.001 = 6.9$, and α is the switch point from the 1st Wiebe function to the 2nd; θ is the instantaneous crank angle degree; θ_0 is the start of combustion; $\Delta\theta_1$ and $\Delta\theta_2$ are the total burn durations for the 1st and 2nd Wiebe functions; and m_1 and m_2 are the combustion mode parameters or Wiebe exponents for the 1st and 2nd Wiebe functions.

2.4.2.1 Semi-Predictive Combustion Model

The double-Wiebe function includes six unknown variables, α, m_1, m_2, $\Delta\theta_1$, and $\Delta\theta_2$, and the SOC (θ_0). The first five variables were determined based on a non-linear least-squares optimization using MATLAB Curve Fitting Toolbox™. The SOC was determined using the Katrašnik et al. criterion as mentioned earlier. A total of six look-up tables, one for each variable, was built for different loads and speeds. These look-up tables were used in the GT-POWER model as discussed next.

2.4.2.2 GT-POWER Model

The effectiveness of the semi-predictive combustion model was tested by comparing the experimental in-cylinder pressures with results obtained from a model built using the 0D/1D engine simulation tool, GT-SUITE/GT-POWER (Gamma Technologies). The six variables of the double-Wiebe function, used to model the two-stage combustion behavior of the GDI engine, were defined in GT-POWER by importing the look-up tables built from the semi-predictive combustion model. The GT-POWER model simulates the engine components from intercooler outlet to turbine inlet. Component characteristics were set based on experimentally measured data and 3D computer-aided design (CAD) models including: valve geometries, timings, lift profiles, and discharge coefficients; in-cylinder and port geometries; injection timings and durations, and air/fuel ratio. The engine induction and exhaust system were built to a close approximation, as there was no CAD model available. The intake manifold throttle angle was controlled using a proportional-integral (PI) controller with brake mean effective pressure (BMEP) as its input value. The in-cylinder heat transfer model was set to WoschniGT with the same in-cylinder temperatures and heat transfer multiplier of heat release analysis described earlier. The combustion model was imposed based on results obtained from the semi-predictive combustion model.

2.4.2.3 Predictive Combustion Model

The semi-predictive combustion model, verified using the GT-POWER simulation, was further studied to find correlations for each of the six variables of the double-Wiebe function. The corresponding combustion model, called "predictive combustion model," can correlate the combustion behavior of the GDI engine to a set of engine parameters. The predictor parameters (x_1 to x_4) chosen for each of these variables are listed in Table 2.3. The linear correlations, as shown in Expression 2.12, were found to well predict the six variables. The first four variables: θ_0, α, $\Delta\theta_1$, and $\Delta\theta_2$; were predicted using the manifold temperature (T_{man}), internal EGR ($iEGR$), engine speed, and ignition timing (θ_{ign}). However, the behavior of last two variables, m_1 and m_2, were best captured by using $\Delta\theta_1$ and $\Delta\theta_2$, respectively, along with $iEGR$ and $Speed$ as model predictor parameters (see Table 2.3). Thus, the same linear correlation shown in Expression 2.12 was used for m_1 and m_2, excluding the x_4 parameter. A variety of parameters were examined to define these dependencies. It seems that the engine in-cylinder characteristics at different loads and speeds could be well captured by current predictor parameters. The combination of manifold temperature and fraction of internal EGR was believed to act as an indicator of the boundary temperature. The speed parameter could play a role in capturing the in-cylinder turbulence. The ignition timing, along with three other parameters, could represent the effect of flame initiation on the combustion behavior.

$$a_0 + a_1x_1 + a_2x_2 + a_3x_3 + a_4x_4 \quad (2.12)$$

where, a_0 to a_4 are constants calculated from the results obtained for the semi-predictive combustion model using linear regressions.

Table 2.3 Double-Wiebe variables and associated predictor parameters.

Variables	x_1	x_2	x_3	x_4
$\boldsymbol{\theta_0}$	T_{Man}	$iEGR$	$Speed$	θ_{ign}
$\boldsymbol{\alpha}$	T_{Man}	$iEGR$	$Speed$	θ_{ign}
$\Delta\boldsymbol{\theta_1}$	T_{Man}	$iEGR$	$Speed$	θ_{ign}
$\Delta\boldsymbol{\theta_2}$	T_{Man}	$iEGR$	$Speed$	θ_{ign}
$\boldsymbol{m_1}$	$\Delta\theta_1$	$iEGR$	$Speed$	$-$
$\boldsymbol{m_2}$	$\Delta\theta_2$	$iEGR$	$Speed$	$-$

A least-squares optimization was performed using the MATLAB algorithm "LinearModel.fit" to minimize the root-mean-square (RMS) error in the prediction of each variable. The linear correlations found here were validated by regenerating the experimental cumulative heat release as discussed later.

2.5 Results and Discussion

The following discussion for the GDI engine is divided into three parts. The first part covers the results obtained for the heat release analysis including the ignition delays at different loads and speeds. The second part discusses the results for the semi-predictive combustion model. These results are followed by a comparison between the experimental and model regeneration of engine heat release in the third part.

2.5.1 Heat Release Analysis

The results obtained from the heat release analysis demonstrated rapid initial pre-mixed combustion (stage 1) followed by a gradual diffusion-like state of combustion (stage 2) for all the loads and speeds studied in this homogeneous charge GDI engine. Figure 2.1 shows the heat release rate for the loads of 60, 120, and 180 N-m at 2000 rpm. Pre-mixed and diffusion-like phases of combustion are clearly noticeable in this figure. To highlight the two stages of combustion in the figure, the rates of combustion at 120 and 180 N-m were shifted to the left with an offset of 6 and 19 crank angle degrees, respectively, to match their SOCs with that of the 60 N-m load. The end point for the pre-mixed combustion is the start point of the diffusion-like phase of combustion which continues up to nearly exhaust valve opening (EVO). The switch point from pre-mixed to diffusion-like phases of combustion was determined as the point where the double-Wiebe function shifts from the first Wiebe function to the second Wiebe function, the crank angle degree (CAD) corresponding to the α value. In this work, 0 CAD corresponds to firing top dead center (TDC). Cumulative heat release results obtained for 120 N-m at 2000 rpm are displayed in Fig. 2.2. In this figure, the peak of the resulting apparent heat release curve was matched to the total chemically released energy (energy from burned fuel), using averaged heat transfer calibrations. These calibrations were attained by adjusting the values for HTM. The blow-by and crevice losses were assumed negligible, and a value of 99.9% was used for the combustion efficiency of all the cases studied.

The SOCs were determined from filtered cycle-averaged cylinder pressure measurements, based on the local maximum of third derivative with respect to crank angle. Accordingly, the corresponding ignition delays are shown in Fig. 2.3. The reported ignition delays were not used in the current engine model development. Nevertheless, they are reported as they can be of interest to readers.

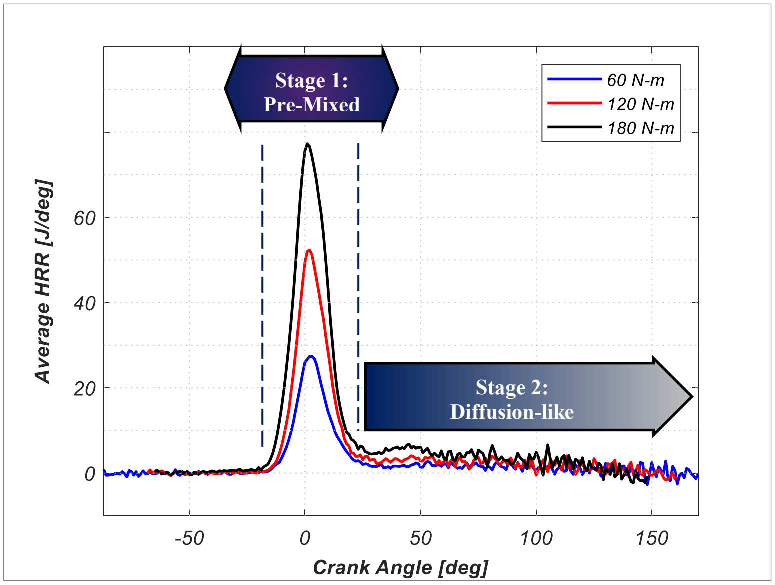

Figure 2.1 In-cylinder rate of heat release for three loads of 60, 120, and 180 N-m at 2000 rpm. The plots for 120 and 180 N-m were shifted to the left.

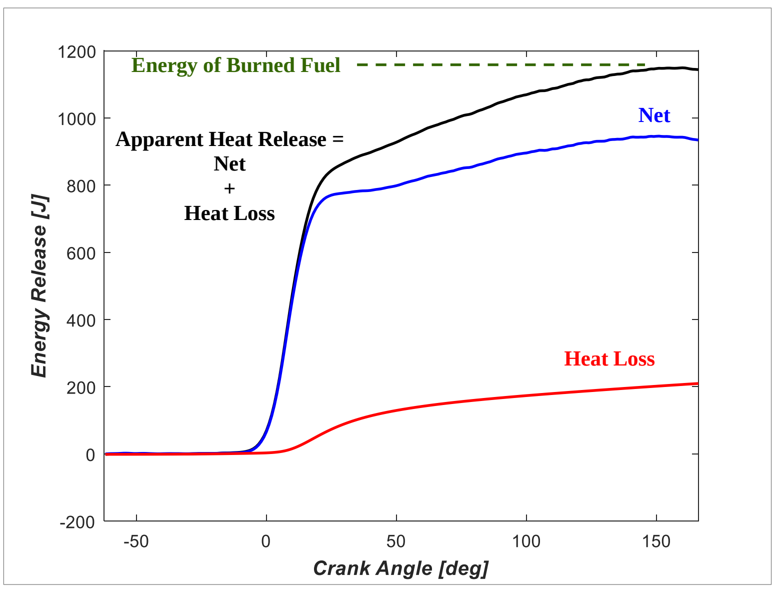

Figure 2.2 Cumulative heat release results at 2000 rpm/120 N-m.

The ignition delay, in general, increased with an increase in engine speed. However, the ignition delay first decreased with the increase in engine load and then slightly increased with further load increase from 120 N-m to 180 N-m. Assanis et al. reported the same trends for the ignition delay of a direct-injection diesel engine [36]. However, their results were limited to 100 N-m of load for a speed range of 900 rpm to 2100 rpm. It should be noted that the signal preparation for all the in-cylinder pressures was performed using a third-order Butterworth filter with a 0.1 normalized cutoff frequency for the 3 dB point, corresponding to 450 Hz – 1350 Hz for different speeds. This may result in some seemingly inaccurate ignition delays for the operating conditions at lower speeds. However, the matter caused by filter design specifications is inevitable without enough information regarding the nature of signal noise at each operating condition.

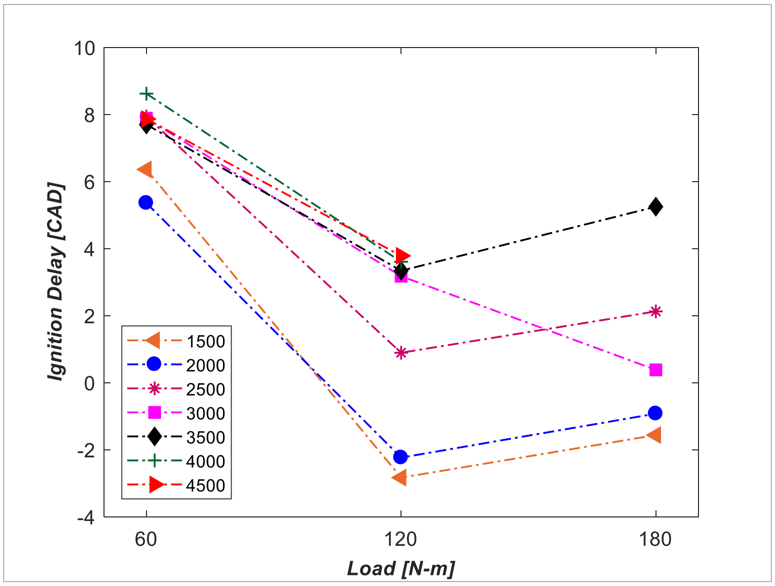

Figure 2.3 Engine ignition delay – all cases studied.

2.5.2 Semi-Predictive Combustion Model

The validity of the semi-predictive combustion model was tested using GT-POWER simulation. Figure 2.4 shows the comparison between experiments and numerical predictions for three loads of 60, 120, and 180 N-m at 2000 rpm. It should be noted that the plots in Figs. 2.4, 2.5, 2.9, and 2.10 begin at the SOC. The RMS errors between the measured and predicted in-cylinder pressures ranged from 0.4-1.2 bar which corresponds to 1.2-2.2% of the peak cylinder pressures.

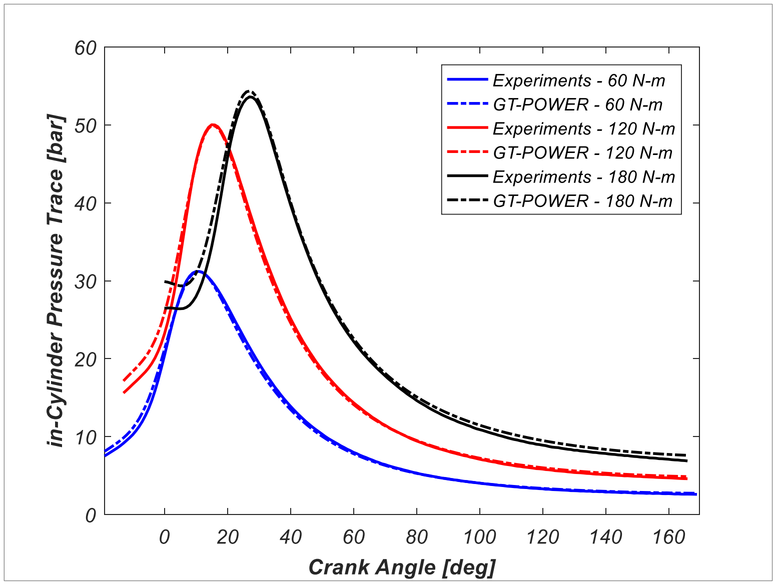

Figure 2.4 Cylinder pressures, experiments vs. numerical predictions at 2000 rpm.

It was observed that the model predicts higher air mass flow rate through the system, compared to experimental measurements. The model over-predictions of air mass flow rate ranged from 3-6%, resulting in 0.6-3.4 bar higher compression pressures. In addition, there were slight differences in pressure traces at EVO. The model predicts lower pressures, within 0.5 bar, for the exhaust stroke, leading to a lower pumping mean effective pressure (PMEP), within 0.2 bar, compared to that during experiments. It should be recalled that the wall temperatures for the heat transfer model were extracted from the work by Huegel et al [24]. For their single-cylinder GDI engine, the heat transfer models were reported to under-predict during the discharge (intake/exhaust) strokes and early compression. These under-predictions could be the reason behind the discrepancies seen in Fig. 2.4. During the early and late stage of combustion, the heat transfer term is the dominant term in the heat release calculation. Any under-predictions of this term would result in lower predicted in-cylinder temperatures and pressures. This causes the engine to take in more air, leading to higher modeling intake air flow rates and thus higher pressures. Additionally, the Ford 1.6-Liter

EcoBoost® is designed to be a high tumble engine. It may not be suitable to use the Woschni heat transfer model for tumble motion engines. Further studies are required to verify this inference.

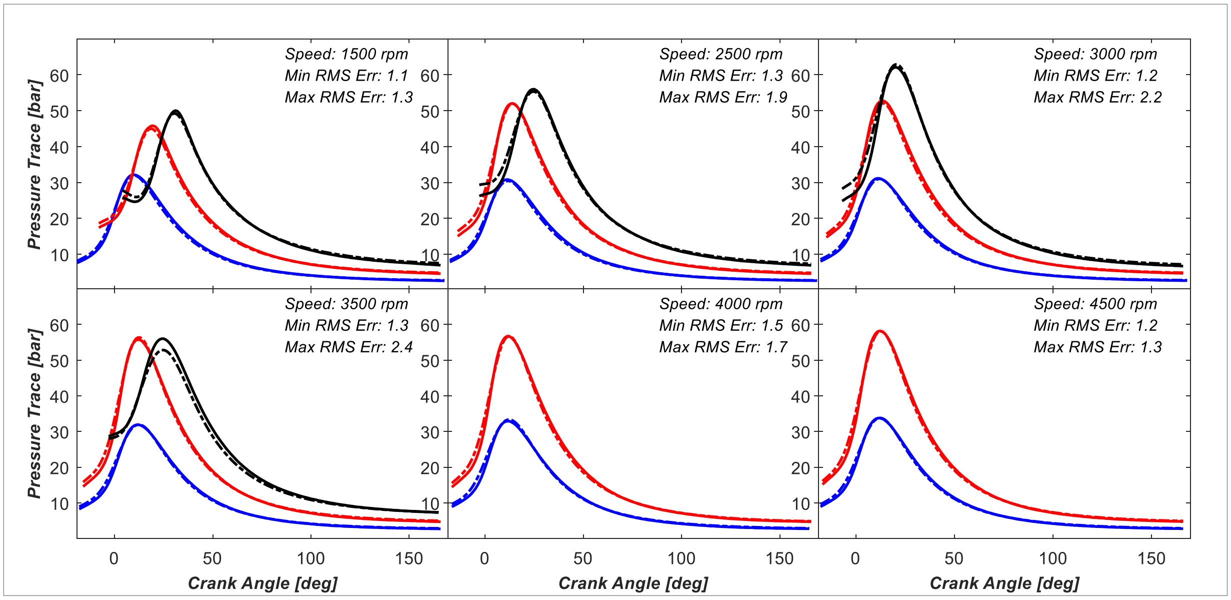

Figure 2.5 Cylinder pressures, experiments versus numerical predictions – all cases studied; solid and dash-dot lines represent the experiments and numerical prediction, respectively. In subplots for speeds from 1500 rpm to 3000 rpm, traces with low, medium, and high peak pressures represent loads of 60 N.m, 120 N.m, and 180 N.m; respectively. Traces for 3500 rpm do not follow the general trend as others and the pressure traces for 180 N.m have peak pressures slightly lower than 120 N.m. Subplots for 4000 rpm and 4500 rpm represent loads of 60 N.m and 120 N.m with the low and high peak pressures, respectively.

Experiments and numerical predictions for all other cases under study are shown in Fig. 2.5. The results achieved a reasonable degree of accuracy with an RMS error ranging from 1.1-2.4% of the peak cylinder pressures. The model was able to capture the peak pressure at all the loads and speeds except for 3500 rpm and 180 N-m (case #15). At this operating condition, the experimental data reveals a relatively low coolant temperature (marked with arrow in Fig. 2.6) which can be the response to the abnormally high in-cylinder temperature (see case #15 in Fig. 2.7). The load and speed associated with each of these case numbers, listed in Figs. 2.6, 2.7, and 2.8; can be found in Table 2.2. This abnormality was accounted for the larger deviation of experimental and numerical peak pressures. Additionally, higher pressures were observed for all the cases during the early compression and late expansion. The reason behind these discrepancies is identified while discussing Fig. 2.4.

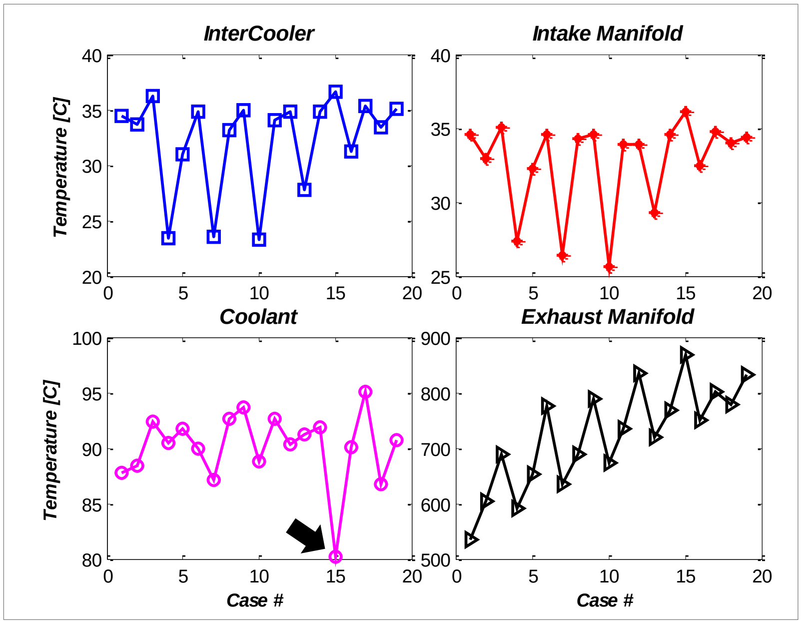

Figure 2.6 Intercooler, intake manifold, coolant, and exhaust manifold temperature – all cases studied. The load and speed associated to each of these case numbers can be found in Table 2.2.

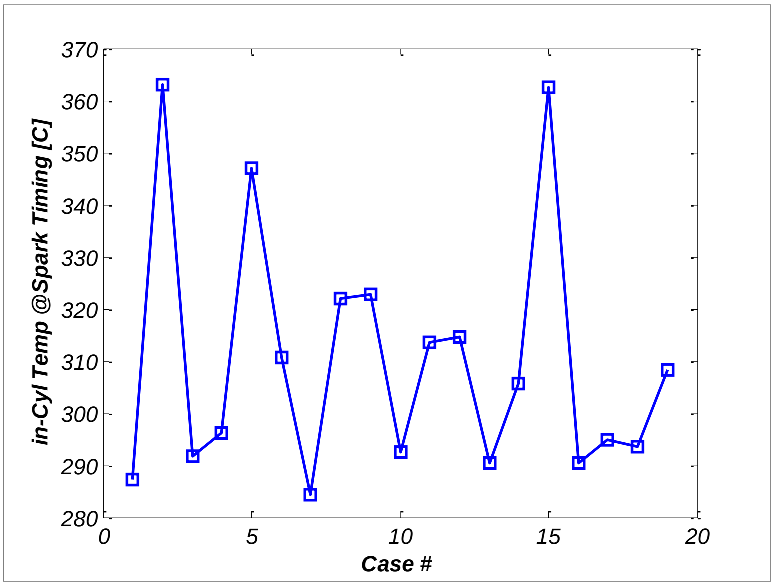

Figure 2.7 In-cylinder temperature at spark timing for all the cases. The load and speed associated to each of these case numbers can be found in Table 2.2.

2.5.3 Predictive Combustion Model

Predicting correlations were found for the six variables of the double-Wiebe function from the results obtained for the semi-predictive combustion model using linear regressions. The comparisons between direct calculations of double-Wiebe function variables and those of linearly developed model predictions are shown in Fig. 2.8. Results demonstrate a good prediction for all the variables except for $\Delta\theta_1$. However, even the linear model for $\Delta\theta_1$ with a low R-squared value of 0.51 predicts a general trend close to the experiments. It is shown in this figure that the major discrepancy happens at case #15 (speed/load of 3500 rpm/180 N-m). The abnormal behavior of this operating condition has been already discussed.

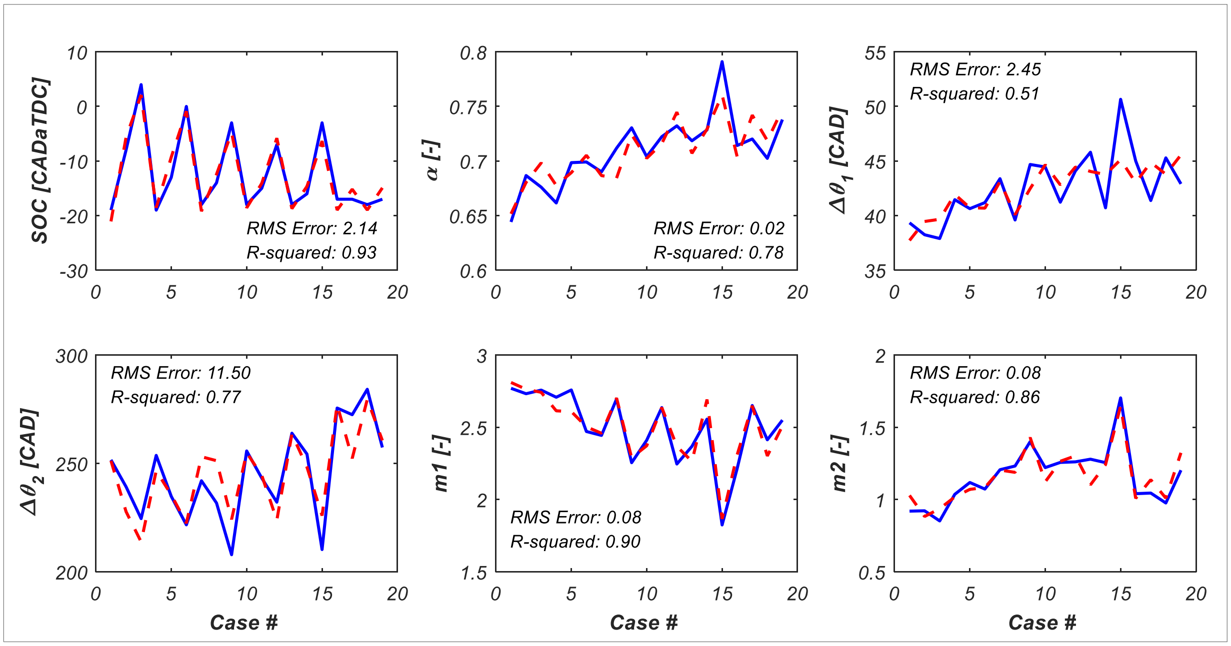

Figure 2.8 Double-Wiebe variables, direct calculations vs. linear model predictions; solid and dashed lines represent the direct calculations and model predictions, respectively. The load and speed associated with each of these case numbers can be found in Table 2.2.

Cumulative heat release can be regenerated using linear correlations found for the six variables of the double-Wiebe function. Figure 2.9 compares the cumulative normalized apparent heat release obtained from direct calculations with those from the developed linear model predictions for the loads of 60, 120, and 180 N-m at 2000 rpm. The RMS errors between direct calculations and model predictions ranged from 0.5-3.5%. The results obtained for all other loads and speeds can be found in Fig. 2.10. Overall, the comparison of direct calculations and model predictions showed an RMS error within 3.5%. Therefore, the developed predictive combustion model is believed to give a good prediction of in-cylinder heat release characteristics. The model accuracy can be improved further by employing non-linear regression models which were avoided in this work for the sake of model simplicity.

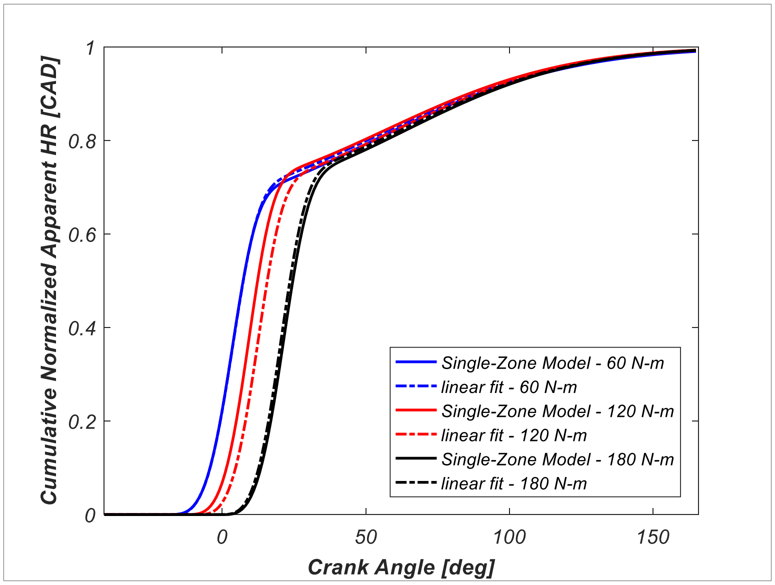

Figure 2.9 Cumulative normalized apparent heat release, direct calculations vs. developed linear model predictions at 2000 rpm.

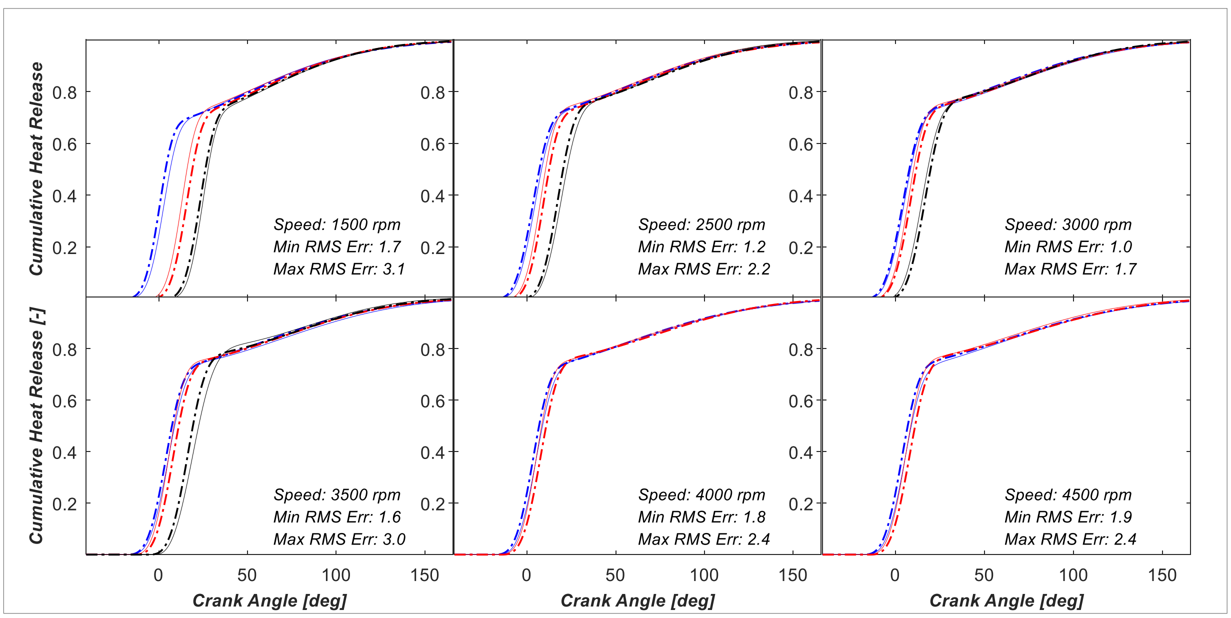

Figure 2.10 Cumulative normalized apparent heat release, direct calculations versus developed linear model predictions – all cases studied; solid and dash-dot lines represent the experiments and numerical predictions, respectively. In each subplot, the traces for the cumulative heat release gradually shift to the right, as loads increase.

2.6 Heat Release Analysis of a DM-TJI Engine

As mentioned earlier, the work presented in this chapter briefly studies the heat release behavior of a Dual Mode, Turbulent Jet Ignition (DM-TJI) engine. This analysis ignores the mass and energy transfer between pre- and main combustion chambers and assumes an average single-zone state for the mixture trapped in the cylinder. An in-depth two-zone analysis of a DM-TJI engine is done in Chapter 3 to study the complexity of the problem. However, the current analysis should be able to produce reliable simplified results since the pre-chamber volume in a DM-TJI engine is as small as 3-5% of the volume at TDC, clearance volume [8].

A single-zone heat release analysis was performed on the experimental data obtained from a gasoline-powered, single-cylinder DM-TJI engine at Michigan State University (MSU); the Prototype I DM-TJI engine. Engine specifications can be found in Table 2.4. The engine was operated at 1500 rpm for all the cases studied here. Details of the engine setup and experimental procedure can be found in [8,37]. Figure 2.11 compares the normalized apparent heat release in the DM-TJI engine for a range of gross indicated mean effective pressure ($IMEP_g$) values below 6.5 bar with that of the Ford 1.6-Liter EcoBoost® GDI engine at 1500 rpm and a load of 60 N-m ($IMEP_g$: 5.8 bar).

Table 2.4 Prototype I DM-TJI engine specifications.

Bore	95 mm
Stroke	100 mm
Connecting rod length	190 mm
Compression ratio	12:1
Pre-chamber volume	2700 mm^3 (~0.4% of displacement volume)
Main chamber volume	0.709 L
Fuel injection	High-pressure injectors for both chambers
Fuel type	EPA LEV-II liquid gasoline (both chambers)

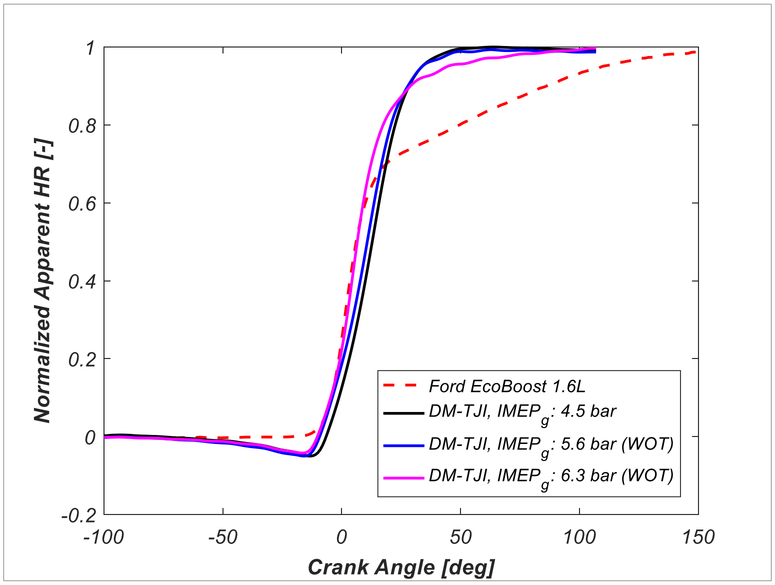

Figure 2.11 Normalized apparent heat release, homogeneous turbocharged GDI engine vs. DM-TJI; speed of 1500 rpm and $IMEP_g$ ~6 bar.

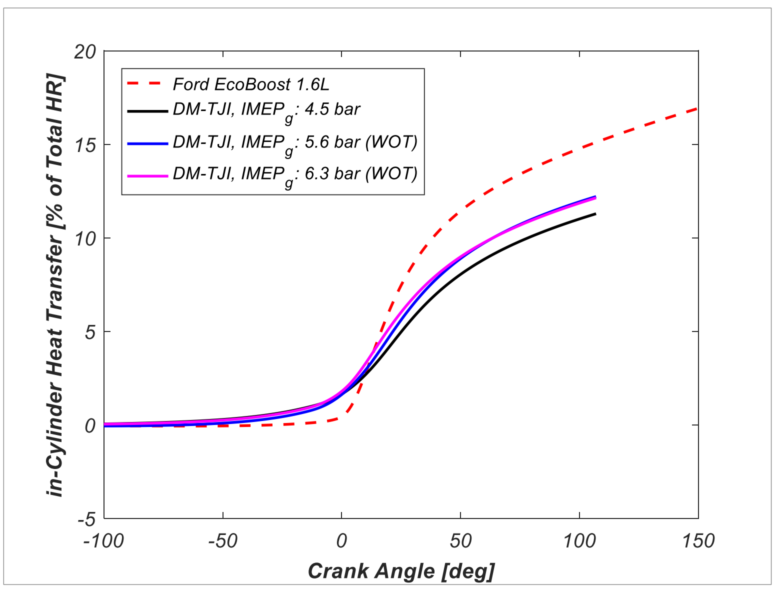

Figure 2.12 Normalized in-cylinder heat transfer, homogeneous turbocharged GDI engine vs. DM-TJI; speed of 1500 rpm and $IMEP_g$ ~6 bar.

The different behaviors of normalized apparent heat release for DM-TJI and GDI engines are evident in Figs. 2.11 and 2.12. In Fig. 2.11, the DM-TJI combustion system is shown to benefit from a rapid pressure rise similar to that in the GDI engine. However, the DM-TJI engine retains the fast burn rate until the end of combustion, while the studied GDI engine entails a slow-paced, diffusion-like phase of combustion after approximately 10 CAD. Additionally, for a given load, lean burn combustion in the DM-TJI engine shows a lower percentage of in-cylinder heat transfer (see Fig. 2.12) compared to a GDI engine, as a result of lower in-cylinder temperatures. Recall that the GDI engine was run at stoichiometry with throttled intake to attain $IMEP_g$ of 5.8 bar. The heat release behavior of a DM-TJI engine is further studied by employing a two-zone analysis in Chapter 3.

2.7 Summary and Conclusion

A combustion model was developed and validated for a homogeneous turbocharged GDI engine operated at a wide range of loads and speeds. Unlike that in a PFI engine, the combustion system of a homogeneous DI engine incurred initial rapid burn pre-mixed combustion followed by a slow diffusion-like phase of combustion. Based on this observation, a double-Wiebe function was employed to model the heat release behavior of the GDI engine. Double-Wiebe variables were further studied to develop a predictive combustion model by using a set of engine parameters. The validity of the predictive combustion model was tested by repeat study of the heat release characteristics of the current GDI engine.

- The semi-predictive combustion model reasonably demonstrated the combustion behavior of this GDI engine in reproducing the in-cylinder pressures. The RMS errors between experiments and numerical pressures were within 2.5% of peak in-cylinder pressures.
- The predictive combustion model was able to capture two phases of combustion for the GDI engine with a maximum RMS error of 3.4% in reproduction of the results obtained from the direct semi-predictive model.

This study is believed to act as a foundation for future work to compare the combustion behavior of a production-based GDI engine with that of a DM-TJI engine. The DM-TJI combustion system offers several benefits in improving the performance of spark ignition engines. Here, a preliminary study was conducted to compare the heat release and heat transfer characteristics of the GDI engine to those of a single-cylinder DM-TJI engine. The DM-TJI engine appears to benefit from a faster energy release and lower heat transfer compared to the GDI engine at the same load and speed. The next chapter involves a two-zone heat release analysis of the DM-TJI engine, while maintaining the mass/energy transfer between pre- and main combustion chambers. This heat release analysis is used in further development of a predictive combustion model for such engines.

CHAPTER 3

DUAL MODE, TURBULENT JET IGNITION ENGINE

3.1 Introduction

The Dual Mode, Turbulent Jet Ignition (DM-TJI) system is an engine combustion technology wherein an auxiliary air supply apart from an auxiliary fuel injection is provided into the pre-chamber [37,38]. The supplementary air supply to the pre-chamber of a DM-TJI system is the main modification to the technology's predecessor, the turbulent jet ignition (TJI) system [39–44]. Upon spark ignition in the pre-chamber, highly energetic chemically active turbulent jets enter the main chamber through a multi-orifice nozzle and ignite the highly lean and/or dilute air/fuel mixture inside the main chamber. High ignition energy, long duration of ignition, and a wide dispersion of ignition sources are essential to achieve fast burn rates in lean and/or highly dilute mixtures [45]. Distributed reaction centers are of particular importance due to the inherent low flame speeds of highly lean/dilute mixtures of reactants. Antoni K. Oppenheim explains the necessity of distributed reaction centers in the most beautiful way in his book "Combustion in Piston Engines: Technology, Evolution, Diagnosis and Control" [46]. He illustrates the concept of propagating flame front using a drawing, done by Jean-Pierre Petit, where the Cal bears were forced to cultivate a field in an overcrowded row at the front [46]; see Fig. 3.1.

He also explains the concept of distributed reaction centers by the same group of Cal bears each cultivating the field on their own in parallel to one another; see Fig. 3.2. The drawing demonstrates the advantage of action in parallel rather than in series, which can be linked to the conceptual difference of a flame front combustion versus the combustion initiated at multiple sites, respectively.

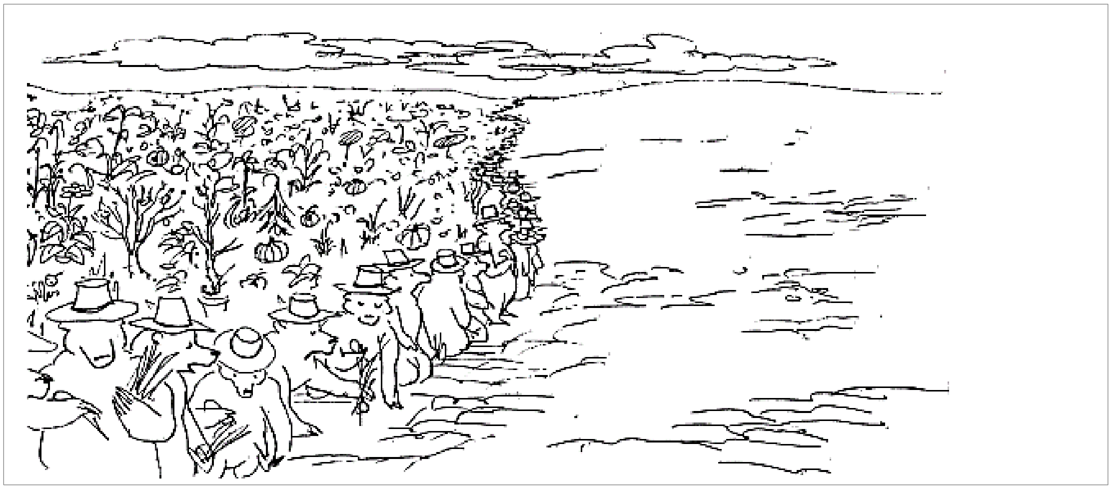

Figure 3.1 The drawing by Jean-Pierre Petit of a group of Cal bears forced to cultivate the field in an overpopulated row [46].

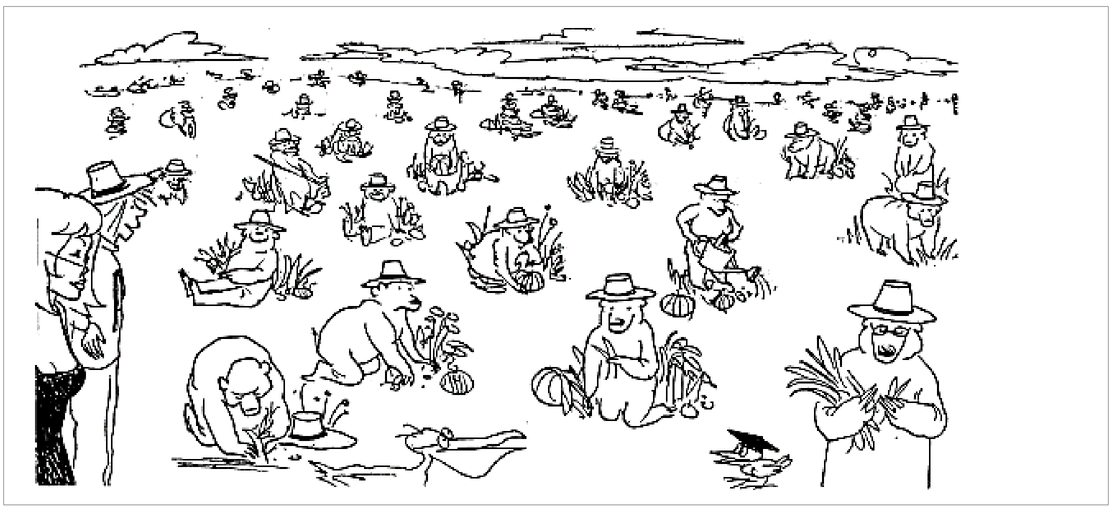

Figure 3.2 The drawing by Jean-Pierre Petit of a group of Cal bears cultivating the field in parallel [46].

The DM-TJI ignition strategy extends the mixture flammability limits by igniting leaner and/or highly dilute mixtures through having higher ignition energy with a longer duration at multiple sites in parallel. Therefore, the DM-TJI system is a promising combustion technology to achieve high diesel-like thermal efficiency at medium to high loads and potentially exceed diesel efficiency at low-load operating conditions. Vedula et al. reported a net thermal efficiency of 45.5%$\pm$0.5% for both lean and near-stoichiometric operations of a gasoline-powered DM-TJI engine [37].

3.2 History

The Dual Model, Turbulent Jet Ignition technology is a modification of the turbulent jet ignition system. The turbulent jet ignition system is among pre-chamber-initiated combustion technologies with small pre-chamber volumes (<3% of the clearance volume). The pre-chamber-initiated combustion can be characterized by having: large or small pre-chamber volumes; auxiliary or no auxiliary pre-chamber fueling (charge stratification); and large or small orifice(s) connecting the pre-chamber to the main combustion chamber [45].

Toulson and colleagues presented a chart of a selection of the research on different pre-chamber-initiated combustion systems [45], which covers studies with both small and large pre-chamber volumes. The small pre-chamber volumes, compared to their larger counterparts, lead to negligible power loss and less hydrocarbon (HC) emissions, as the crevice volume and combustion surface area are reduced [42]. Additionally, as mentioned above, the Dual Model, Turbulent Jet Ignition technology is a modification of the turbulent jet ignition engine with a small pre-chamber. Therefore, the current work will focus on the pre-chamber-initiated combustion systems with small pre-chambers or jet ignition technologies.

The idea of jet ignition was first introduced by Nikolai Nikolaievich Semenov, the winner of the 1956 Nobel prize in chemistry for his work on formulating the chain reaction theory [46]. Semenov later, in collaboration with Lev Ivanovich Gussak, directed extensive research toward the first jet ignition engine which was born under the name of LAG, avalanche activated combustion [46]. As Gussak explained [47,48], the incomplete combustion of a rich mixture inside the pre-chamber results in chemically active reacting jets which cause the main chamber combustion to be fast, stable, and complete. The orifice connecting the pre- to the main combustion chamber works as an extinguisher to the flame initiated inside the pre-chamber, leading to radical species downstream into the main chamber [42,48]. As the pre-chamber flame breaks into chemically active radicals, a number of vortices are created. These vortices carry the active radicals further down into the main chamber resulting in a complete and stable combustion inside the main chamber [48]. Gussak reported “a pre-chamber volume of 2-3% of the clearance volume, an orifice area 0.03-0.04 cm2 per 1 cm3 of pre-chamber volume with an orifice length to diameter ratio of ½” as the most optimized condition for an engine equipped with LAG process [47]. In 1979, Gussak used the LAG process to ignite a lean mixture (normalized air/fuel ratio or lambda of 2) inside the main combustion chamber with a rich (lambda of 0.5) pre-chamber charge. The LAG process was implemented into the powertrain of the Volga passenger vehicle [46]. It was Gussak who showed the importance of radical species in this type of combustion technology.

LAG ignition was also researched by Yamaguchi and colleagues during the 1980s [49]. They studied the LAG process in a divided chamber bomb at the Nogoya Institute of Technology in Japan. Through their study, they identified four different ignition patterns which are possible using the LAG system: well-dispersed burning, composite ignition, flame kernel torch ignition, and flame front torch ignition. Among these, the composite ignition pattern was determined to be the best for lean burn conditions, since it occurred as a result of both active radicals and thermal effects.

Attard and colleagues performed a comprehensive literature study regarding past jet ignition systems from the 1950s to 2007. Table 3.1 represents the study done by this group [42]. A short description for all technologies described in Table 3.1 follows.

Table 3.1 Literature study of past jet ignition technologies with small pre-chamber volume (<3% of cylinder volume at top dead center) [42].

Start Date	Jet Ignition System	Researchers Involved	Reference
1950s	LAG- Avalanche Activated Combustion	L.A. Gussak and colleagues	[50–55]
Late 1970s	Flame Jet Ignition (JPIC- Jet Plume Injection and Combustion, PFJ- Pulsed Flame Jet, PCJ- Pulsed Combustion Jet)	A.K. Oppenheim and colleagues at the University of California, Berkeley and later by E. Murase at Kyushu University	[46,56–64]
1984	Swirl chamber spark plug	Reinhard Latsch at Bosch, Stuttgart	[65]
1992	HAJI- Hydrogen Assisted Jet Ignition	H.C. Watson and colleagues at the University of Melbourne, Australia	[66–74]
1993	PJC- Pulsed Jet Combustion and JDC- Jet Dispersed Combustion	Warsaw University of Technology	[75–77]
1993	HF JI- Hydrogen Flame Jet Ignition	Toyota College of Technology and Gifu University, Japan	[78,79]
1999	APIR (Self-ignition triggered by radical injection)	University of Orleans, France	[80,81]
1999	Scavenged and unscavenged swirl chamber spark plugs	Pischinger and colleagues at Aachen University of Technology and FEV Motorentechnik, GmbH, Germany	[82]
1999	BPI- Bowl Pre-Chamber Ignition	Universitaet Karlsruche and Multitorch GmbH, Germany	[83,84]
2003	Dual-Mode Combustion (PCFA- Premixed Charge Forced Auto-ignition & PJI- Pulse Jet Igniter)	P. M. Najt and colleagues at General Motors	[85]
2005	HCJI- Homogeneous Combustion Jet Ignition	Robert Bosch GmbH	[86,87]
2007	Pre-chamber spark plug with pilot injection	IAV GmbH and Multitorch GmbH, Germany	[88]

Pulsed jet combustion (PJC) was one of the first engine studies using the jet ignition concept performed by Lezanski and colleagues at the Warsaw Institute of Technology [75]. Lezanski et al. studied the effect of a rich (lambda of 0.85)-stoichiometric pre-chamber on the combustion inside the main chamber. Based on their observations, the PJC system produced faster combustion, more rapid pressure rise, and a higher peak pressure relative to the conventional spark ignition engine. However, as the pre-chamber mixture moved closer to stoichiometry, the behavior of the engine equipped with the PJC system showed results closer to those of the conventional spark ignition engine.

Jet plume injection and combustion (JPIC), introduced by Oppenheim and colleagues, slightly differed from PJC systems. PJC technologies used the high pressure generated inside the pre-chamber due to combustion to initiate the radical jet igniters [45,75], while JPICs used its high-pressure injection system to produce the jetting effect. The fuel injector in the JPIC system could inject either fuel or air/fuel mixture into the cavity at the bottom of its combustor [58]. The self-purging capability of JPIC was an advantage over its predecessor, the PJC system. The high-pressure injector of JPIC systems forced the flow out of the pre- into the main combustion chamber. Thus, it eliminated the problem caused by trapped residuals in the cavity of PJC systems. There have been a number of studies investigating the JPIC system in both combustion bombs and rapid compression machines. Toulson reported a number of these studies [71].

The swirl chamber spark plug was first introduced by Reinhard Latsch at Bosch Stuttgart in the early 1980s [65], as an attempt toward simplification of the LAG process. The LAG system included an auxiliary fuel-air supply to the pre-chamber, which was removed in swirl chamber spark plugs. Further studies on the same concept as the swirl chamber spark plug were published by Latsch and colleagues under bowl pre-chamber ignition (BPI) systems [83,84]. The swirl chamber spark plug and BPI solely depended on the piston motion during the compression stroke to direct the main air/fuel mixture into the small pre-chamber cavity, housed inside the spark plug. There were two fuel injection events for the swirl chamber spark plug and BPI systems. The first occurred during the intake stroke to maintain a lean air/fuel mixture inside the main combustion chamber. The second fuel injection event contained only a small amount of fuel (~3% of total fuel mass) and happened during the compression stroke toward the piston bowl. The piston motion would push the additional fuel toward the cavity of the spark plug, causing a rich mixture inside the pre-chamber at the time of ignition.

The hydrogen-assisted jet ignition system (HAJI) was a combustion technology equipped with a small pre-chamber, apart from the main combustion chamber. A small amount of hydrogen (about 2% of the main fuel energy) was injected next to the spark plug inside the pre-chamber to create a rich air/fuel mixture at the time of ignition [45]. The rich mixture inside the pre-chamber would ignite and form chemically active radical jets which penetrated into the main chamber. Chemically active turbulent jets caused by the HAJI system can provide an ignition source of energy more than two orders of magnitude higher than what is found in spark plugs [66]. The lean flammability limit can be extended to lambda (normalized air/fuel ratio) of 5 at wide-open throttle (WOT), with gasoline as the main chamber fuel and a small amount of hydrogen for the pre-chamber [89]. There have been numerous studies in this area, and some of them can be found in Table 3.1. The hydrogen flame jet ignition (HF JI) system [78,79], which was developed at Gifu University and Toyota College of Technology in Japan, was similar to the HAJI system. The authors of these papers conducted an in-depth study to understand the influence level of radical species formed by rich hydrogen combustion inside the pre-chamber compared to jet turbulence in extending the lean limit of stable ignition. The turbulence caused by jets, as they found, played a larger role in combustion stability in lean limits.

The idea of self-ignition triggered by radical injection (APIR) [80,81] was similar to the basis of the pulsed combustion jet (PCJ) born at the University of California, Berkeley. The APIR system, like PCJ technology, benefited from smaller-hole orifices which were used to quench flame propagation and simultaneously to prevent combustion from reappearing in the vortex of jets going from pre- to the main combustion chamber [45]. The main difference lay in the number of orifices connecting the pre- to the main combustion chamber. The APIR system increased the number of orifices for radial seeding of the chemically active turbulent jets inside the main chamber.

A dual-mode combustion process [85] patented by Paul Najt and colleagues at General Motors included premixed charge forced auto ignition (PCFA) as its first mode of combustion for light loads and speeds. Additionally, for higher loads and speeds, a conventional second mode of combustion was utilized by igniting a premixed mixture with spark ignition and/or pulse jet ignition (PJI). The dual-mode combustion process aimed to overcome the known limitations of homogeneous charge compression ignition (HCCI) systems, such as unpredictability of charge ignition timing (combustion phasing) and technology limitations at higher loads and speeds. The PCFA mode of combustion employed pulse jet ignition to ignite an ultra-dilute, pre-mixed charge in the main combustion chamber. The PJI system would work like a pre-chamber-initiated combustion by forcing a spark-ignited jet of hot reacting fuel mixture from a pre-chamber into the ultra-dilute charge of the main chamber [85].

Homogeneous combustion jet ignition (HCJI) [86,87], introduced by Kojic et al. of Robert Bosch GmbH, was another innovation in the world of jet ignition technologies. Like the dual-mode combustion of Paul Najt and colleagues, HCJI was an attempt to control the combustion phasing of HCCI engines. The HCJI system contained two small pre-chambers which were coupled to the main chamber. Each pre-chamber had its own "pre-chamber piston" [45]. As there was no spark plug into the pre-chamber, small and precisely-controlled pistons of the two pre-chambers managed the start of combustion inside the pre-chamber through auto-ignition. The connection between pre- and main combustion chambers was maintained using two microvalves which were closed till early compression inside the main chamber. The valves had been opened by the time the pre-chamber combustion was started, so hot gas jets initiated by auto-ignition of the pre-chamber could induce a second auto-ignition inside the main combustion chamber.

At the end of combustion cycle, a large quantity of residual gas could remain in the pre-chamber due to improperly scavenged combustion products [88]. The pre-chamber spark plug with pilot injection was an attempt to avoid the problems caused by improperly scavenged pre-chamber of a jet ignition technology. The pilot fuel was injected during the intake stroke with an aim of purging the pre-chamber. The amount of pilot fuel injected would vary based on injection pressure and the operating condition. An air/fuel mixture was, then, formed inside the pre-chamber during the compression stroke as the air/fuel mixture from main combustion chamber was pushed into the pre-chamber. The initiation of combustion inside the pre-chamber occurred by a spark event and the jets generated would pass through the holes connecting the pre- to the main chamber. Combustion inside the main chamber occurred as a result of hot, chemically active turbulent jets from the pre- to the main combustion chamber. Getzlaff and colleagues studied several gaseous fuels [88] to purge the pre-chamber, including methane and hydrogen. The most promising results were obtained using hydrogen as the pilot fuel for the pre-chamber.

Apart from studies reviewed by Attard and colleagues [42], presented in Table 3.1 and explained above, there are a number of other works to discuss regarding pre-chamber-initiated combustion systems with small pre-chambers (<3% of the clearance volume) or jet ignition technologies.

In 2005, Harold Durling patented an "igniter for internal combustion engines operating over a wide range of air fuel ratios" [90]. The system introduced mainly included: "an internal cavity disposed substantially within the igniter body, an internal spark gap disposed substantially within the internal cavity, an external spark gap disposed substantially on an exposed surface of the igniter body, and a fuel charge delivery system for delivering a fuel charge to the internal cavity" [90]. The patent also contained a method of operation for internal combustion engines by determining a load threshold within the range of loads available for IC engines. The engine could operate in a spark-ignited mode for higher loads while the determined load threshold was not attained. For lower loads, however, the engine would be operated in a homogeneous charge compression ignition (HCCI) mode of operation as the determined load threshold was met. In the spark-ignited mode of operation, the igniter system worked as a torch jet spark plug, patented by Harold Durling in 1995 [91]. The spark plug ignited the air/fuel mixture pushed from the main combustion chamber to the internal chamber within the igniter body (the pre-chamber) during compression. As a result of combustion inside the pre-chamber, a jet of partially combusted fuel was generated and passed the orifice connecting the pre- to the main combustion chamber and ignited the air/fuel charge inside the main chamber. Additionally, the external spark gap, which was disposed substantially on an exposed surface of the igniter body, contributed to a rapid and full combustion of the air/fuel mixture contained within the main combustion chamber. In the homogeneous mode of operation, the lean air/fuel mixture inside the main chamber was forced into the pre-chamber. At or just before ignition, a small amount of air/fuel mixture was delivered to the pre-chamber through the fuel delivery system in order to maintain a rich mixture inside the pre-chamber. At the time of ignition, the internal and external spark gap fired in series, with the internal event happening a few micro-seconds in advance. As a result, the rich mixture inside the pre-chamber was ignited and formed the torch jet, igniting the lean air/fuel mixture inside the main chamber. The resulting combustion of the main charge in the HCCI mode of operation was primarily caused by compression, but it was triggered by the torch jet discharged from the pre- to the main combustion chamber. Durling also patented a directed jet spark plug in 2001 [92], which was a modification of the torch jet spark plug. In a directed jet spark plug, the orifice connecting the internal cavity within the igniter body (the pre-chamber) to the main chamber was oriented so that its axis was not parallel to the longitudinal axis of the spark plug. The inclination of the orifice caused the torch jet to be selectively directed to any region within the main combustion chamber.

In 2007, David Blank of HCRI Technologies Intl. patented a process called homogeneous combustion radical ignition (HCRI) or partial HCRI, for enhancing homogeneous combustion and improving ignition in rotary and reciprocating piston IC engines [93]. The method included providing the plurality of radical species generated in at least one prior cycle in a number of secondary chambers coupled to the main combustion chamber. The method also included communicating of secondary chambers with the main combustion chamber through small conduits. Additionally, the method regulated the quantities of radical ignition species generated for and conveyed to the later cycle. The idea points to the possibility that, if compression ratios (CRs) were kept within the normal CRs for diesel engines and heat losses were reduced, the hydrogen IC engine may be made to run only on one mode of operation, namely radical species [94]. An older study by Blank and Pouring showed the usage of micro-chambers with no auxiliary fueling as the secondary chambers for the HCRI system [95]. A more recent work, however, studied the HCRI system with a number of mini-chambers and an auxiliary fuel delivery system [94]. More details regarding the HCRI process and studies done in this area can be found in [93].

In 2012, William Attard of MAHLE Powertrain patented a “turbulent jet ignition pre-chamber combustion system for spark ignition engines” [39]. The turbulent jet ignition (TJI) was an ignition system for internal combustion engines. The ignition system included: “a housing, an ignition device, an injector, and a pre-chamber having a nozzle disposed spaced from the proximal portion of the pre-chamber” [39]. The turbulent jet ignition presented by MAHLE Powertrain was built on a number of studies regarding TJI systems [40–42,44] in addition to previous works completed in this area. The main objective of a TJI system was to make the technology more feasible compared to other laboratory-based jet ignition systems described above. Additionally, the system was developed to operate on readily available commercial fuels such as gasoline, propane, and natural gas [45]. The list below highlights some of the defining features for the MAHLE TJI system [40–42,44,45]:

- Very small pre-chamber (~2% of the clearance volume)

- Pre-chamber connected to main chamber by one or more small orifices (~1.25 mm in diameter)
- Separate auxiliary pre-chamber direct fuel injector
- Main chamber fuel injector (port fuel injector (PFI) or direct injector (DI))
- Spark discharge-initiated pre-chamber combustion
- Use of readily available commercial fuels for both main and pre-chambers

Attard and colleagues reported a peak 42% net thermal efficiency for a TJI system mounted on a GM (General Motors) Ecotec 4-valve pent roof combustion system [40]. The 42% efficiency corresponded to a ~6 bar net mean effective pressure (NMEP) at a speed of 1500 rpm with a ~1.6 normalized air/fuel ratio (lambda). The reported thermal efficiency was associated with an 18% improvement in fuel consumption of a lean-operated TJI system compared to conventional stoichiometric spark ignition engines at the same load and speed [40].

3.3 Objective

The TJI systems, as mentioned earlier, have proved a high level of improvement in thermal efficiency compared to conventional IC engines. However, TJI systems face some complications when it comes to engine-out emissions. One of the early challenges of the three-way catalytic converter (TWC), and indeed, one that persists today, is the conversion efficiency of a TWC for nitrogen oxides (NOx). This efficiency is extremely low if the air/fuel ratio moves even slightly toward the lean limit. Figure 3.3 shows the conversion efficiency of a TWC for hydrocarbon (HC), carbon monoxide (CO), and NOx versus the air/fuel ratio (the figure is directly taken from the work by Gandhi et al. [96]). As one can see, the conversion efficiency for NOx species sharply decreases if the air/fuel ratio moves in the slightest toward the lean side of the window. The basic demands of higher technologies in IC engines come from high brake thermal efficiency with low engine-out emissions, while maintaining a low investment and maintenance cost. The TJI systems running on excess air as diluent (lambda>1) make the use of a TWC nearly impossible or at least, it must be used coupled with a rather complex deNOx system such as the selective catalytic reduction (SCR) [97] or NOx traps. A more complex aftertreatment system such as SCR adds to the investment and maintenance cost of an engine, and thus the main criteria are not met. A solution to this problem is operating the engine at stoichiometry, with excess exhaust gas recirculation (EGR) as the diluent.

Using EGR as diluent instead of excess air makes the use of a TWC possible, while maintaining high thermal efficiency at low/medium-load operating conditions (it still avoids throttling of the intake system which is the main cause of the low thermal efficiency at low/medium-load conditions [98]). However, using EGR as diluent further decreases the laminar flame speed compared to that at lean operating conditions, due to lower oxygen concentration in the mixture [97]. Thus, a fast combustion technology is needed under highly dilute operating conditions with excess EGR. The TJI systems cannot operate well under dilute conditions having high level of EGR (up to 40%) as their diluent due to lack of control for maintaining the pre-chamber stoichiometry. Trapped combustion residuals in the pre-chamber of TJI engines cause pre-chamber misfiring and consequently misfires of the main chamber. The pre-chamber combustion residuals can be due to the backflow from the main combustion chamber to the pre-chamber while the engine operates under highly dilute conditions with excess EGR. The trapped residuals in the pre-chamber may also happen as a result of improperly scavenged combustion residuals caused by the pre-chamber combustion itself. This problem becomes worse, as the engine runs under highly dilute conditions.

The Dual Model, Turbulent Jet Ignition (DM-TJI) addresses the aforementioned problem. The DM-TJI system is an engine combustion technology wherein an auxiliary air supply apart from an auxiliary fuel injection, as seen in TJI systems, is provided into the pre-chamber; see Fig. 3.4. The DM-TJI system enhances the stoichiometry control in the pre-chamber which results in combustion stability in the pre-chamber, and consequently combustion stability in the main chamber.

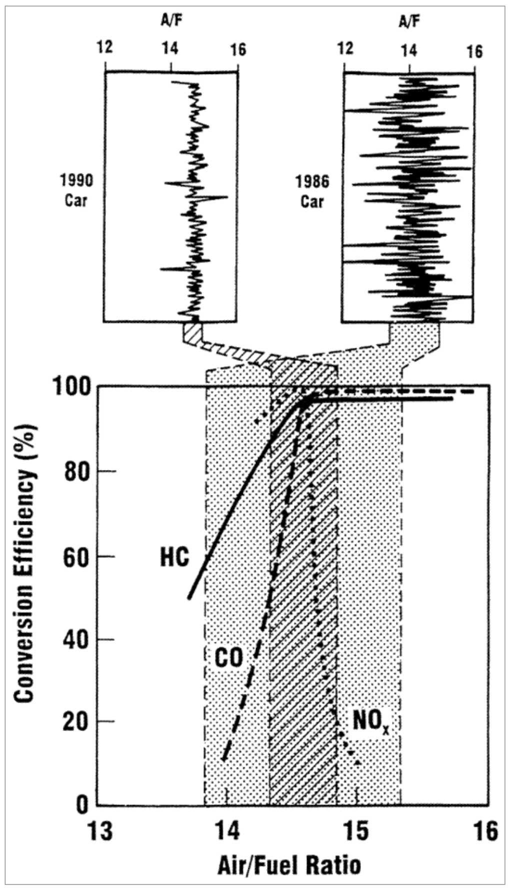

Figure 3.3 Plot for conversion efficiency vs. air/fuel ratio (A/F) with typical air–fuel traces (showing actual variations in air–fuel ratio under closed-loop control) from 1986 and 1990 cars; the figure is directly taken from the work by Gandhi et al. [96]. The stoichiometric air/fuel ratio is about 14.7.

There have been a number of studies on the DM-TJI engine. Vedula and colleagues reported a net thermal efficiency of 45.5%$\pm$0.5% for both lean and near-stoichiometric operations of a gasoline-powered DM-TJI engine [37,48]. The experiments were run on the Prototype I DM-TJI engine at

Michigan State University (MSU). The engine was a single-cylinder optical engine with a flat head. The engine pre-chamber was equipped with a separate fuel injector, while the air delivery to the pre-chamber was provided through a high-pressure DI fuel injector; see Fig 3.5. Engine specifications can be found in the work done by Vedula and colleagues [37]. Song et al. developed a control-oriented combustion model calibrated based on experimental data from the Prototype I DM-TJI engine [99]. This study was a continuation of work published by Song and colleagues [38] on a control-oriented model of a TJI system in a rapid compression machine. Song et al. later expanded the work done in their study of 2017 [99] to a state-space model for a gasoline-powered turbulent jet ignition engine [100]. The former [100] was also calibrated based on experimental data from the Prototype I DM-TJI engine at MSU.

The performance of the Prototype I, although promising, led to a number of questions. The most frequent question regarded power requirements for delivering air to the pre-chamber. Prototype I, while successfully demonstrating the combustion concept, was not a production-viable system. Additionally, the studies to date neither predicted the losses nor projected the expected efficiency of a DM-TJI engine in a multi-cylinder configuration. The Prototype II DM-TJI engine was built and tested in an attempt to answer these questions.

The current study, for the first time, predicts the ancillary work requirement to operate the DM-TJI system. It also includes the path from engine experiments toward model development of a DM-TJI engine. Such a model is essential to project the behavior of a DM-TJI system in a multi-cylinder configuration over the entire engine fuel map. The full map of an engine equipped with the DM-TJI system was fed to the U.S. Environmental Protection Agency (EPA) advanced light-duty powertrain and hybrid analysis (ALPHA) tool. The ALPHA is a "physics-based, forward-looking, full vehicle computer simulation capable of analyzing various vehicle types with different powertrain technologies, showing realistic vehicle behavior" [101] to predict fuel economy and CO2 emission. The results of drive cycle analysis of an engine equipped with the DM-TJI system are presented in Chapter 4.

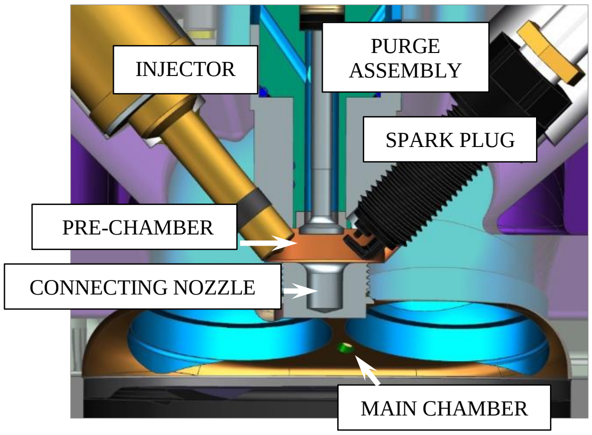

Figure 3.4 Design details for the pre-chamber of the Prototype II DM-TJI engine.

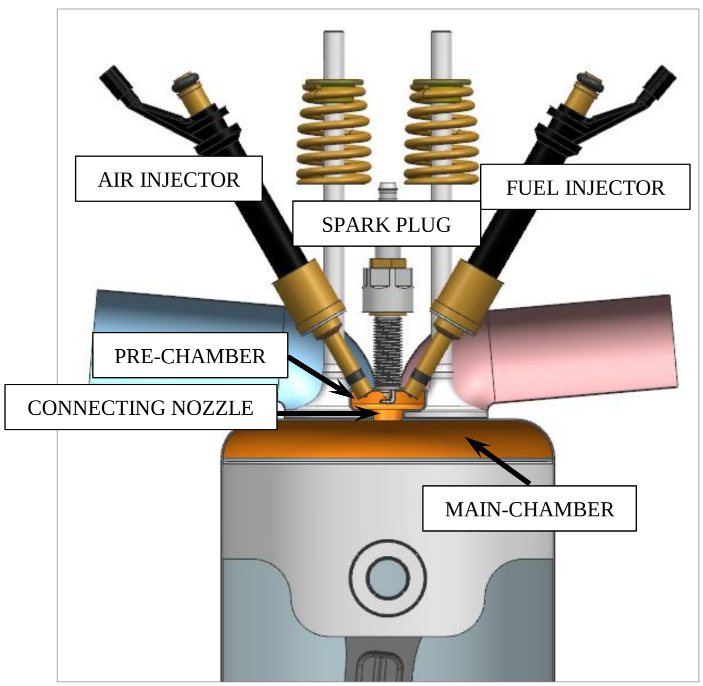

Figure 3.5 Design details for the pre-chamber of the Prototype I DM-TJI engine.

This chapter is organized as follows. The experimental arrangement for the Prototype II DM-TJI engine is first described. After that, the modeling framework for the system-level simulation is explained, followed by the approach used in the model calibration. Experimental and numerical results are presented and discussed. Conclusions are drawn in the last section.

3.4 Experimental Arrangement

3.4.1 Experimental Setup

The experiments were performed on a single-cylinder optical engine of the Prototype II DM-TJI engine. Apart from geometrical alterations, the main difference between the first and second prototypes lies in the way that air is provided to the pre-chamber. The first prototype of the DM-TJI engine maintained the pre-chamber charge stoichiometry, using the pre-chamber auxiliary fuel and air injections. Bosch DI fuel injectors were used for both fuel and air delivery to the pre-chamber [37]. The current DM-TJI engine, Prototype II, substitutes the pre-chamber air injector with a small hydraulically-controlled poppet valve, enabling pre-chamber purge with a modest work input; see Fig. 3.6.

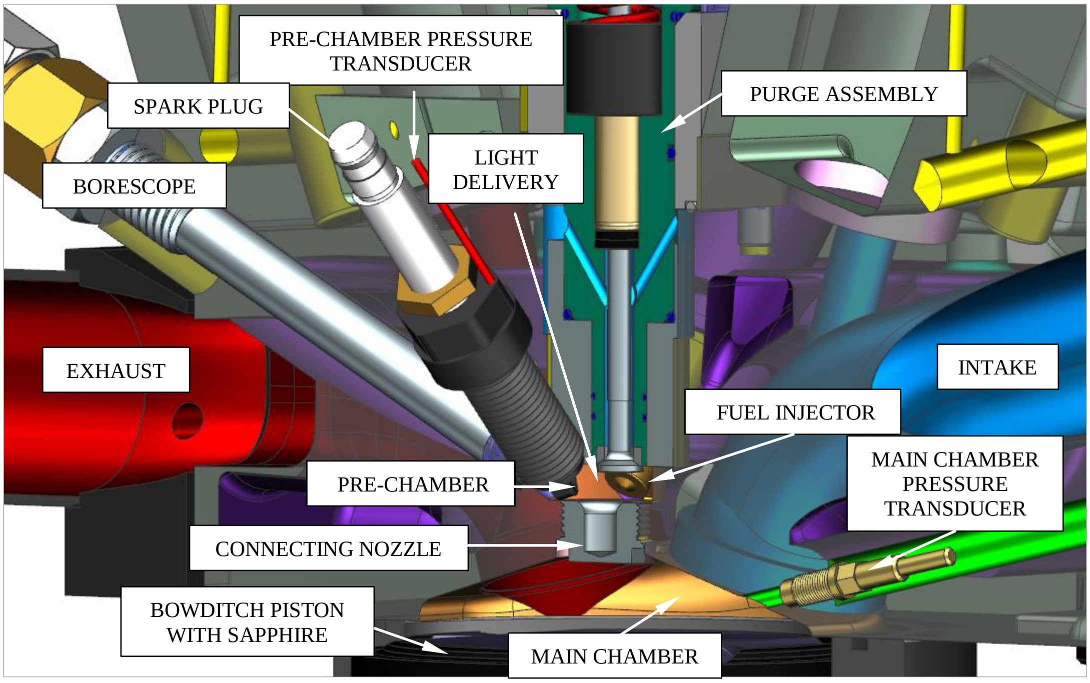

Figure 3.6 Prototype II DM-TJI engine architecture.

The Prototype II DM-TJI engine is an optically accessible engine with a modern pentroof head. The engine head was modified to account for the pre-chamber of the DM-TJI engine; see Fig. 3.6. The engine houses a Bowditch piston assembly with a sapphire window. The piston utilizes production piston rings in conjunction with an oiled felt ring for lubrication. The engine was pre-heated for all the experiments by flowing a 50:50 ethylene glycol-water mixture through its flow passages. Table 3.2 shows the engine specifications.

Table 3.2 Prototype II DM-TJI engine specifications.

Bore	86 mm
Stroke	95 mm
Connecting rod length	170 mm
Compression ratio	12:1
Pre-chamber volume	2532 mm^3 (~5% of clearance volume at TDC)
Main chamber swept volume	0.552 L
Fuel injection	High-pressure injectors for both chambers

Experimental data were recorded for the purpose of model calibration and understanding engine behavior. A measuring spark plug with integrated pressure sensor, Kistler 6115CF-8CQ01-4-1, was employed for the pre-chamber pressure measurement. Main chamber pressure was measured separately using a second pressure sensor, Kistler 6052A. Measured differential pressures of pre- and main chambers were pegged to the averaged intake manifold pressure over 10 CAD starting at -180 crank angle degree after top dead center of fire (CADaTDCF). A Fiat Chrysler Automobiles (FCA) 3 bar manifold air pressure (MAP) sensor and a Kistler sensor, 4045A5, were used to measure the intake and exhaust manifold pressures, respectively. The Kistler sensor for measuring the exhaust pressure was cooled down during the experiments by running the 50:50 ethylene glycol-water mixture through its housing.

A Meriam laminar flow element (LFE), Z50MJ10-11, was installed to measure the air flow to the pre-chamber. A multivariable digital transmitter, MDT500 by Meriam Process Technologies, was used to transfer the LFE reading to the Meriam software development kit (SDK) [102]. The SDK includes libraries for calculating flow rate and for communicating with the LFE device on the test bench to take measurements and access configuration options. The low-range LFE (0.035 SCFM – 1 SCFM), used to measure the pre-chamber air flow, was connected to the air valve with a flow dampener in between. The flow dampener was aimed to dampen the flow pulsations upstream from the pre-chamber air valve for a better flow measurement. Figure 3.7 represents assembly of the dampener system used in this study.

Type K thermocouples were added to the intake manifold, exhaust manifold, coolant, and the oil passage for the air valve assembly to measure the temperatures. Ambient pressure, temperature, and the relative humidity were measured using omega sensors (Omega PX409 and Omega HX93BC-RP1). Figure 3.8 shows the Prototype II DM-TJI engine on the test bench at the MSU Energy and Automotive Research Laboratory (EARL).

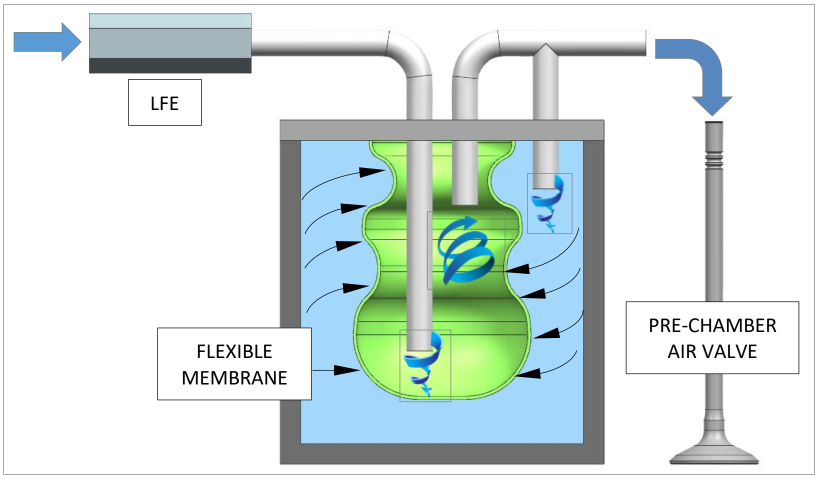

Figure 3.7 Schematic of the dampener for the flow measurement of the pre-chamber purge valve assembly. The inside and outside of the flexible membrane are filled by air at approximately the same pressure. The flexible membrane absorbs the flow pulsations upstream from the air valve, leading to a reliable flow measurement.

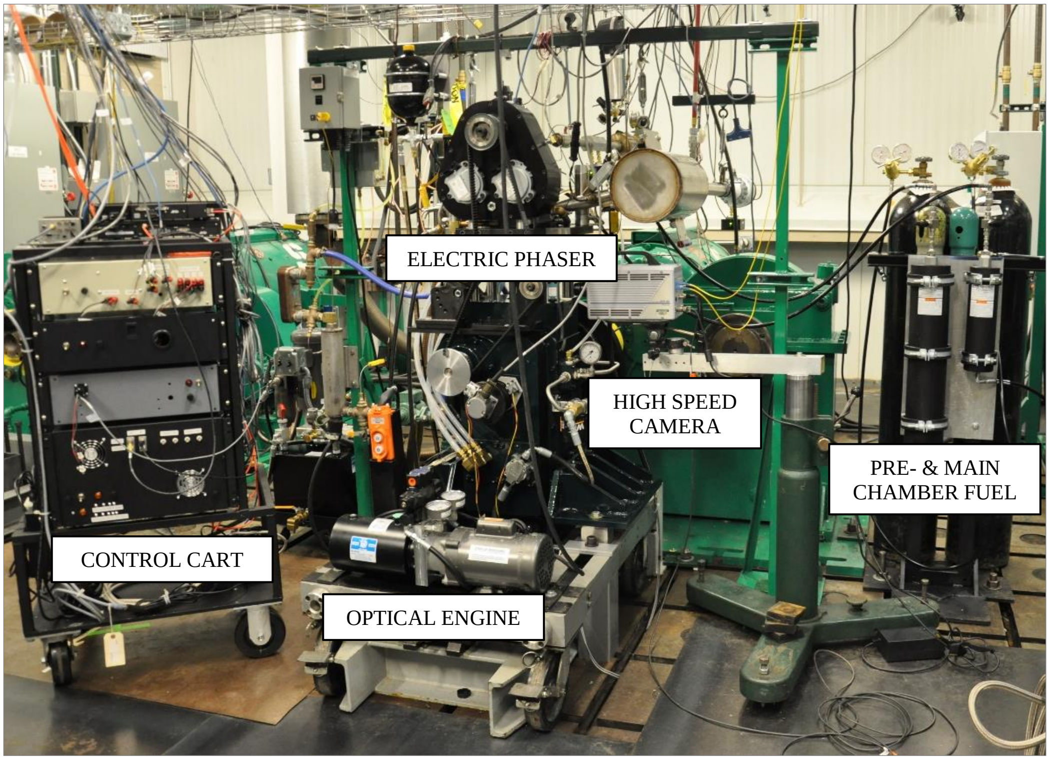

Figure 3.8 Prototype II DM-TJI engine at MSU EARL.

3.4.2 Data Set Definition

The data logged included pre-chamber valve mass flow rate, intake/exhaust manifold pressures, pre-chamber valve upstream pressure, ambient pressure/temperature/relative humidity, intake/exhaust manifold temperatures, coolant temperature, temperature of the oil passage for the pre-chamber air valve, in-cylinder pressures, and the combustion characteristics calculated by CAS.

3.4.3 Data Collection Procedure

Two data acquisition systems were used. The first was a National Instruments (NI) data acquisition device for low-frequency data and the second was an A&D Technology Combustion Analysis System (CAS) for high-frequency data acquisition. CAS data were sampled at 1 crank angle resolution. The low-frequency data acquired by NI system were logged through NI VeriStand at 100 Hz.

Apart from pre-heating the engine using the 50:50 ethylene glycol-water mixture, the engine was run for 200 cycles closer to stoichiometry (lambda~1.4) at the beginning of each experiment to warm up the engine. The same warm-up process was employed for all cases studied. After that, the engine was run for 600 cycles at each operating condition, with the data being processed at the last 200 cycles.

3.5 Numerical Approach and Model Development

3.5.1 Modeling Platform

Engine modeling can be broadly separated into two different categories: reduced order zero-dimensional/one-dimensional (0D/1D) engine simulation tools and high-fidelity three-dimensional (3D) modeling platforms. The 0D/1D simulation tools are used for engine studies and optimizations, when computationally expensive 3D simulations are impractical, and can be further classified into three sub-categories in the order of increasing physical fidelity and run time [103]: mean-value models, filling-and-emptying models, and wave action (gas dynamic) models.

Mean-value engine models or fast-running models (FRM) neglect the breathing dynamics of the engine and operate on a cycle-by-cycle basis. Models in this category can be easily run many times faster than high-fidelity models to provide the average performance metrics for the engine [103]. Mean-value models can be used as plant models for software-in-the-loop (SiL) and hardware-in-the-loop (HiL) testing. They can also be coupled with vehicle models for fuel economy, drivability, and other vehicle studies. Nonetheless, mean-value models cannot be used for engine performance development due to lack of details during the combustion event such as heat release rate and the engine in-cylinder pressure. The inaccuracy caused by generalization in mean-value models can be amplified during transient operation of the engine. Hendricks and Sorenson reported an accuracy of ±2% over the entire operating range of an engine [104]. They also conducted a series of experiments at widely separated points in the operating range of the engine and concluded that the transient accuracy of the model is comparable to its steady-state predictions. Hunt and colleagues, however, estimated a more conservative accuracy for the mean-value models [105]. They reported a ±10-15% accuracy based on their results on an adapted form of a four-cylinder version of the BMW Valvetronic (variable valve lift system) engine.

Filling-and-emptying models simulate the breathing dynamics of the engine with some simplifications. In these models, the manifolds (or sections of manifolds) are characterized by finite volumes where the mass of gas can increase or decrease with time [26]. The filling-and-emptying models can run on much finer timescales than those of mean-value models, often on a crank-resolved basis [103]. Models in this category range from treating the whole intake/exhaust system as a single volume to dividing these single volumes into many subsections. The run time will increase, as the number of sub-volumes increases. The models solve for mass and energy equations developed for open thermodynamic systems, coupled with information on the mass flow rates in and out of each sub-volume with each sub-volume containing gas in a uniform state [26]. These models are coupled with a thermodynamic analysis of the in-cylinder processes. Filling-and-emptying models can provide crank-resolved rates of heat release and in-cylinder pressures. However, such models cannot provide the spatial variation of pressure (and other gas properties) caused by unsteady gas dynamics in intake/exhaust manifolds.

Wave action (gas dynamic) models run on the same time resolution as filling-and-emptying models. However, they comprise finer spatial resolutions compared to those of filling-and-emptying models. They include the wave dynamic characteristics of intake/exhaust systems. The overall performance of an induction and exhaust system is dependent on many design parameters including the length and cross-sectional area of both primary and secondary runners, the volume and location of the plenum, and the entrance or exit angle of the runners [26]. Most of these geometrical details are beyond the level of complexity for mean-value or filling-and-emptying models. The geometrical details, mentioned earlier, coupled with the pulsating behavior of the flow in and out of each cylinder, create the gas dynamic effects which can be captured with wave action (gas dynamic) models or more complicated high-fidelity models. Gas dynamic models typically solve for one-dimensional unsteady conservation of mass, momentum, and energy equations. These models use a thermodynamic analysis of the in-cylinder processes to couple with the intake and exhaust systems [26].

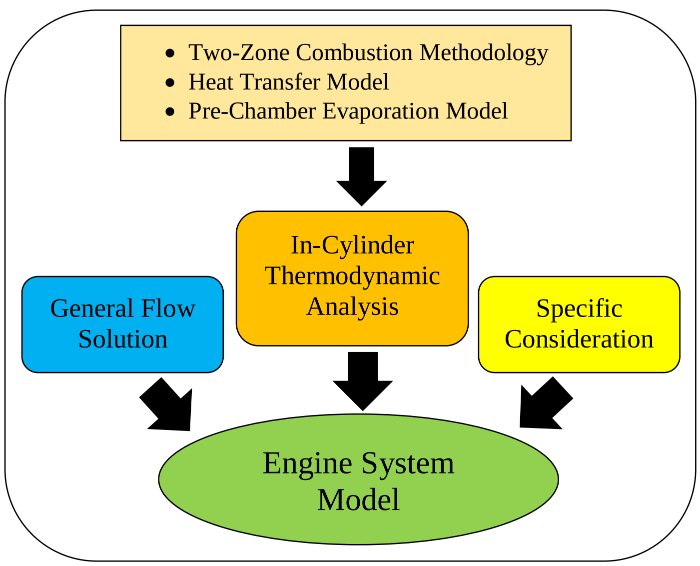

Figure 3.9 Modeling framework for system-level simulation of Prototype II DM-TJI engine.

GT-SUITE/GT-POWER is the industry standard engine performance simulation tool, used by every major original equipment manufacturer (OEM). GT-POWER is used to predict engine performance quantities such as power, torque, air flow, volumetric efficiency, fuel consumption, etc. [106]. Additionally, a calibrated GT-POWER model captures the wave dynamic effects by solving for simplified 1D Navier-Stokes equations. GT-SUITE/GT-POWER, with its capabilities in prediction of engine in-cylinder characteristics and wave dynamic effects, lies among wave action (gas dynamic) engine simulation tools.

The current study employs GT-POWER as its modeling platform. Figure 3.9 presents a conceptual diagram of the modeling framework for the system-level simulation of the Prototype II DM-TJI engine. Each of the modeling considerations prior to a complete engine system simulation is explained, as follows.

3.5.1.1 General Flow Solution

The developed model includes the intake/exhaust systems, the pre-chamber purge valve, the pre-chamber, the main chamber, and the nozzle connecting the pre- to the main combustion chamber. The flow characteristics for all the parts except for pre- and main combustion chambers were determined by solving for 1D Navier-Stokes equations, namely the conservation of mass (Equation 3.1), momentum (Equation 3.2), and energy (Equation 3.3).

$$\frac{dm}{dt} = \sum_{boundaries} \dot{m} \tag{3.1}$$

$$\frac{d\dot{m}}{dt} = \frac{dpA + \sum_{boundaries}(\dot{m}u) - 4C_f \frac{\rho u|u|}{2}\frac{dxA}{D} - K_p\left(\frac{1}{2}\rho u|u|\right)A}{dx} \tag{3.2}$$

$$\frac{d(me)}{dt} = -p\frac{dV}{dt} + \sum_{boundaries}(\dot{m}H) - hA_s(T_{fluid} - T_{wall}) \tag{3.3}$$

where, $\dot{m}$ is the boundary mass flux into the volume; m is the mass of the volume; V is the volume; p is the pressure; ρ is the density; A is the cross sectional flow area; A_s is the heat transfer surface area; e is the total specific internal energy (internal energy plus kinetic energy per unit mass); H is the total specific enthalpy ($H = e + \frac{p}{\rho}$); h is the heat transfer coefficient; T_{fluid} is the fluid temperature; T_{wall} is the wall temperature; u is the velocity at the boundary; C_f is the fanning friction factor; K_p is the pressure loss coefficient (commonly due to bend, taper or restriction); D is the equivalent diameter; dx is the length of mass element in the flow direction (discretization length); and dp is the pressure differential acting cross dx.

The flow solution was carried out by integration of the conservation equations in both space and time. An explicit integration method was used in this study. To ensure numerical stability, the time step was restricted based on the Courant number.

At each time step, the pressure and temperature are calculated in the following order:

- Conservation of mass and energy are first solved to determine the mass and energy in each volume.
- With the volume and mass known, the density is then calculated.
- The equations of state for each species define the density and energy as a function of pressure and temperature. The solver will then iterate on pressure and temperature until it satisfies already calculated density and energy from the previous step.

3.5.1.2 In-Cylinder Thermodynamic Analysis

Thermodynamic zone modeling is used to simplify the complicated processes during combustion with the general idea of practicality, when computationally expensive high-fidelity models are impractical [107]. The current study employed a two-zone analysis for both pre- and main combustion chambers, while the GT-POWER WoschniGT heat transfer model was used to simulate the heat transfer. Additionally, the current model compensates for the pre-chamber evaporation with a two-step fuel injection event. A brief explanation of each of these elements follows.

Two-Zone Combustion Methodology

In a two-zone analysis, one zone represents the unburned mixture before the combustion and a second zone represents the burned mixture after combustion. Thermodynamic properties of the cylinder contents can be quantified more accurately in a two-zone analysis. At the start of combustion, the cylinder is divided into unburned and burned zones. In GT-POWER, all the contents of the cylinder start in the unburned zone, including fuel and internal/external exhaust gas recirculation (EGR). At each time step, the combustion rate of heat release is in charge of mass transfer from the unburned zone to the burned zone. The burn rate is imposed directly to the cylinder object in GT-POWER simulations through predictive, semi-predictive, and non-predictive combustion models. More information can be found in GT-SUITE manuals under "Engine Performance." Once the unburned fuel and associated air are transferred from the unburned zone to the burned zone, a chemical equilibrium calculation takes place for the entire burned zone of analysis. This calculation solves for 13 products of combustion species including N_2, O_2, H_2O, CO_2, CO, H_2, N, O, H, NO, OH, SO_2, and Ar based on all the atoms available to the combustion process. The equilibrium concentrations of these species are highly dependent on the burned zone temperature. Once the new composition of the burned zone is obtained, the total energy of the burned zone is obtained as a summation of internal energy of each individual species. The new temperature and pressure of the burned zone is, then, determined as the energy is always conserved. The two-zone analysis solves for Equations 3.4 and 3.5 at each time step. Equation 3.4 represents the energy balance for the unburned zone, and Equation 3.5 is used for the burned zone calculation.

$$\frac{d(m_u e_u)}{dt} = -p\frac{dV_u}{dt} - Q_u + \left(\frac{dm_f}{dt}h_f + \frac{dm_a}{dt}h_a\right) + \frac{dm_{f,i}}{dt}h_{f,i} \tag{3.4}$$

$$\frac{d(m_b e_b)}{dt} = -p\frac{dV_b}{dt} - Q_b - \left(\frac{dm_f}{dt}h_f + \frac{dm_a}{dt}h_a\right) \tag{3.5}$$

where, m_u, m_f, m_a, and $m_{f,i}$ are the unburned zone mass, the fuel mass, the air mass, and the injected fuel mass; respectively. Moreover, e_u is the unburned zone energy; p is the in-cylinder pressure; V_u is the unburned zone volume; Q_u is the unburned zone heat transfer; h_f is the enthalpy of fuel mass; h_a is the enthalpy of air mass; and $h_{f,i}$ is the enthalpy of injected fuel mass. The subscript "b" denotes the burned zone.

Heat Transfer Model

The GT-POWER WoschniGT heat transfer model was used to simulate the heat transfer term in Equations 3.4 and 3.5. WoschniGT closely matches the classical Woschni correlation without swirl. The most important difference lies in the treatment of heat transfer coefficients when the intake and exhaust valves are open, and intake inflow velocities and exhaust backflow velocities increase the in-cylinder heat transfer. More information can be found in Chapter 2 under "Numerical Approach and Model Development."

Pre-Chamber Evaporation Model

Pre-chamber evaporation modeling is important while injecting liquid fuel directly into the small volume of the pre-chamber. The current model compensates for the pre-chamber evaporation with a two-step fuel release event. A "k" factor was optimized for the fraction of the fuel to be evaporated at the time of injection. The model assumes that the entire fuel injected evaporates during one engine cycle. Thus, to conserve the mass of fuel injected into the pre-chamber, the "$(1-k)$" remained fraction of the fuel will be released as the combustion starts inside the main chamber and pushes the hot reacting air/fuel mixture to the pre-chamber. The second fuel release continues until the mass flow rate from main to pre-chamber reaches its maximum level.

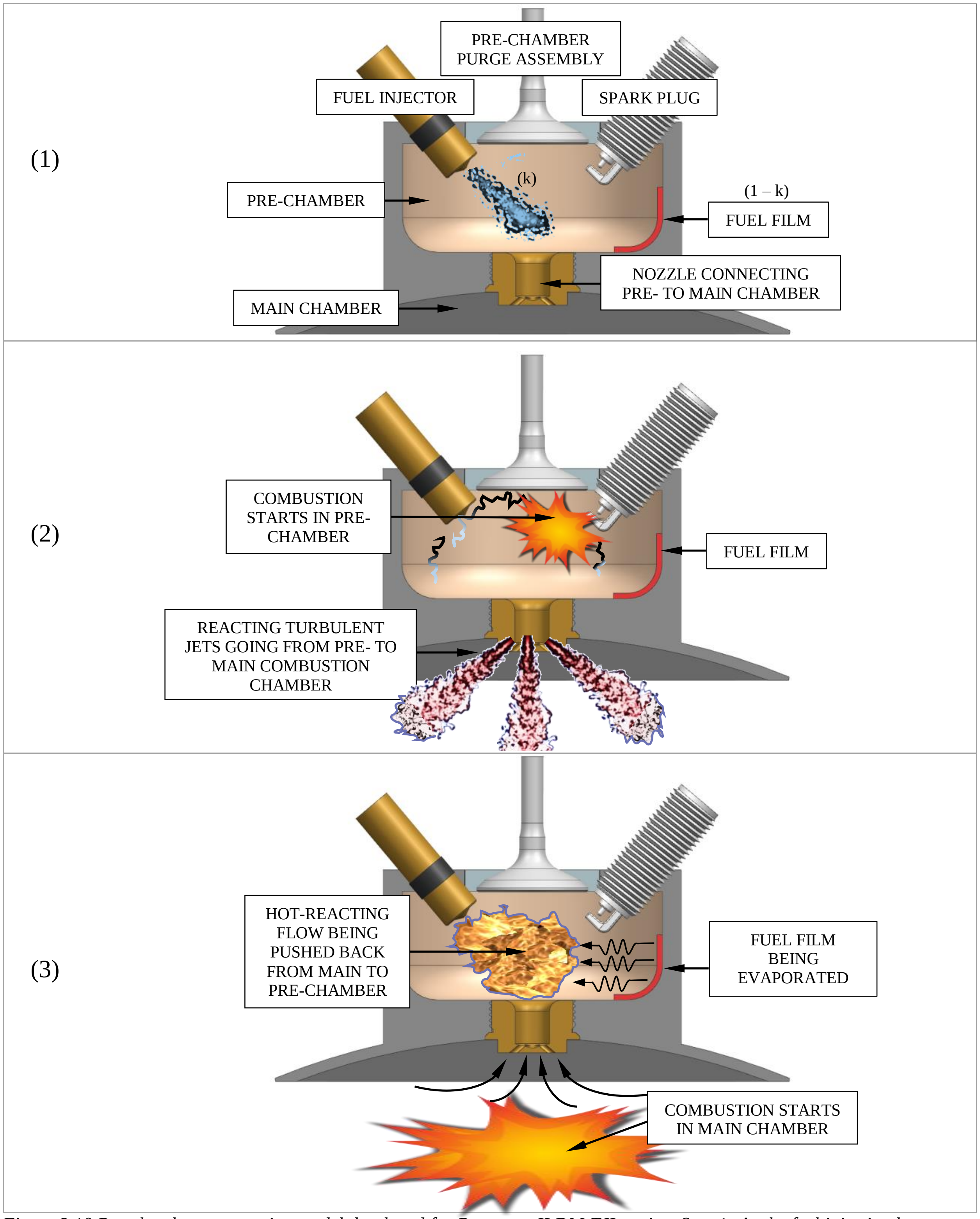

Figure 3.10 Pre-chamber evaporation model developed for Prototype II DM-TJI engine. Step 1: As the fuel injection happens, a portion of fuel will evaporate immediately at the time of injection, "k" factor. The remaining ("1-k" factor), however, will form a thin fuel film on the pre-chamber wall. Step 2: Combustion starts inside the pre-chamber leading to the chemically active turbulent jets entering the main combustion chamber. Step 3: Combustion starts inside the main chamber, leading to the flow being pushed into the pre-chamber. The hot reacting pushed-back flow causes the pre-chamber fuel film to evaporate.

Figure 3.10 depicts the three steps associated with the fuel release inside the pre-chamber. A control mechanism was added to the simulation using GT-POWER control objects to detect the start and end of the second fuel release into the pre-chamber. Figure 3.11 displays a sample prediction of the model for the start and end of secondary fuel release inside the pre-chamber.

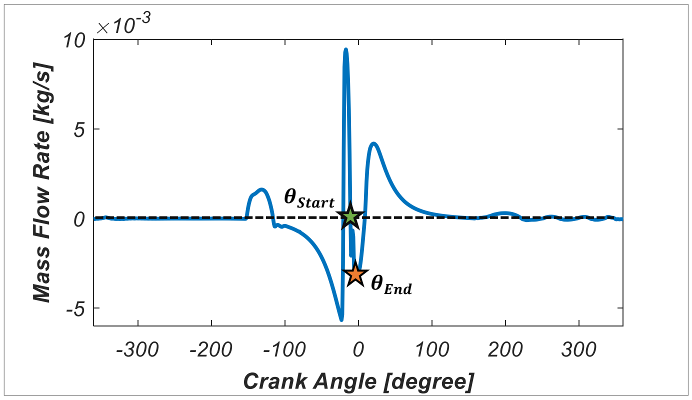

Figure 3.11 Mass transfer between pre- and main combustion chambers. Positive values present the flow in the direction of pre- to the main chamber, while the negative values are for the flow in the opposite direction (from main to the pre-chamber). The blue solid line shows the crank-resolved model prediction of the mass flow rate. The green and orange stars point to the start (θ_{Start}) and end (θ_{End}) of the second fuel release into the pre-chamber, respectively.

3.5.1.3 Specific Considerations

The DM-TJI system, with its specific design requirements, necessitates some custom modeling while using GT-SUITE/GT-POWER as the modeling platform. There are two main areas which need special attention when it comes to modeling the DM-TJI system, compared to other engine technologies:

- Pre-chamber modeling
- Burn dependency between pre- and main chambers

Pre-chamber modeling

Until the end of 2017, GT-SUITE/GT-POWER did not include a template, and subsequently an object, having a constant volume with a place holder for combustion modeling. In their 2018 version, Gamma-Technologies introduced for the first time a pre-chamber template. However, as the pre-chamber template is under development, it is limited on object connectivity. For example, one cannot connect an object to the pre-chamber, which represents the nozzle connecting the pre- to the main combustion chamber. Adding a nozzle connection, although it requires a very small time step due to the small volume of the nozzle, is essential considering the approach used in this study to maintain the correlation between the burn characteristics of the pre- and main chambers. The approach employed requires the crank-resolved mass and enthalpy of the flow going from pre- to the main chamber and vice versa. Such information is not available by using the current pre-chamber orifice connection found in GT-POWER. Additionally, the currently available pre-chamber template is limited on valve connectivity as was needed to model the pre-chamber purge valve of the Prototype II DM-TJI engine.

The current study modeled the pre-chamber of the DM-TJI engine using a GT-POWER engine cylinder template. However, to obtain the constant volume of the pre-chamber, the piston position was defined as a non-moving piston in reference to bottom dead center over the entire engine cycle. Also, the compression ratio (CR) was set to the minimum value allowed as 1.001. The pre-chamber combustion was imposed using a single-Wiebe function [35], with three calibrating parameters: total burn duration ($\Delta\theta_{Pre}$), start of combustion ($\theta_{0,Pre}$), and Wiebe exponent or combustion mode parameter (m_{Pre}). The pre-chamber start of combustion was calculated as spark timing (θ_{Spark}) with some ignition delays ($\Delta\theta_{ignD-Pre}$), Equation 3.7. The pre-chamber ignition delay was defined as a fraction (α_{Pre}) of spark timing, with α_{Pre} being optimized with the rest of the calibrating parameters. Equation 3.6 shows the single Wiebe function used to calculate the mass fraction burned of the pre-chamber ($x_{b,Pre}$). The value of constant a in Equation 3.6 is equal to 6.9, which is obtained assuming the mass fraction burned of 99.9% at the end of combustion [20]. The pre-chamber rate of heat release ($\dot{Q}_{Pre}$) was then calculated as the multiplication of: pre-chamber combustion efficiency (η_{Pre}), instantaneous total mass of fuel in the pre-chamber ($\frac{m_{f,Pre}}{1-x_{b,Pre}}$), fuel lower heating value (Q_{LHV}), and rate of mass fraction burned with respect to crank angle ($\frac{dx_{b,Pre}}{d\theta}$); see Equation 3.8.

$$x_{b,Pre} = 1 - \exp\left[-a\left(\frac{\theta - \theta_{0,Pre}}{\Delta\theta_{Pre}}\right)^{m_{Pre}+1}\right] \tag{3.6}$$

$$\theta_{0,Pre} = \theta_{Spark} + \Delta\theta_{ignD-Pre} = \theta_{Spark} + \alpha_{Pre}|\theta_{Spark}| \tag{3.7}$$

$$\dot{Q}_{Pre} = \eta_{Pre}\frac{m_{f,Pre}}{1 - x_{b,Pre}}Q_{LHV}\frac{dx_{b,Pre}}{d\theta} \tag{3.8}$$

where, $m_{f,Pre}$ is the instantaneous mass of fuel trapped in the pre-chamber at each crank angle.

Burn dependency between pre- and main chambers

The burn dependency between pre- and main combustion chambers was adapted from the already developed and tested concept of a parameter-varying Wiebe function [38,99] with a number of readjustments. Song and colleagues reported a high correlation between the mass flow rate of the turbulent jets and the rate of combustion in the main chamber [38,99]. Thus, they linked the intensity of the turbulent jets to their combined mass flow rate. In a parameter-varying Wiebe function, the intensity of turbulent jets is the term to maintain the burn dependency of the pre- to the main combustion chamber. The simplicity of the correlation was logical toward a control-oriented model.

The current study linked the intensity of turbulent jets to the energy release from pre- to the main chamber, as a result of pre-chamber combustion. After all, the ignition energy and the long duration of ignition are two out of three elements of a fast burn combustion caused by a DM-TJI system. Equations 3.9, 3.10, 3.11, 3.12, 3.13, 3.14, and 3.15 represent the corresponding mathematics. The mass fraction burned of the main chamber ($x_{b,Main}$), calculated in Equation 3.14, was translated into the main chamber rate of heat release in Equation 3.15.

$$\dot{E}_{tur} = \dot{m}_{tur} C_p T_{tur} \tag{3.9}$$

$$\dot{E}_{tur}{}^{+} = \begin{cases} \dot{E}_{tur} & \dot{m}_{tur} \geq 0 \; and \; \theta_{Spark} < \theta < 0 \\ 0 & \dot{m}_{tur} < 0 \end{cases} \tag{3.10}$$

$$b = \beta . \dot{E}_{tur}{}^{+} + 1 \tag{3.11}$$

$$\theta_{ign-b} = \theta_{0,Main} - \int_{\theta_0}^{\theta} [b-1] d\theta \tag{3.12}$$

$$\theta_{0,Main} = \theta_{0,Pre} + \Delta\theta_{ignD-Main} = \theta_{0,Pre} + \alpha_{Main} |\theta_{Spark}| \tag{3.13}$$

$$x_{b,Main} = 1 - exp\left(-a\left(\frac{\theta - \theta_{ign-b}}{\Delta\theta_{Main}}\right)^{m_{Main}+1}\right) \tag{3.14}$$

$$\dot{Q}_{Main} = \eta_{Main} \frac{m_{f,Main}}{1 - x_{b,Main}} Q_{LHV} \frac{dx_{b,Main}}{d\theta} \tag{3.15}$$

In these equations, $\dot{m}_{tur}$ is the mass flow rate of turbulent jets, C_p is the specific heat at constant pressure; T_{tur} is the temperature of turbulent jets; $\dot{E}_{tur}$ is the energy of turbulent jets; θ_{Spark} is the crank angle degree at the time of spark timing; θ is the instantaneous crank angle degree; $\dot{E}_{tur}{}^{+}$ is the filtered energy term to consider the effect of turbulent jets after spark timing and before top dead center of fire (0 crank angle degree), while the flow direction is from pre- to the main combustion chamber; β is a calibrating parameter to maintain the burn dependency of the pre- to the main chamber; b is the mathematical expression for the intensity of turbulent jets [38,99]; $\theta_{0,Main}$ is the main chamber start of combustion (SOC) which is calculated as pre-chamber SOC with some ignition delays ($\Delta\theta_{ignD-Main}$); $\Delta\theta_{ignD-Main}$ is the main chamber ignition delay which is defined as a fraction (α_{Main}) of spark timing with α_{Main} being optimized with the rest of calibrating parameters; θ_{ign-b} is the parameter-varying SOC; $\Delta\theta_{Main}$ is the main chamber total burn duration; m_{Main} is the combustion mode parameter or Wiebe exponent for the main chamber; $x_{b,Main}$ is the main chamber mass fraction burned; η_{Main} is the main chamber combustion efficiency; $m_{f,Main}$ is the instantaneous mass of fuel trapped in the main chamber at each crank angle; Q_{LHV} is the fuel lower heating value; $\frac{dx_{b,Main}}{d\theta}$ is the main chamber rate of mass fraction burned; and $\dot{Q}_{Main}$ is the main chamber rate of heat release.

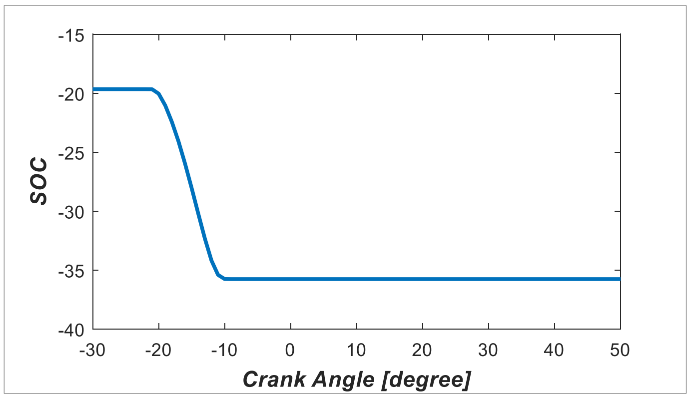

Figure 3.12 Variable start of combustion (SOC) of parameter-varying Wiebe function.

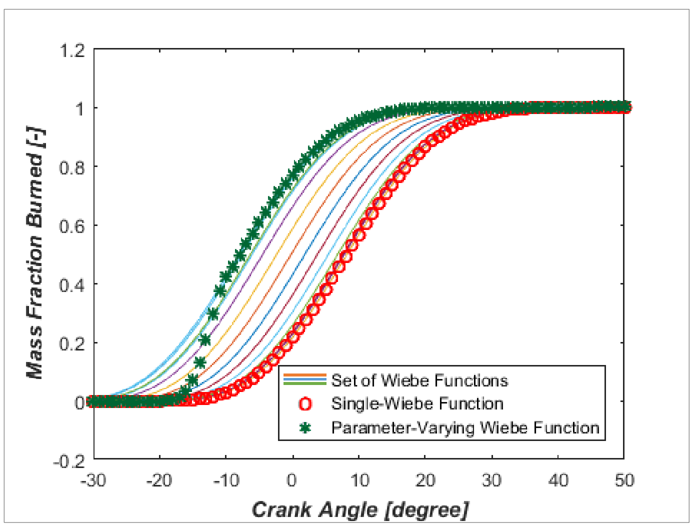

Figure 3.13 Parameter-varying Wiebe function vs. single-Wiebe function. The red circles display the single-Wiebe function, while the green stars represent the parameter-varying Wiebe function obtained using the variable SOC shown in Fig 3.12. The multi-color solid lines are the single-Wiebe curves associated with the variable SOCs.

The parameter-varying Wiebe function advances the mathematical SOC of the Wiebe function (θ_{ign-b}) based on energy release of the turbulent jets at each crank angle. While the mathematical

SOC is shifted, the physical SOC ($\theta_{0,Main}$) is kept constant with an ignition delay ($\Delta\theta_{ignD-Main}$) with respect to SOC inside the pre-chamber. Figure 3.12 shows a sample calculation for the variable SOC. Figure 3.13 represents the mass fraction burned of the parameter-varying Wiebe function using the variable SOC shown in Fig. 3.12, compared to a single-Wiebe function. The parameter-varying Wiebe function and the single-Wiebe function shown in Fig. 3.13 have the same physical SOC ($\theta_{0,Main}$). This burn dependency was imposed using available control templates/objects on the GT-POWER platform.

3.5.2 Calibration of Engine System Model

The engine system model developed includes the detailed geometry of the pre- and main combustion chambers, along with the intake and exhaust systems. The test cell pressure, temperature, and relative humidity measured were set as boundary conditions for both the intake and exhaust systems. The wall temperature of the intake port was set to 360 K which is the temperature associated with the 50:50 ethylene glycol-water mixture through flow passages of the engine. The wall temperature of the exhaust port was defined as 450 K at wide-open throttle and 400 K at partially throttled conditions. The heat transfer multiplier for the intake/exhaust ports was fixed at 1.5. The wall temperatures for the intake system upstream of the intake port were assumed to be the test cell temperature. The wall temperatures downstream from the exhaust port were calculated using the GT-POWER wall temperature calculator.

The amount of fuel injected for the main combustion chamber was obtained by calibration of the fuel injector at atmospheric pressure. For all the experiments, the main fuel injection happened at -360 crank angle degree after top dead center of fire (CADaTDCF). For the calibration points at wide-open throttle, the in-cylinder pressure at the time of main fuel injection is around atmospheric pressure. The changes in fuel flow due to lower in-cylinder pressures for partially throttled conditions were not considered in the current study. The number of fuel injections was set according to the experiments, while the fuel profiles were linearly defined to capture the right amount of fuel measured by the main fuel calibration. The pulse widths of the fuel injection for the pre-chamber were within linearity limit of the fuel injector, reported by Bosch. Thus, the amount of fuel injected was considered to be linear with the pulse width. The detailed fueling event of the pre-chamber was explained earlier under “Pre-Chamber Evaporation Model.” The intake/exhaust valve lifts were imposed directly, as well as the lift profile for the pre-chamber purge assembly and spark timing. The lift profiles of the intake, exhaust, and pre-chamber purge valves were measured using the MICRO-EPSILON optoNCDT displacement sensor, prior to the complete engine assembly.

The developed model consists of three sets of calibrating parameters specifying the engine combustion characteristics for both pre- and main combustion chambers; the pre-chamber fuel evaporation; and the heat transfer and flow characteristics between pre- and main combustion chambers. The calibrating parameters are listed in Table 3.3.

For each calibration point, the motoring pressure was closely matched to the experimental hot motoring pressure by optimizing the heat transfer and flow calibrating parameters. The main chamber wall temperatures of 170 ˚C, 150 ˚C, and 130 ˚C for the cylinder head, piston, and liner respectively with a heat transfer multiplier of 1 seemed to give a good prediction of the lean operating conditions tested in this study. The pre-chamber wall temperature was assumed to be the same as main chamber head temperature. The heat transfer multiplier of the pre-chamber was considered to be the same as that for the main chamber. The forward and backward discharge coefficients for the six-hole orifice connecting the pre- to the main chamber appeared to have a considerable effect on the correct prediction of the air flow for the pre-chamber valve assembly, as well as the right motoring pressure for the pre-chamber in reference to the main chamber. The pre-chamber pressure is slightly lower than the main chamber pressure during compression, and it tends to reverse its behavior as combustion starts in the pre-chamber or during the expansion stroke. The discharge coefficients were found to be 0.63 and 0.68 for forward and reverse flow, respectively. Forward flow in this simulation is in the direction of pre- to the main chamber.

Table 3.3 Calibrating parameters including the combustion-related parameters, the evaporation parameter, and the heat transfer & flow parameters.

	Combustion Calibrating Parameters
$\boldsymbol{\beta}$ *[-]*	Calibrating parameter to maintain the burn dependency of the pre- to the main chamber
$\boldsymbol{\alpha_{Pre}}$ *[-]*	Pre-chamber ignition delay calibrating parameter
$\boldsymbol{m_{pre}}$ *[-]*	Combustion mode parameter or Wiebe exponent for the pre-chamber
$\Delta\boldsymbol{\theta_{Pre}}$ *[CAD]*	Total burn duration for the pre-chamber
$\boldsymbol{\alpha_{Main}}$ *[-]*	Main chamber ignition delay calibrating parameter
$\boldsymbol{m_{Main}}$ *[-]*	Combustion mode parameter or Wiebe exponent for the main chamber
$\Delta\boldsymbol{\theta_{Main}}$ *[CAD]*	Total burn duration for the main chamber
$\boldsymbol{\eta_{eff-Pre}}$ *[%]*	Combustion efficiency of the pre-chamber
$\boldsymbol{\eta_{eff-Main}}$ *[%]*	Combustion efficiency of the main chamber
	Evaporation Calibrating Parameter
$\boldsymbol{k}$ *[-]*	Fraction of fuel to be evaporated at the time of injection into the pre-chamber
	Heat Transfer and Flow Calibrating Parameters
$\boldsymbol{Cd_{fwd}}$ *[-]*	Forward discharge coefficient for six-hole orifice connecting the pre- to the main chamber
$\boldsymbol{Cd_{bkw}}$ *[-]*	Backward discharge coefficient for six-hole orifice connecting the pre- to the main chamber
$\boldsymbol{T_{head-Main}}$ *[C]*	Main chamber head temperature
$\boldsymbol{T_{piston-Main}}$ *[C]*	Main chamber piston temperature
$\boldsymbol{T_{liner-Main}}$ *[C]*	Main chamber liner temperature
$\boldsymbol{T_{wall-Pre}}$ *[C]*	Pre-chamber wall temperature
$\boldsymbol{HTM_{Pre}}$ *[-]*	Pre-chamber heat transfer multiplier
$\boldsymbol{HTM_{Main}}$ *[-]*	Main chamber heat transfer multiplier

The single calibrating parameter for the pre-chamber evaporation modeling was previously optimized with the combustion-related calibrating parameters at 1500 rpm with a wide-open throttle. Different scenarios were studied, as the "k" factor ranged from 0.66 to 0.75. It appeared that a "k" factor of 0.7 is sufficiently precise for the optimization performed. The primary fuel injection event into the pre-chamber starts within 1 CAD of the end of the pre-chamber purge valve closing, for the cases studied. The upstream pressure and temperature of the purge valve were kept constant during the experiments. Although characteristics of the air trapped in the pre-chamber at the time of fuel injection may vary at different loads and speeds, the effect of associated variations on the “k” factor was considered negligible in regard to the precision expectancy of the 0D/1D model developed. A “k” factor of 0.7 was used through the entire simulation, which is equivalent to 70% of the fuel injected into the pre-chamber being evaporated at the time of injection.

The main chamber total burn duration, the pre-chamber combustion efficiency, and the main chamber combustion efficiency were pre-determined. The pre-chamber combustion mode parameter, Wiebe exponent, was also closely restricted to a narrow range of valid values. The pre-determination of some of the parameters is necessary when the cost function is co-dependent on a group of calibrating parameters. This co-dependency leads to the compensation by a number of parameters if any shortage of the cost function appears with respect to the rest of the calibrating parameters. The main chamber total burn duration is set to 60 CAD, while the pre- and main combustion efficiencies were assumed as 98%. The remaining calibrating parameters were optimized using a nondominated sorting genetic algorithm (NSGA).

The nondominated sorting genetic algorithm III (NSGA-III) [108] used in this simulation is the successor to NSGA-II and is optimized for multi-objective Pareto optimization. NSGA-III is a powerful global optimizer for a thorough search of the entire design space. There are two main inputs to be defined prior to a NSGA optimization: the population size and the number of generations. There are recommendations available based on the number of parameters to be calibrated. A population size of 26 was chosen for the current study, having 6 calibrating parameters to be optimized at the same time. The number of generations was observed to be 20±5 to reach a reasonable convergence.

A cost (fitness) function was defined to include the weighted summation of squared numerical-to-experimental errors for both pre- and main combustion chambers during the pre-chamber combustion before top dead center of fire (TDCF); the weighted squared numerical-to-experimental error for the amplitude and phasing of the main chamber maximum pressure; and the weighted squared numerical-to-experimental errors for five selected points from the main chamber pressure trace. The weighting factors were studied to improve the cost function toward capturing the right pressure traces for both pre- and main combustion chambers. Equation 3.16 displays the cost function used in this study.

$$\begin{aligned} Cost\ Function = &\sum_{\substack{PreCh\\Combustion}} \left\{ w_1 \left(p_{Num,Pre} - p_{Exp,Pre}\right)^2 + w_2 \left(p_{Num,Main} - p_{Exp,Main}\right)^2 \right\} + \\ &w_3 \left(p_{Num} - p_{Exp}\right)^2_{Max\ Amplitude,Main} + \\ &w_4 \left(\theta_{Num} - \theta_{Exp}\right)^2_{Max\ Amplitude,Main} + \\ &\sum_{i=1}^{5} w_{i+4} \left(p_{Num} - p_{Exp}\right)^2_{Point\ i,Main} \end{aligned} \tag{3.16}$$

where, w_1 to w_9 are the weighing factors for the terms defined in the cost function, p is the in-cylinder pressure, and θ is the instantaneous crank angle degree. Subscripts "Pre", "$Main$", "Num", and "Exp" denote the pre-chamber, main chamber, numerical, and experimental; respectively.

3.6 Results and Discussion

3.6.1 Energy Input for a Pre-Chamber Air Valve

The dampener system, explained under "Experimental Setup" and shown in Fig. 3.7, successfully dampened the flow upstream of the air valve for a reliable flow measurement. Figure 3.14 shows the flow measured by the low-range laminar flow element (LFE) at 1500 rpm with a wide-open throttle (WOT). The volume flow fluctuation is negligible considering that the flow upstream of the air valve is highly pulsatile. As seen in Fig. 3.14, the average flow slightly decreases over time. The downward trend, although small, may be due to the wall temperature rise of the pre-chamber.

A comprehensive study is needed to find the elements involved and their corresponding effects. The average volume flow rate was observed to be 0.15 SCFM at 1500 rpm. At 2000 rpm, the average flow was measured as 0.16 SCFM which is slightly higher than the flow at 1500 rpm. The pre-chamber air valve was opened at -150 CADaTDCF and closed at -120 CADaTDCF with 1 bar gauge upstream pressure.

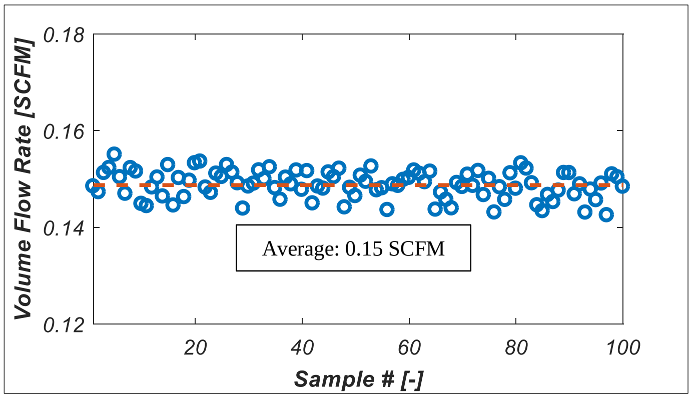

Figure 3.14 Volume flow rate measured by the low range LFE at 1500 rpm with a WOT.

The LFE reading was verified by direct measurement using a displaced bubble technique as well as by GT-POWER Model, with the results found to be in good agreement. The purge valve flow coefficients were adjusted accordingly along with the discharge coefficients of the six-hole orifice, connecting the pre- to the main chamber, to replicate the experimental data. Numerical results for the pre-chamber air flow precisely follow the experiments for both 1500 rpm and 2000 rpm. The relative error was below 2% of the experimental data.

Based on the results obtained in the Prototype II DM-TJI engine and the Womack fluid power design sheet [109], at 1 bar gauge upstream pressure less than 6.5 watts of power are required to deliver 0.15 SCFM or 0.16 SCFM air flow; corresponding to 1500 rpm and 2000 rpm, respectively. Thus, for a four-cylinder engine running at 1500 rpm or 2000 rpm, 25 watts of power would be sufficient. At higher speeds and loads or under highly dilute conditions, the required airflow will be greater. However, by delivering the pre-chamber air during the appropriate time of compression, work will be recovered from the pre-chamber purge air during the expansion stroke of the piston.

In addition to pumping air, the work required to activate the valve system for a four-cylinder engine is about 75 watts at 2000 RPM. This value is based on power requirements to drive an engine camshaft given to MSU from a Tier 1 OEM supplier. The DM-TJI system has a small poppet valve with a small actuation lift requirement. The assumption of 75 watts is very conservative. It is half of the power required for a conventional camshaft. Mechanical cams are extremely efficient valve actuators, as the compressed springs put work back into the system during decompression.

It appears that this function is ideally suited to electrification, as the trend in the next decade is that nearly all vehicles will be at least partially electrified. If a pre-chamber reservoir is charged at a condition where excess electrical energy is available, either because a battery is fully charged or can only take charging at a certain rate, that energy to drive the electric pump is actually free. Results to date show that power consumption to deliver pre-chamber air will not be a factor limiting implementation of the technology.

3.6.2 Combustion Stability

An extensive set of experiments was conducted on the Prototype II DM-TJI engine. The experiments were run at 1500 rpm and 2000 rpm with both wide-open throttle (WOT) and the throttle partially opened. The normalized air/fuel ratio (lambda) was kept at 1.9±0.1 for all the experiments in this study. The spark timing and the fuel strategy in the pre-chamber were varied to obtain the combustion stability at each operating condition. The fueling event of the pre-chamber happened at -120 CADaTDCF with one pulse of 1.3 ms or 1.5 ms. Table 3.4 summarizes the spark sweeps and the fuel strategies examined in this study. The pre- and main chamber fuel injectors were run at 100 bar with 3 pulses of fuel into the main chamber starting at -360 CADaTDCF with 1.5 ms in between. The pre-chamber air valve was opened at -150 CADaTDCF and closed at -120 CADaTDCF with 1 bar gauge upstream pressure.

Table 3.4 Spark sweeps and fuel strategies associated with the points examined in this study.

Speed [rpm]	Throttle Position [-]	Spark Sweep [CADaTDCF]	Pre-Chamber Fuel Strategy [ms]
2000	Wide Open	-29, -28, -27, -26	1.3, 1.5
2000	Partial	-36, -34	1.3, 1.5
1500	Wide Open	-29, -28, -27, -26, -25	1.3, 1.5
1500	Partial	-34, -33, -32, -31	1.3, 1.5

Results demonstrated a stable combustion for all four operating conditions over the spark sweep and the two fuel strategies inside the pre-chamber. Combustion stability with an IMEP COV below 2.5% is proven to be attained at highly lean conditions, lambda ~2, for the throttle conditions both wide and partially opened. The observed CA50s, crank angle degree at which 50% of the fuel is burned, ranged from 3 to 6 CADaTDCF.

3.6.3 Brake Efficiency Calculation

A preliminary efficiency calculation was conducted on the results obtained from experiments under highly lean conditions, lambda ~2. A friction loss of 6% with no pumping loss at WOT and a 3% pumping loss at partially throttled conditions were considered in these calculations. An estimation of the work input for the air valve assembly, as explained under "Energy Input for a Pre-Chamber Air Valve," was included in the brake efficiency calculations. The lower heating value of the fuel used in this study was examined and reported by Galbraith Laboratories Inc. as 43.2 MJ/kg.

The case at 2000 rpm with a WOT maintained the highest gross indicated efficiency at 41.2%, which resulted in 38.6% brake thermal efficiency. The second-highest gross indicated efficiency belonged to the case at 1500 rpm with a WOT at 40.3%. The brake thermal efficiency was then calculated as 37.6%. The operating conditions with partially opened throttle at 2000 rpm and 1500 rpm resulted in 39.8% and 40.1% of gross indicated efficiencies, leading to 36.1% and 36.2% in brake thermal efficiencies, respectively.

Table 3.5 presents the efficiency calculations. The thermal efficiencies obtained for the Prototype II DM-TJI engine were compared to the results reported by Ortiz-Soto and colleagues for an engine run under an advanced multi-mode combustion in Fig. 3.15. The multi-mode combustion studied in their work involved spark ignition (SI), homogeneous charge compression ignition (HCCI), and spark-assisted compression ignition (SACI) operating strategies [107]. The SI-HCCI-SACI engine used in their study has the same bore and stroke (86 mm/94.3 mm) as the DM-TJI engine examined in the current work, with slightly higher compression ratio (12.42:1) than the Prototype II DM-TJI engine. Figure 3.15 clearly demonstrates the potential of a DM-TJI system for higher thermal efficiencies at low to mid-load operating conditions, as the results obtained for the DM-TJI system lie close to those for HCCI-SACI combustion. The DM-TJI system benefits from high thermal efficiencies close to HCCI-SACI combustion technologies, while it does not involve the difficulties arising from those types of combustion. The latter difficulties include the complex control mechanism and fuel intolerance.

Table 3.5 Preliminary brake efficiency calculations for the Prototype II DM-TJI engine (naturally aspirated, CR=12:1, bore=86 mm, stroke=95 mm). A friction loss of 6% with no pumping loss at WOT and a 3% pumping loss at partially throttled conditions were considered in these calculations. The work input associated to the pre-chamber air valve was included proportional to the volume flow rate of the pre-chamber air valve.

Speed [rpm]	Throttle Position [-]	Gross IMEP [bar]	BMEP, WO Pre Air [bar]	BMEP, W Pre Air [bar]	Gross Indicated Efficiency [%]	Brake Efficiency, WO Pre Air [%]	Brake Efficiency, W Pre Air [%]
2000	WOT	6.60	6.20	6.18	41.2	38.8	38.6
2000	Partial	4.47	4.08	4.05	39.8	36.3	36.1
1500	WOT	6.04	5.68	5.64	40.3	37.9	37.6
1500	Partial	4.54	4.14	4.10	40.1	36.5	36.2

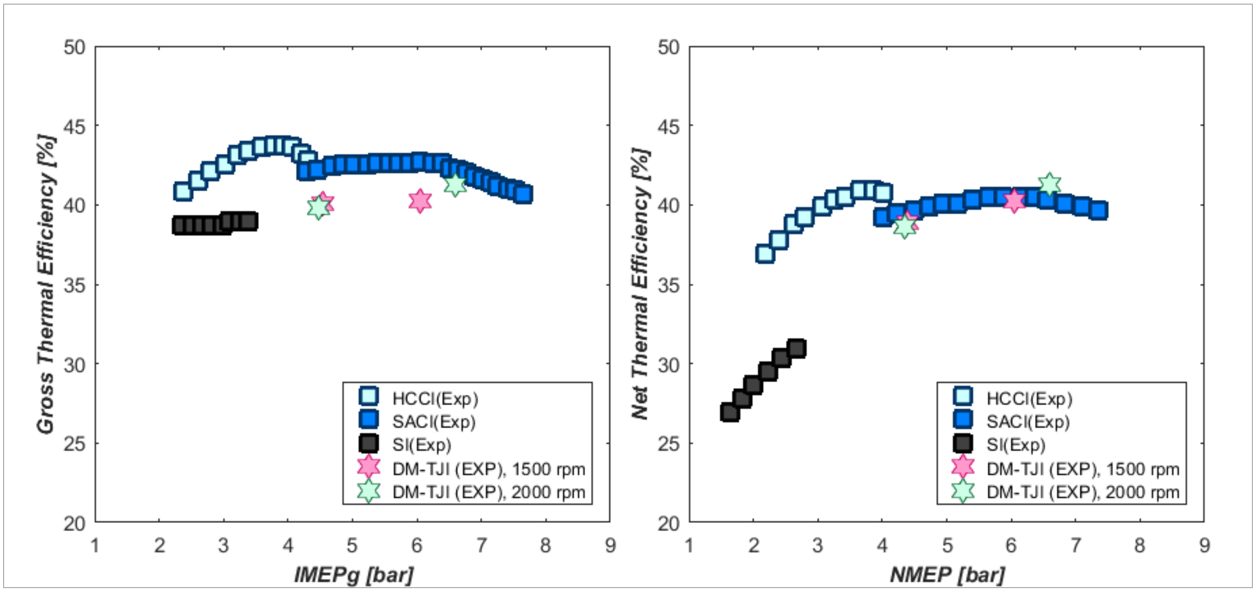

Figure 3.15 Thermal efficiencies obtained for the Prototype II DM-TJI engine compared to an engine run under SI-HCCI-SACI combustion strategies. The main figure is a duplication of the results presented by Ortiz-Soto and colleagues in "Thermodynamic efficiency assessment of gasoline spark ignition and compression ignition operating strategies using a new multi-mode combustion model for engine system simulations" [107]. The data from the Prototype II DM-TJI were added based on preliminary efficiency calculations under lean operating conditions, lambda ~2.

3.6.4 Model Predictions of Experimental Trends

The engine system model developed was calibrated based on experimental data at four operating conditions shown in Table 3.5. The calibration processes were explained previously under "Calibration of Engine System Model," and the results are presented in Table 3.6. In general, it appears that the numerical simulations were able to capture the experimental trends. The validity of the model in prediction of experiments was observed based on the standard metric of the coefficient of determination, R^2, shown in Fig. 3.16; and comparison plots for the in-cylinder pressures presented in Figs. 3.17, 3.18, 3.19, and 3.20. The dashed lines in Fig. 3.16 indicate 5% error lines. Numerical predictions for three metrics of main chamber combustion (gross IMEP, main chamber peak pressure, and main chamber phasing for the peak pressure) were within 5% of experimental data with one exception happening at 6% (peak pressure phasing of the main chamber for partially throttled case at 1500 rpm). Solid blue lines in the upper images of Figs. 3.17-3.20

represent the experimental trend, while numerical predictions are depicted in dashed red lines. The lower images in the same figures show the numerical-to-experimental errors at each crank angle. The absolute root mean square (RMS) errors of in-cylinder pressures for both pre- and main combustion chambers were below 0.35.

Table 3.6 Optimization results for the calibrating parameters of the engine system model.

	2000/WOT	2000/PT	1500/WOT	1500/PT
Combustion Calibrating Parameters				
β [-]	0.88	1.08	1.05	0.62
$PreCh\ Ignition\ Delay\ Index$ [-]	0.19	0.24	0.18	0.20
m_{pre} [-]	0.51	0.50	0.56	0.50
$\Delta\theta_{Pre}$ [CAD]	47.23	45.03	50.70	45.56
$MainCh\ Ignition\ Delay\ Index$ [-]	0.17	0.18	0.10	0.11
m_{Main} [-]	2.73	2.50	2.95	2.35
$\Delta\theta_{Main}$ [CAD]	60.00	60.00	60.00	60.00
$\eta_{eff-Pre}$ [%]	98.00	98.00	98.00	98.00
$\eta_{eff-Main}$ [%]	98.00	98.00	98.00	98.00
Evaporation Calibrating Parameter				
k [-]	0.7	0.7	0.7	0.7
Heat Transfer and Flow Calibrating Parameters				
Cd_{fwd} [-]	0.63	0.63	0.63	0.63
Cd_{bkw} [-]	0.68	0.68	0.68	0.68
$T_{head-Main}$ [C]	170	170	170	170
$T_{piston-Main}$ [C]	150	150	150	150
$T_{liner-Main}$ [C]	130	130	130	130
$T_{wall-Pre}$ [C]	170	170	170	170
HTM_{Pre} [-]	1	1	1	1
HTM_{Main} [-]	1	1	1	1

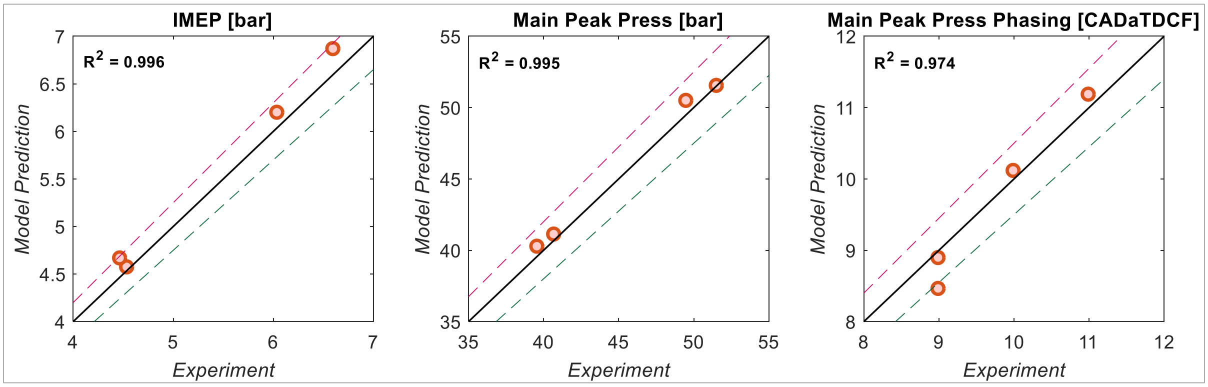

Figure 3.16 Correlation plots for gross IMEP, main chamber peak pressure, and peak pressure phasing of the main chamber. The high R^2 values indicate the high level of correlation between numerical predictions and experiments.

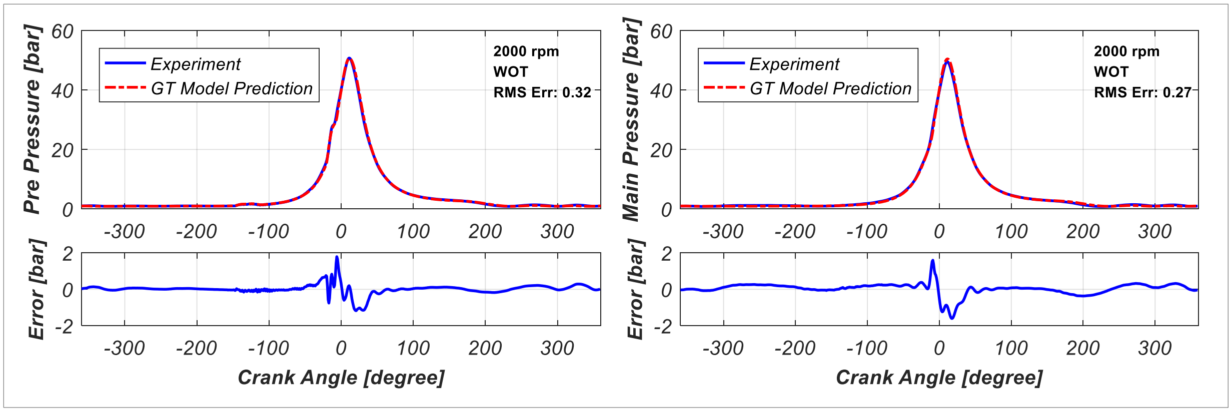

Figure 3.17 Model prediction vs. experiments for in-cylinder pressures of pre- and main combustion chambers at 2000 rpm with a WOT.

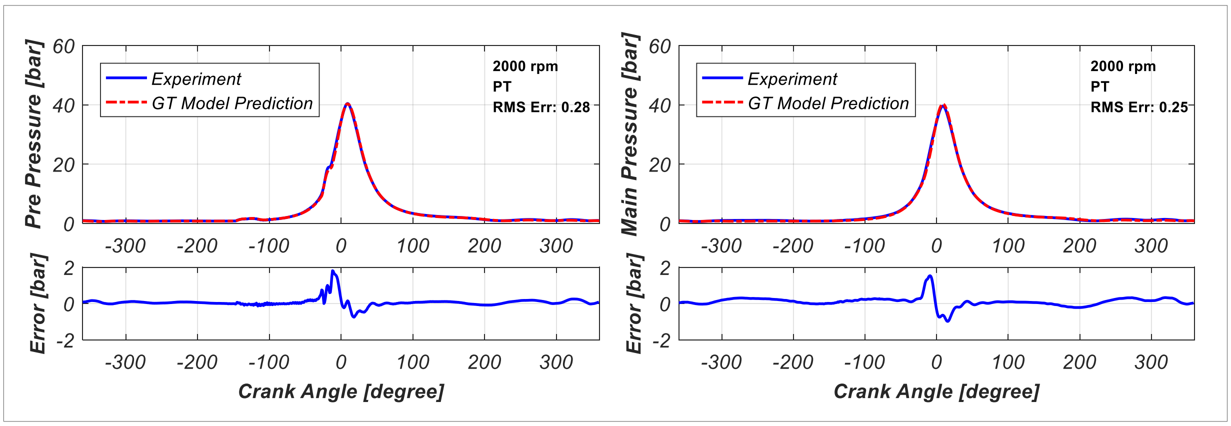

Figure 3.18 Model prediction vs. experiments for in-cylinder pressures of pre- and main combustion chambers at 2000 rpm with a throttle partially opened.

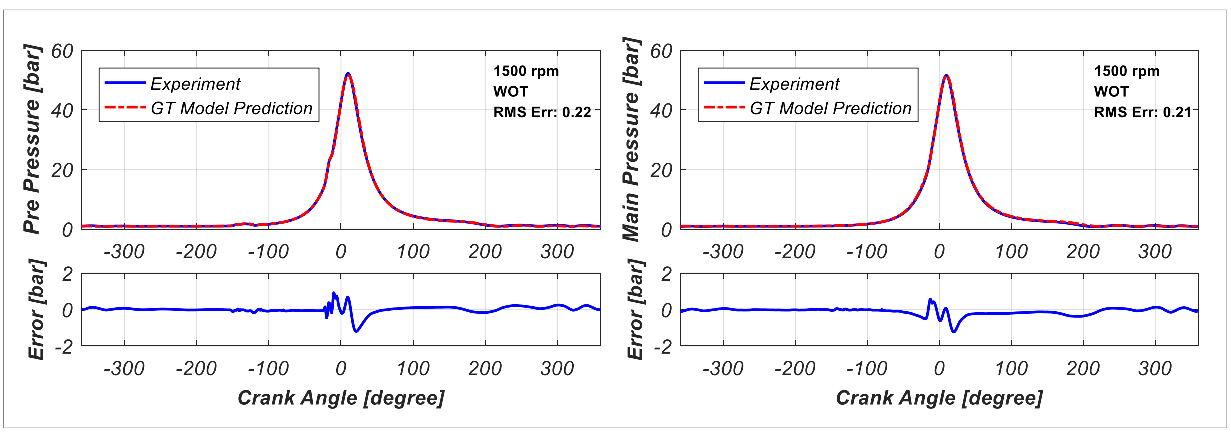

Figure 3.19 Model prediction vs. experiments for in-cylinder pressures of pre- and main combustion chambers at 1500 rpm with a WOT.

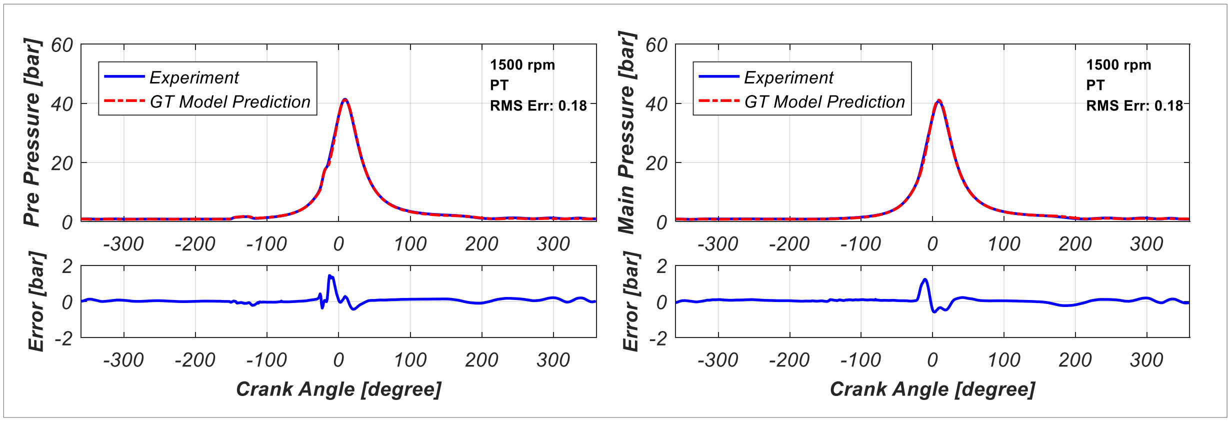

Figure 3.20 Model prediction vs. experiments for in-cylinder pressures of pre- and main combustion chambers at 1500 rpm with a throttle partially opened.

As mentioned earlier, none of the studies to date on the DM-TJI engine predicted the losses of such a system. Table 3.7 presents the heat transfer and exhaust losses as the percentage of total fuel energy in addition to the pre-chamber lambda at the time of spark timing, and the main chamber combustion phasing and 10-90% burn duration. Model prediction for ignition delays of pre- and main combustion chambers are also shown in the same table.

Table 3.7 Model prediction of in-cylinder characteristics.

	2000/WOT	2000/PT	1500/WOT	1500/PT
Pre-Chamber Lambda @Spark Timing	1.2	0.7	1.0	0.8
Main Chamber CA50* [CADaTDCF]	6.5	2.9	4.3	3.1
Burn 10-90** [CAD]	26.1	26.4	25.3	26.7
Pre-Chamber Ignition Delay [CAD]	4.86	8.56	4.81	6.36
Main Chamber Ignition Delay [CAD]	4.39	6.44	2.71	3.48
Heat Transfer, % of Total Fuel Energy	22.3	25.5	26.0	28.4
Exhaust, % of Total Fuel Energy	35.3	34.9	32.8	32.6
Indicated Efficiency, % of Total Fuel Energy	41.2	39.6	41.2	39.0

* The crank angle degree at which 50% of the fuel is burned.
** The duration in crank angle degree from 10% of the fuel burned to the 90%.

The results demonstrate a range of lambda distribution for the pre-chamber at the time of spark event, from slightly rich (lambda <1) to slightly lean (lambda > 1). The results may be in part influenced by pre-chamber evaporation modeling which considers a fixed percentage of fuel evaporation at the time of fuel injection into the pre-chamber. However, the range of lambda distributions obtained is within the range described for this type of combustion technology [47,52,53], with previous studies being more inclined toward the rich side of air/fuel ratios.

The CA50 values calculated for the main combustion chamber ranged from 3 to 6 CADaTDCF. The 10-90% burn duration ranged from 25 to 27 CAD. Ortiz-Soto and colleagues reported the 10-90% burn duration ranging from 25 to 28 CAD for their idealized-air and idealized-EGR simulations [107], while the combustion efficiency was considered as ~98%. Such idealized simulations were corresponding to 40-45% gross thermal efficiencies. The 10-90% burn durations for HCCI-SACI combustion have been also reported by the same group in the range of 5 CAD to 20 CAD, with combustion efficiency ranging from 85% to 98%. As the thermal efficiencies for the DM-TJI system were close to those in HCCI-SACI combustion reported by Ortiz-Soto et al., one may expect the same in-cylinder behaviors as well. In this study, the combustion efficiency of the DM-TJI engine was assumed as 98% for both pre- and main combustion chambers. However, a lower combustion efficiency will lead to a faster burn rate calculation for the DM-TJI system, as both HCCI-SACI and DM-TJI engines benefit from the same high thermal efficiencies. Further studies should be conducted to shed light on this matter.

The simple approach employed to capture ignition delays for both pre- and main combustion chambers seems to predict a reasonable trend. As described earlier under "Numerical Approach and Model Development," two calibrating parameters (α_{Pre} and α_{Main}) were optimized at each of the four operating conditions studied here to define ignition delays of the pre- and main chambers. These two parameters were normalized with respect to spark timing. The results obtained demonstrated an increase in ignition delays as the engine speed increases, and a decrease in ignition delays as the load increases. The trend observed is in agreement with the results reported by Assanis and colleagues [36] for the ignition delays of a direct-injection diesel engine. Tolou and colleagues observed the same trend for ignition delays of a gasoline direct injection (GDI) engine

[110]. However, the former study reported an increase in ignition delays, as the load further increases and exceeds 120 N-m of brake torque at high-boost conditions.

Model prediction for in-cylinder losses toward the heat transfer and exhaust follows a logical trend. Heat transfer decreases, as engine speed increases. Energy loss through exhaust, on the other hand, increases, as engine speed goes up. The rise in exhaust energy loss at higher speeds seems reasonable, as not all the energy saved by less heat transfer at higher speeds will be recovered as indicated efficiencies. On average, 26% of total fuel energy is lost through heat transfer, followed by 34% through exhaust. The averaged loss mentioned above leaves a 40% indicated thermal efficiency at low to mid-load operating conditions for the DM-TJI system examined in the current work.

3.6.5 Predictive, Generalized Model for a DM-TJI Engine

The optimization results for model calibrating parameters were further studied to propose a predictive, generalized model for a DM-TJI engine. Such a model is essential to project the behavior of an engine equipped with the DM-TJI combustion technology over the entire engine fuel map. Table 3.6 presented the optimization results for each of the calibrating parameters in this study. Considering the low range of variation for each of these parameters, it seems that an average value should well predict the general behavior. The combustion-related calibrating parameters, optimized by NSGA and described in Table 3.6, were averaged over the four cases examined in this study. The parameters recommended for a predictive, generalized model are listed in Table 3.8.

The author proposes that the spark timing should be optimized at each operating condition to achieve the highest thermal efficiency, while the 10-90% burn duration is kept below 27 CAD. In this study, the highest 10-90% burn duration was observed to be 27 CAD. Lavoie and colleagues reported a 10-90% burn duration of 25 CAD as a choice to obtain best efficiencies possible over the range of conditions studied [111]. The 25 CAD of 10-90% burn duration was described by the same group as the mid-way between HCCI and dilute SI combustion. The study by Lavoie et al. also determined a minimum 10-90% burn duration of ~20 CAD as the low limit to achieve high efficiencies in normal engines with heat transfer. The gain in thermal efficiency by further reduction of 10-90% burn duration below 20 CAD was perceived to be negligible.

Table 3.8 Calibrating parameters for a predictive, generalized model of a DM-TJI system.

Combustion Calibrating Parameters	
β [-]	0.9
$PreCh\ Ignition\ Delay\ Index$ [-]	0.20
m_{pre} [-]	0.5
$\Delta\theta_{Pre}$ [CAD]	47
$MainCh\ Ignition\ Delay\ Index$ [-]	0.14
m_{Main} [-]	2.6
$\Delta\theta_{Main}$ [CAD]	60.00
$\eta_{eff-Pre}$ [%]	98.00
$\eta_{eff-Main}$ [%]	98.00
Evaporation Calibrating Parameter	
k [-]	0.7
Heat Transfer and Flow Calibrating Parameters	
Cd_{fwd} [-]	0.63
Cd_{bkw} [-]	0.68
$T_{head-Main}$ [C]	170
$T_{piston-Main}$ [C]	150
$T_{liner-Main}$ [C]	130
$T_{wall-Pre}$ [C]	170
HTM_{Pre} [-]	1
HTM_{Main} [-]	1

As the pre-chamber combustion is the source of ignition inside the main chamber, the pre-chamber fuel, and the pre-chamber air valve timing and upstream pressure should also be optimized at each operating condition to maintain a lambda of 0.9±5% at the time of spark event. The 0.9 lambda is the 4-case- averaged value of the model predictions at the time of spark timing. The 5% bandwidth was defined to account for the uncertainties regarding the lambda calculation. Maintaining a proper lambda at the time of spark event will be more crucial if the model is used to project the behavior of the DM-TJI engine under highly dilute conditions with excess EGR. Based on the Womack fluid power design sheet [109], the work required to deliver air to the pre-chamber of a DM-TJI system is proportional to both pressure and volume flow rate. These differ from one operating condition to another. Furthermore, the primary fueling event inside the pre-chamber should always happen within a small number of crank angle degrees from the pre-chamber valve closing to maintain the stoichiometry inside the pre-chamber.

The in-cylinder maximum pressures can be limited by adding a constraint to the optimization to reflect the design specifications. Wall temperatures of pre- and main combustion chambers may also need to be modified based on an engineering judgment at higher loads.

The possibility of knocking behavior, which is more likely to happen at low speeds and high loads, was not examined in the current study. This issue is not considered as an error to the current modeling approach, but as a limitation of the current analysis. Investigating the knocking behavior was out of the scope of the current project and its experimental platform. Thus, if it were possible to address the knocking behavior by any means including but not limited to in-cylinder charge preparation and/or combustion chamber design, the current model should be capable of projecting the DM-TJI engine behavior over the entire engine fuel map.

3.6.6 DM-TJI Engine Fuel Map under Highly Dilute Conditions

The approach described above was utilized to generate a complete engine fuel map which covers the power requirements of the Ford F-150 2.7-Liter EcoBoost®. According to the National Public Radio (NPR), a Ford F-150 pickup truck is sold about every 30 seconds in the U.S. [112]. The Ford F-150 is not only America's best-selling pickup truck but also America's best-selling vehicle in total [113]. The Ford F-Series has gained an incredible reputation in both fuel economy and vehicle performance.

The Ford 2.7-Liter EcoBoost® is a turbocharged six-cylinder engine which includes the Ford port-fuel and direct-injection (PFDI) system with two injectors per cylinder; dual overhead cam design with variable intake/exhaust cam timing; and twin intercooled turbochargers for on-demand power [114]. The maximum torque curve of the engine was satisfied via a four-cylinder boosted configuration of the DM-TJI engine with higher limits for brake mean effective pressures (BMEP). A maximum of 2 bar gauge boost pressure and 40% exhaust gas recirculation (EGR) were employed. The in-cylinder pressures for both pre- and main combustion chambers were bound to a maximum of 150 bar at high-load operating conditions.

Figure 3.21 presents a conceptual diagram for the modeling framework used in this study in order to generate a full engine map, equivalent to power requirements of the Ford F-150 2.7-Liter vehicle. The black solid line in this figure shows the maximum torque curve for the 2.7-Liter EcoBoost® engine. The full fuel map of the 2.7-Liter EcoBoost® was produced by the U.S. EPA National Vehicle and Fuel Emission Laboratory (NVFEL) located in Ann Arbor, Michigan [115,116]. The dash-dot line in grey marks the naturally aspirated line at 40% external EGR. The core data including the ones representing the naturally aspirated line up to the maximum torque curve were generated by the GT-POWER model simulations performed in the current study. As one can see in Fig. 3.21, the external EGR was first kept constant, while the boost pressure was increased to achieve higher loads at different speeds. After that, the boost pressure was kept constant at 2 bar gauge (maximum boost pressure used in the current simulations) and the amount of external EGR was reduced to reach the maximum torque of 508.4 N-m at 3000 rpm.

At each operating condition, the main chamber fuel was first optimized to maintain the stoichiometry for the rest of the charge trapped in the cylinder. Afterward, a GA optimization was run for each of the operating conditions to optimize the spark timing, the pre-chamber fuel, and the pre-chamber valve upstream pressure and timing. The goal of the optimization was defined to maximize the indicated gross efficiency. The maximum in-cylinder pressures of 150 bar and the pre-chamber lambda of 0.9±5% at the time of spark event were added as constraints to the optimizations. The amount of EGR trapped in the pre-chamber at start of combustion (SOC) was also constrained to a maximum of 30% to ensure a successful combustion in the pre-chamber. The optimizations were performed with a population size of 16, while the number of generations was set to 5.

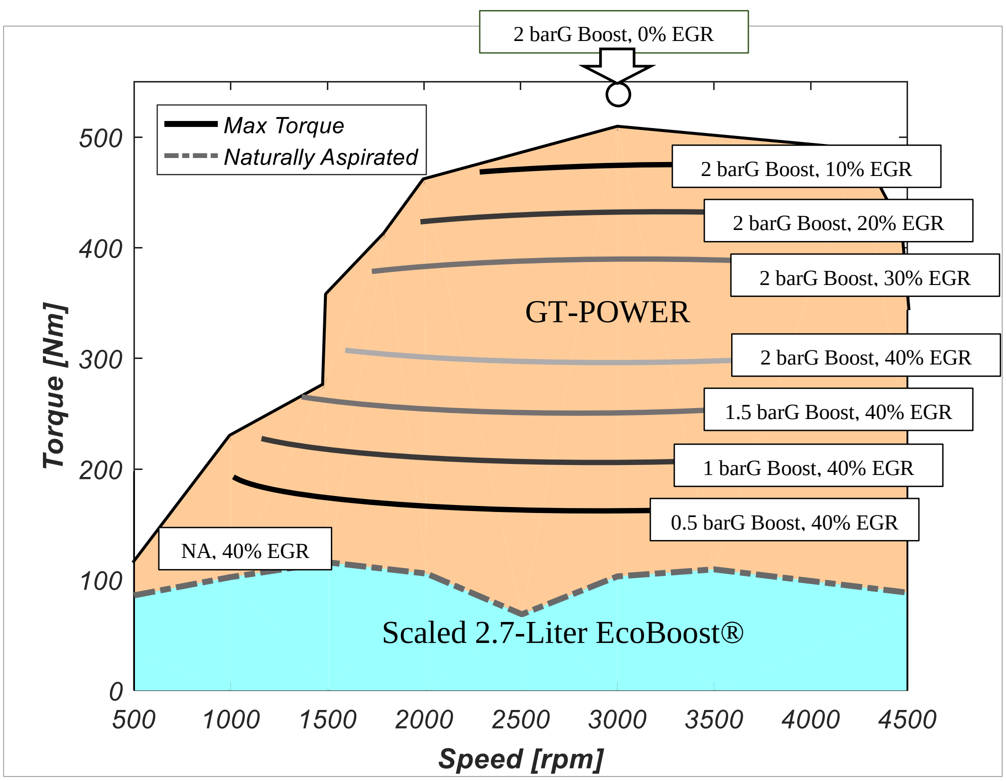

Figure 3.21 Modeling framework used in order to generate a full engine map, equivalent to the power requirements of the Ford F-150 2.7-Liter EcoBoost®, for the DM-TJI engine under highly dilute conditions.

The core data below the naturally aspirated line were covered based on experimental data from the 2.7-Liter EcoBoost® at a number of brake mean effective pressures (BMEP) in that region. The fuel consumptions of the 2.7-Liter EcoBoost® at low loads were scaled to be used toward the fuel map generation of the DM-TJI engine. The data scaling took place using Equation 3.17 with taking into account the change in engine displacement from the 2.7-Liter EcoBoost® to the 2.2-Liter DM-TJI engine. The 2.7-Liter EcoBoost® includes 6 cylinders of 0.45-Liter, while the DM-TJI engine was defined in a four-cylinder configuration of 0.55-Liter each. The brake specific fuel consumptions (BSFC) at each particular BMEP were kept the same. The power value, however, reflected the change in engine displacement at the same BMEP from one engine to the other.

$$\dot{m}_{fuel}\left(\frac{g}{hr}\right) = BSFC\left(\frac{g}{kW - hr}\right) \times P(kW) \tag{3.17}$$

Figure 3.22 represents the thermal efficiency map for the DM-TJI engine in a four-cylinder configuration. Accordingly, the brake specific fuel consumption (BSFC) map in g/kW-hr is shown in Fig. 3.23. The core data obtained from the GT-POWER simulations and the 2.7-Liter EcoBoost® engine are displayed in black dots through the whole map for both the thermal efficiency and BSFC. A MATLAB surface generator algorithm called "gridfit" was employed to build the complete map of the DM-TJI engine out of obtained scattered data [117]. The smoothing parameter of the algorithm was altered to slightly smoothen the data and achieve a better representation. The details of BSFC calculations for the core data generated by the GT-POWER model simulations can be found in Appendix A, Tables A.1 and A.2.

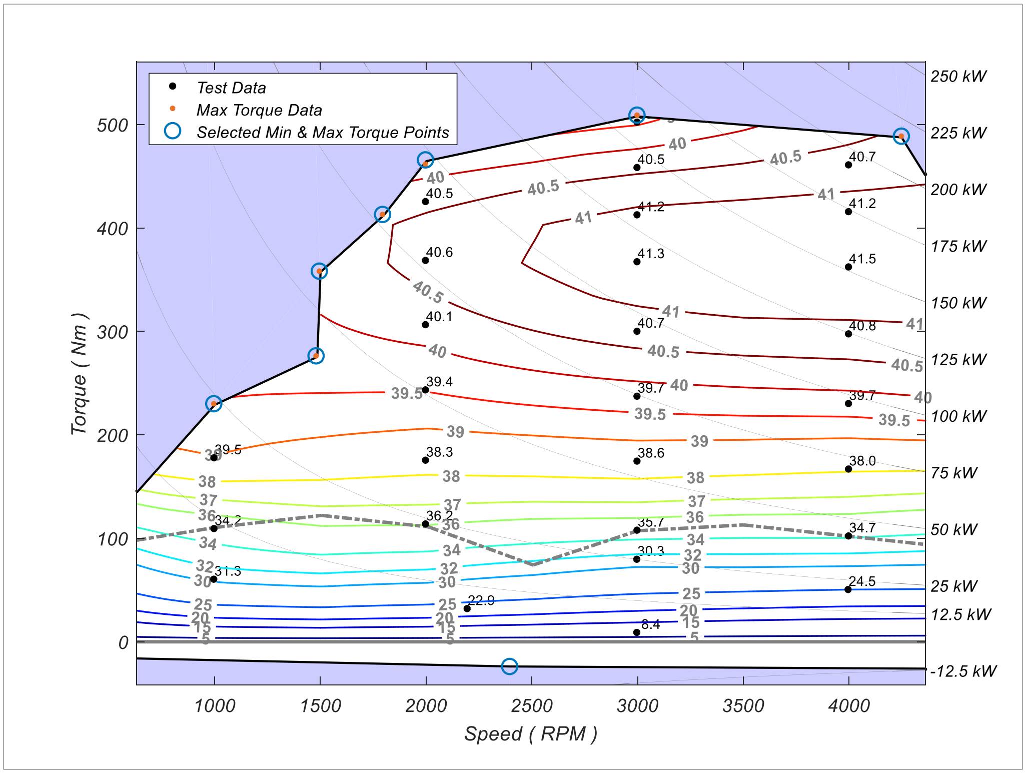

Figure 3.22 Brake thermal efficiency map of the DM-TJI engine in a four-cylinder boosted configuration under highly dilute conditions up to 40% external EGR.

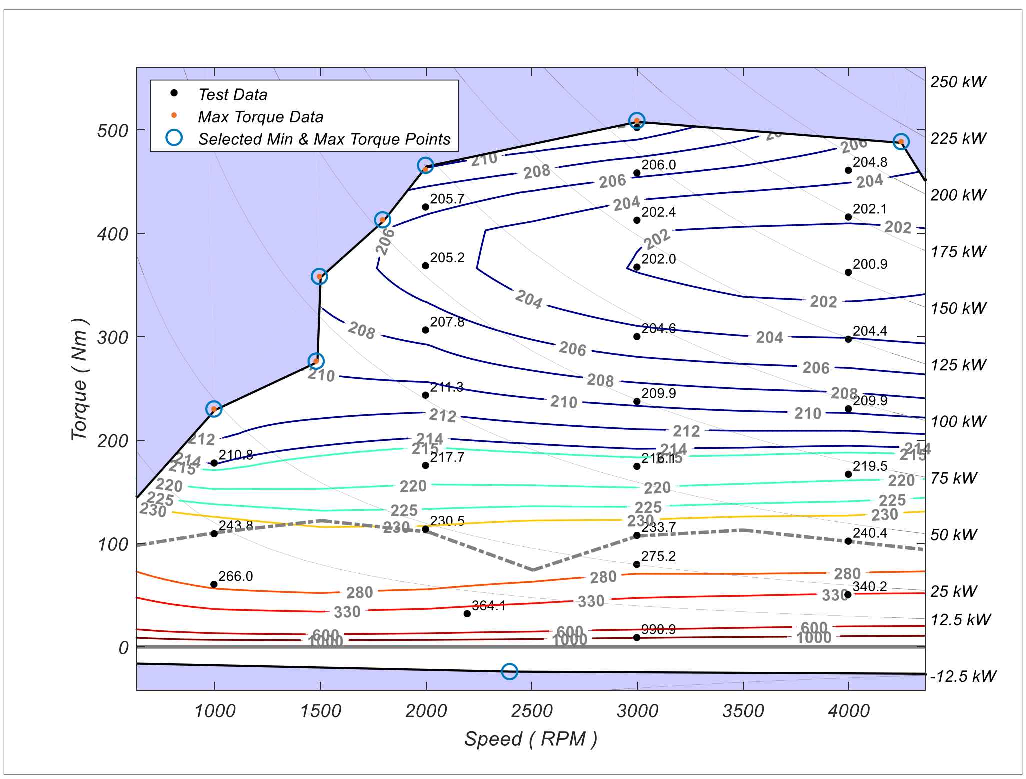

Figure 3.23 Brake specific fuel consumption (BSFC in g/kW/hr) map of the DM-TJI engine in a four-cylinder boosted configuration under highly dilute conditions up to 40% external EGR.

The friction term in BMEP calculations of the core data generated by the GT-POWER model was described by the Chen-Flynn equation [118], Equation 3.18.

$$FMEP = 0.3\ [bar] + 0.004\ [-]\ P_{Cyl,max} + 0.08\ [\frac{bar}{m/s}]\ U_p \tag{3.18}$$

where, FMEP is the friction mean effective pressure in bar; $P_{Cyl,max}$ is the maximum cylinder pressure in bar; and U_p is the mean piston speed in m/s. Equation 3.18 includes the GT-POWER recommended coefficients for such a model. The units for each of the coefficients in Equation 3.18 are shown in the brackets above.

Additionally, the warmed-up closed-throttle (CT) BMEP curve for the 2.7-Liter EcoBoost® engine was provided to the MSU Energy and Automotive Research Lab (EARL) by the U.S. EPA NVFEL. Figure 3.24 displays the segmented closed-throttle curve at four different speeds (1000 rpm to 4000 rpm with a 1000 rpm increment) compared to the FMEP results obtained by the Chen-Flynn model for all the loads studied at the same speeds. The differences observed between the CT values and the Chen-Flynn simulations include the slight pumping work at closed throttle plus the energy loss through heat transfer. The maximum amount of difference was observed to be 33% at the lowest BMEP and the speed of 2000 rpm. The minimum difference of 6% happened at the high load and 3000 rpm. In general, the discrepancy between two curves decreases as the load increases; and the Chen-Flynn model takes into account the term for maximum in-cylinder pressures. The magnitude of highest relative difference between the CT values and the Chen-Flynn calculations also decreases, as speed increases and consequently the engine heat transfer reduces. Moreover, the discrepancy between the CT values and the Chen-Flynn model calculations becomes almost constant, as the BMEP passes a particular threshold at higher loads. Recall that the in-cylinder pressures for both pre- and main combustion chambers were bound to a maximum of 150 bar at high-load operating conditions. The details of friction calculations for the core data obtained by the GT-POWER model can be found in Appendix A, Table A.4. Friction calculations performed by the Chen-Flynn equation were used toward BSFCs, as there was no other data available on the friction curve of the 2.7-Liter EcoBoost® engine.

Figure 3.25 displays indicated gross efficiencies obtained for the current simulations with respect to BMEP at different speeds. In general, indicated efficiency increases, as engine speed goes up. Additionally, higher BMEPs corresponding to higher boost pressures lead to higher gross indicated efficiencies. The indicated efficiency decreases with further increase in BMEP above 23 bar. To obtain BMEPs above 23 bar, the in-cylinder charge dilution was reduced, and the spark timing was retarded to not exceed the 150 bar threshold of in-cylinder pressures.

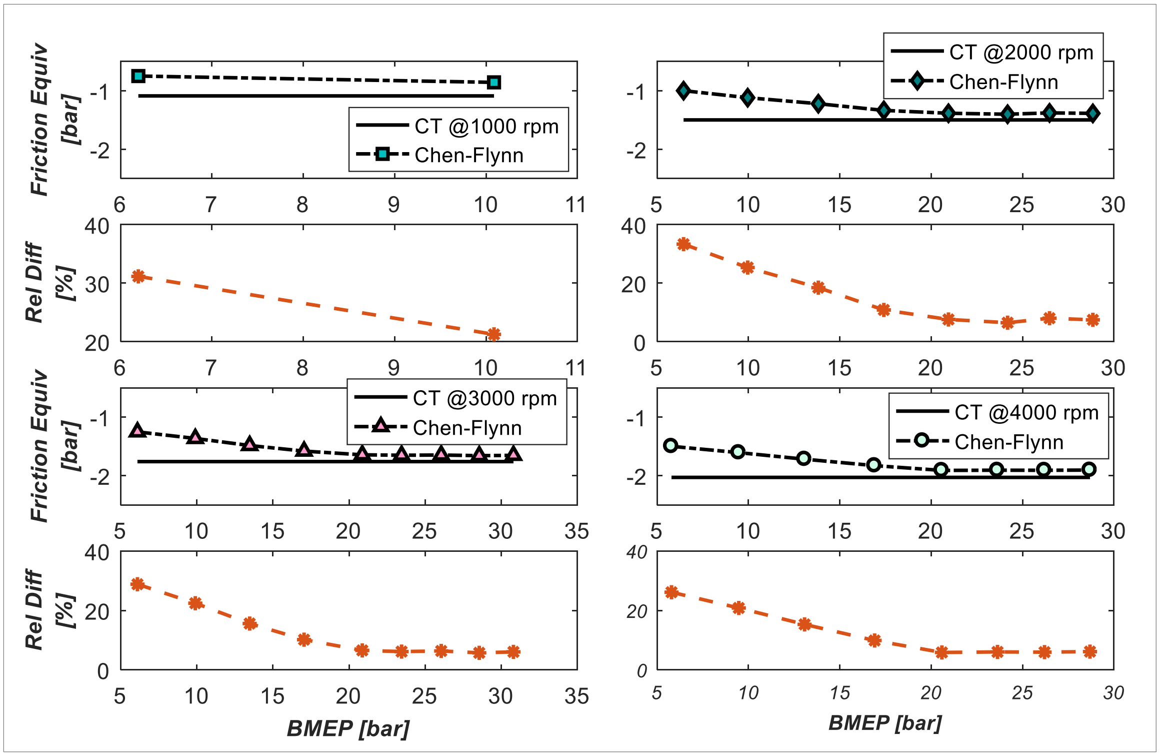

Figure 3.24 Segmented warmed-up closed-throttle (CT) BMEP curve of the 2.7-Liter EcoBoost® engine compared to the FMEP results obtained by the Chen-Flynn model at different loads and speeds.

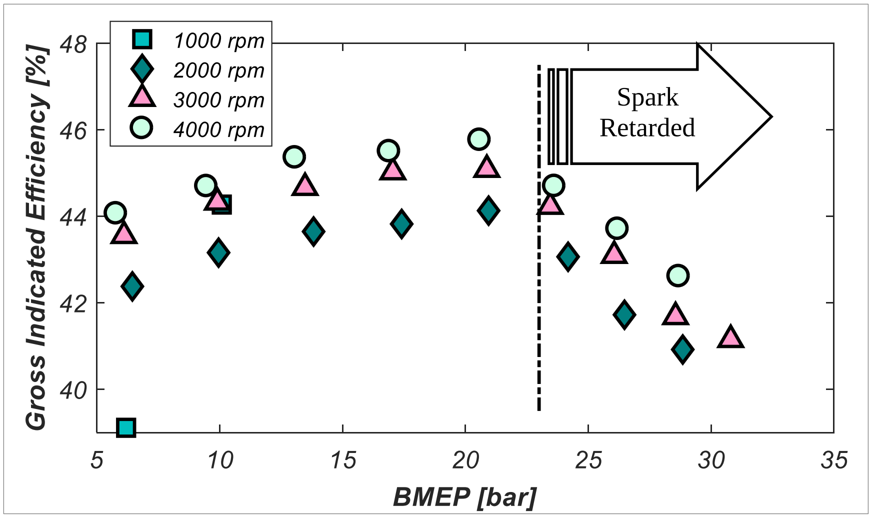

Figure 3.25 Gross indicated efficiency with respect to BMEP. The dash-dot line displays the 23 bar BMEP. The loads beyond this point were obtained by reducing the charge dilution, while the spark timings were retarded to maintain the 150 bar constraint for in-cylinder pressures.

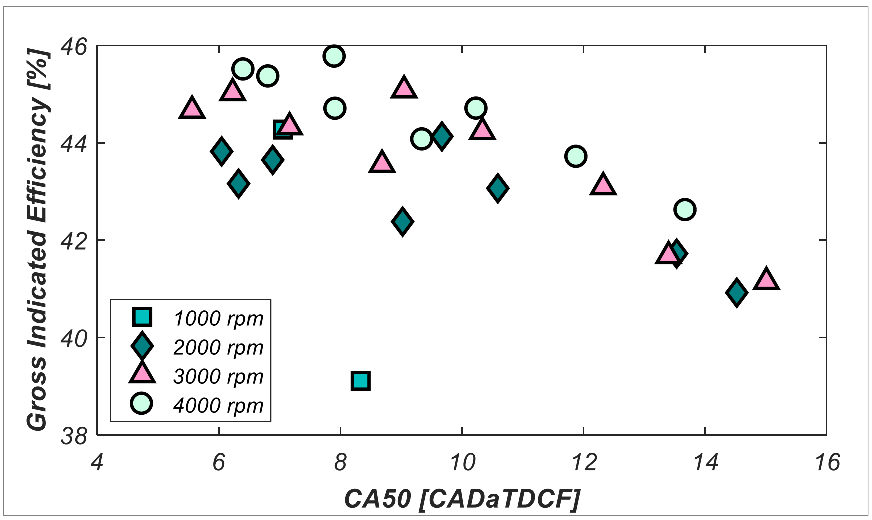

Figure 3.26 Gross indicated efficiency with respect to CA50. The data report an average CA50 of 7.6 CADaTDCF as the optimum CA50 for the current simulations performed on the DM-TJI engine. The data with retarded spark events were excluded in average value calculation.

Figure 3.26 represents gross indicated efficiencies with respect to CA50. The optimum CA50s in these simulations were ranged from 6 CADaTDCF to 9 CADaTDCF, with an average of 7.6 CADaTDCF. The data with retarded spark events were excluded in average value calculation. The optimum CA50 decreases with a decrease in 10-90% burn duration. The results found well agree with the best CA50s reported by other researchers to obtain maximum efficiency. The 50% mass fraction burned in the range of 8 to 10 CADaTDCF has been numerously described by others as the optimized range [111,119–121]. However, the same studies report a decline in optimum CA50, as the 10-90% burn duration decreases. The combustion characteristics obtained for the current simulations were summarized in Appendix A, Table A.3.

The power requirements for delivering air to the pre-chamber were calculated based on Womack fluid power design sheet [109] and summarized in Appendix A, Table A.1. Figure 3.27 displays the results for the pre-chamber power requirements of the DM-TJI engine as the percentage of gross IMEP (IMEPg). In general, relative work required decreases, as engine speed increases. It seems that ~2% of the gross work generated by the engine at each operating condition would be used toward the ancillary work for the pre-chamber of a DM-TJI engine under highly dilute conditions (40% EGR). The work required decreases with a decrease in main chamber charge dilution (BMEPs above 23 bar in Fig. 3.27).

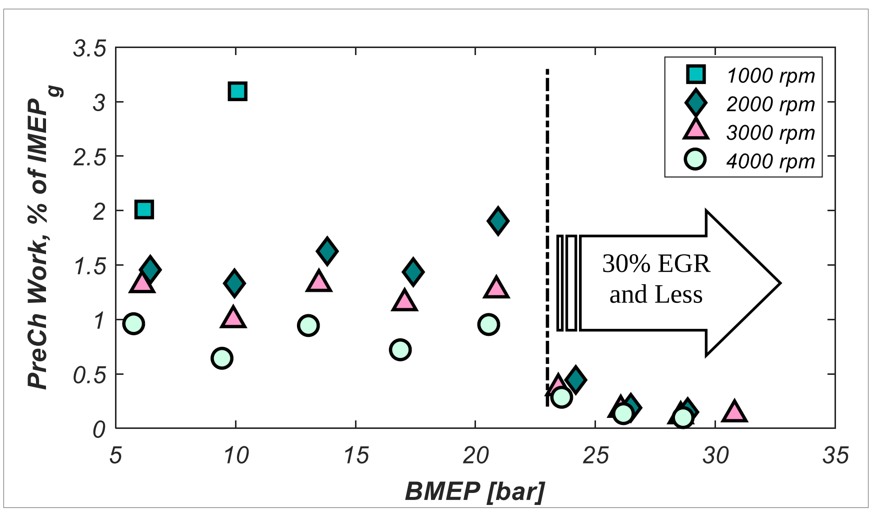

Figure 3.27 Power requirements for delivering air to the pre-chamber of a DM-TJI engine as the percentage of IMEPg. Details of these calculations were explained under "Energy Input for a Pre-Chamber Air Valve" and summarized in Appendix A, Table A.1.

3.7 Summary and Conclusion

The chapter first described the history of pre-chamber-initiated combustion technologies with small pre-chamber volumes (<3% of the clearance volume). The MAHLE Powertrain turbulent jet ignition (TJI) system was introduced, and the technology difficulties under highly dilute conditions were discussed. The MSU Dual Model, Turbulent Jet Ignition (DM-TJI) combustion technology, which is a solution to the difficulties of the MAHLE TJI combustion system, was then experimentally and numerically discussed in this chapter.

To date, the DM-TJI systems have proven a high level of improvements in thermal efficiency compared to conventional IC engines. However, some questions were still unanswered. A major question regarded the power requirements for delivering air to the pre-chamber of a DM-TJI system. Additionally, there was no study available to predict the expected efficiency of a DM-TJI engine in a multi-cylinder configuration. The work presented in this chapter, for the first time, predicted the ancillary work requirement to operate a DM-TJI system. A novel, reduced order, and physics-based model was also developed in this study to project the behavior of a DM-TJI engine with a pre-chamber air valve assembly.

The developed model included the intake/exhaust systems, pre-chamber purge valve, pre-chamber, main chamber, and the nozzle connecting the pre- to the main combustion chamber. Flow characteristics for all parts except for pre- and main combustion chambers were determined by solving for 1D Navier-Stokes equations. In addition, the current study employed a two-zone analysis for both pre- and main combustion chambers, while the GT-POWER WoschniGT heat transfer model was used to simulate heat transfer. Pre-chamber evaporation was compensated with a two-step fuel injection event. Burn dependency between pre- and main combustion chambers was also adapted from a previously developed and tested concept of a parameter-varying Wiebe function with a number of readjustments. The engine system model developed was calibrated based on experimental data from the Prototype II DM-TJI engine.

The experimental and numerical results demonstrated that:

- Power consumption to deliver pre-chamber air will not be a factor limiting implementation of the technology. In a four-cylinder configuration, it is predicted that 100 watts of power would be sufficient at 1500 rpm and 2000 rpm. The power requirement will increase at higher loads and speeds or under highly dilute conditions. However, by delivering the pre-chamber air during the appropriate time of compression, work will be recovered from the pre-chamber purge air during the expansion stroke of the piston.
- A stable combustion was convenient to reach at highly lean conditions, lambda ~2, for the throttle conditions both wide and partially opened. Combustion stability with an IMEP COV below 2.5% was observed under different spark timings and pre-chamber fuel strategies.
- The DM-TJI system comprises a high potential for improvements in thermal efficiencies at low to mid-load operating conditions. The DM-TJI system benefits from high thermal efficiencies close to HCCI-SACI combustion, and it does not involve the difficulties arising from HCCI-SACI combustion. These difficulties include the complex control mechanism and fuel intolerance.
- The numerical simulations were able to capture the experimental trends. The validity of the model in prediction of experiments was observed based on the standard metric of the coefficient of determination, as well as comparison plots for in-cylinder pressures. The numerical predictions for three metrics of main chamber combustion (gross IMEP, main chamber peak pressure, and main chamber phasing for the peak pressure) were within 5% of experimental data, with one exception happening at 6%. Additionally, the absolute RMS errors of in-cylinder pressures for both pre- and main combustion chambers were below 0.35.

The optimization results for model calibrating parameters were further studied to propose a predictive, generalized model for a DM-TJI engine. Such a model is essential to project the behavior of an engine equipped with the DM-TJI combustion technology over the entire engine fuel map. The possibility of knocking behavior was not studied in the current analysis. However, the author believes if it were possible to address the knocking behavior by any means including but not limited to in-cylinder charge preparation and/or combustion chamber design, the proposed generalized model should be capable of presenting reliable projections of the DM-TJI engine behavior.

The generalized model proposed was employed to predict a complete engine fuel map for a DM-TJI engine in a four-cylinder boosted configuration under highly dilute conditions (up to 40% EGR). The model in use provided the engine core data above the naturally aspirated (NA) curve of the engine. The core data below the NA line were extracted from the 2.7-Liter EcoBoost® engine embodied in a Ford F-150 vehicle. The data from the EcoBoost® engine were scaled to be used toward the fuel map generation of the DM-TJI engine.

The in-cylinder pressures for both pre- and main combustion chambers were bound to 150 bar for engine simulations completed in this study. The amount of EGR available in the pre-chamber at start of combustion was also limited to 30% to ensure a successful initiation of combustion processes. The 30% EGR presents the average status of the charge trapped in the pre-chamber at start of combustion. However, there may be some stratifications involved in the vicinity of the spark plug, leading to less EGR being exposed to the spark at the time of ignition in the pre-chamber. Further studies should be performed both experimentally and via 3D simulations to clarify the charge status in the pre-chamber at the time of spark occurrence. The engine fuel map projected for the DM-TJI engine will be further explored by a drive cycle analysis in the next chapter, Chapter 4.

CHAPTER 4

VEHICLE SIMULATION OF A DUAL MODE, TURBULENT JET IGNITION ENGINE OVER EPA DRIVING CYCLES

4.1 Introduction

A vehicle simulation allows to examine the outcome of different powertrain technologies on fuel consumption and emission, as well as vehicle performance. The DM-TJI system, as discussed in the previous chapter, is an advanced combustion technology for spark ignition engines to achieve high diesel-like thermal efficiencies and minimal engine-out emission. A vehicle simulation can accentuate the benefits obtained from such a technology, as it translates technical fuel map data into more tangible terms such as fuel consumption in miles per gallon (MPG) and overall thermal efficiencies. The work presented in this chapter translates the fuel map of the DM-TJI engine, generated in Chapter 3, into fuel economy and CO_2 emission over EPA driving cycles. The DM-TJI combustion technology and its effect on fuel economy and CO_2 emission were tested by using the Ford F-150 2.7-Liter as the base vehicle. The U.S. EPA advanced light-duty powertrain and hybrid analysis (ALPHA) was employed as the modeling platform to perform the vehicle simulation.

The chapter is organized as follows. The methodology used in this study is first described, followed by a short description of the U.S. EPA ALPHA model. After that, the fuel economy and CO_2 emission of a Ford F-150 2.7-Liter are reported while the vehicle's original engine was substituted with the fuel map generated for the DM-TJI engine. The results are compared to the results obtained for the same vehicle equipped with its original engine. Conclusions are drawn in the last section.

4.2 Methodology

The fuel map for a DM-TJI engine, generated in Chapter 3 using the introduced predictive-generalized model, was translated into fuel economy and CO2 emission over EPA driving cycles. The vehicle simulation was performed using the U.S. EPA ALPHA model. Apart from the engine map, which was meticulously studied over the course of this project, assumptions made for the rest of the components associated with the whole vehicle simulation were kept the same as already built ALPHA model for the Ford F-150 2.7-Liter EcoBoost®. The 2.7-Liter EcoBoost® is a turbocharged six-cylinder engine including the Ford port-fuel and direct-injection (PFDI) system with two injectors per cylinder; dual overhead cam design with variable intake/exhaust cam timing; and twin intercooled turbochargers for on-demand power [114]. Recall that the combustion behavior of a 1.6-Liter EcoBoost® engine embodied in a Ford Escape vehicle is already discussed in Chapter 2. The design specifics, however, may vary leading to different combustion behaviors for these two engines compared to one another.

The engine map of the Ford 2.7-Liter EcoBoost® was substituted with the map generated for the DM-TJI engine. The maximum torque curve of the 2.7-Liter EcoBoost® was satisfied via a four-cylinder configuration of the DM-TJI engine with higher brake mean effective pressures (BMEP), compared to the original engine. A maximum of 2 bar gauge boost pressure and 40% exhaust gas recirculation (EGR) were employed to generate the fuel map for the DM-TJI engine. Additionally, the in-cylinder pressures for both pre- and main combustion chambers were bound to a maximum of 150 bar at high-load operating conditions. More information can be found in Chapter 3.

The approach described led to perform an analysis of fuel consumption and CO_2 emission for a currently available Ford F-150 2.7-Liter EcoBoost®, while its original engine was substituted with an engine equipped with the DM-TJI combustion technology. A short description of the ALPHA model, which was used as the modeling platform for the vehicle simulation, follows.

4.3 ALPHA Vehicle Simulation Model

The advanced light-duty powertrain and hybrid analysis (ALPHA) was born through a regulatory commitment made by the U.S. Environmental Protection Agency (EPA) to perform a midterm evaluation (MTE) of the standards for model years (MY) 2022-2025 [115]. The ALPHA model was built as an in-house vehicle simulation tool and released to the public for full transparency and flexibility. ALPHA is a "physics-based, forward-looking, full vehicle computer simulation capable of analyzing various vehicle types with different powertrain technologies, showing realistic vehicle behavior" [101]. The EPA ALPHA model predicts fuel economy and CO_2 emission. The prediction of other types of emissions is not yet included in the ALPHA model. The ALPHA model was built in MATLAB/Simulink and has been validated using several resources including vehicle benchmarking, stakeholder data, and industry literature.

Daniel Barba, director of the U.S. EPA National Center for Advanced Technology (NCAT), presented a full set of vehicle benchmarking components with/without the currently available ALPHA model, at the 2016 SAE government-industry meeting. Table 4.1 is a duplication of what was presented at the time [122]. The 2015 Ford F-150 2.7-Liter EcoBoost® is the one used in the current study.

The ALPHA model is comprised of four systems: ambient, driver, powertrain, and vehicle. Aside from ambient and driver systems, the two others include a number of subcomponents.

Table 4.1 A set of vehicles benchmarked by the U.S. EPA with/without built-in ALPHA model, presented by Daniel Barba at 2016 SAE government-industry meeting [122].

			Conventional Vehicle	Engine	Transmission	Primary Reasons for Benchmarking	ALPHA Validation
1	**Turbo Engine**	**Car**	2013 Focus (Euro)	1.6L I4 EcoBoost (Euro)	6MT	large volume turbo, VVT, EURO-cal efficiency map	partial
2			2013 PSA	PSA 1.6L turbo	_	efficiency map	
3			2015 Volvo S60 T5	2.0L I4 turbo	8AT	I4 with 8AT, start-stop	yes
4			2016 Honda Civic	1.5L turbo	CVT	1.5L turbo, CVT	yes
5			2016 Acura ILX	2.4L I4 turbo	DCT8 w/TC	DCT8 with torque converter	yes
6		**Truck/SUV**	2013 Escape	1.6L I4 EcoBoost	6AT	large volume turbo, VVT, US-cal efficiency map	yes
7			2014 RAM 1500 EcoDiesel	3.0L V6 diesel (VM Matori)	8AT	(845RE) 8AT	yes
8			2015 Ford F-150	2.7L EcoBoost V6	6AT (same as GM 6L80)	next generation EcoBoost with VVT, integrated exhaust manifold, twin-scroll turbo, start-stop, US-cal efficiency map	yes
9	**Naturally Aspirated Engine**	**Car**	2013 Malibu Base	2.5L I4 GDI engine	6AT (6T40)	shift algorithm, transient fueling	yes
10			2013 Chevrolet Malibu Eco	2.4L I4	6AT (6T40)	BAS operation, start-stop	
11			2013 Jetta hybrid	1.4L I4	P2, DCT7	DCT operation, P2 hybrid operation	yes
12			2013 Mercedes E350	ETEC diesel	7AT	diesel operation, 7AT	yes
13			2013 Altima SV	2.5L I4	Jatco CVT8	CVT operation	yes
14			2014 US Mazda 6	SkyActiv 2.5L I4	6MT		
15			2014 US Mazda 3	SkyActiv 2.0L I4, 13:1CR	6AT	advanced NA engine operation	partial
16			2014 Dodge Charger 5-spd	3.6L V6	5AT(NAG1)	5-speed operation	yes
17			2014 Dodge Charger 8-spd	3.6L V6	8AT (8HP45)	8AT to compare with 5AT with same engine	yes
18		**Truck/SUV**	2014 RAM 1500 HFE	3.6L V6	8AT (845RE)	8-speed operation	yes
19			2014 Chevy Silverado 1500 2WD	4.3L EcoTec3 V6/V3	6AT (6L80 MYC)	cylinder deactivation, limited 6AT benchmarking	yes
20			2015 BMW X5 xDrive 35d	3.0L I6 Diesel	8AT (845RE)		yes

4.3.1 Ambient System

The ALPHA model is built to regenerate the test data produced by chassis dynamometer certification tests. Therefore, the ambient system is included in the model to define the test ambient characteristics.

4.3.2 Driver System

The driver system in the ALPHA model is designed to follow the vehicle speed versus time for different driving cycles, such as UDDS (urban dynamometer driving schedule), FTP (federal test procedure), HWFET (highway fuel economy test), etc. The driver system is a proportional-integral-derivative (PID) control driver that involves a small look ahead to consider the upcoming accelerations in its calculations. This particular feature can be necessary to overcome the delay caused by the large inertia of the vehicle and drivetrain. The driver PID output is then separated into separate accelerator and brake signals for use by their respective component models.

The engine speed at a given point in the drive cycle is calculated from the simulated vehicle speed based on transmission strategies and the torque converter model. The torque converter model simulates the fluid coupling used for low speed driving and provides appropriate load on the engine when the vehicle is stopped, and the transmission is in gear. The quantity of torque required is obtained from the driver model accelerator demand to match the desired vehicle speed, an idle speed controller, and requests from the transmission during shifts [101]. The torque calculated from these inputs is then modified using an engine torque response model, in order to match the torque response of naturally aspirated and turbocharged engines [123]. The resulting power from target engine torque and speed are compared to the best BSFC points of the engine fuel map for the power calculated. If the torque and speed fall far from the best efficiency region for that particular power, the gear ratio is shifted up or down to operate the engine at a more efficient point. The updated engine torque and speed are used to interpolate the engine fuel map to estimate fuel consumption. The generated torque also flows through the following downstream powertrain models to compute an updated vehicle speed and engine speed.

4.3.3 Powertrain System

The powertrain system includes four subcomponents: engine, electric, accessories, and transmission. Each of these subcomponents may or may not include other subsystems. A full description of each of these subcomponents can be found in the Proposed Determination prepared by the U.S. EPA [101]. The engine model, which is the focus of the current study, is built based on a full-engine fuel map covering all the loads and speeds from wide-open throttle (WOT) at full load to closed throttle at no-load conditions. The engine map developed by vehicle benchmarking, engine test data, and simulation tools such as GT-SUITE/GT-POWER is fed to the ALPHA model to define the engine subcomponent. The engine fuel map represents fuel mass flow rates versus engine crankshaft speed and brake torque. The lumped engine model in ALPHA does not include the in-cylinder combustion processes.

Over the course of simulation, the driver model calculates the engine torque and speed required to keep the simulated vehicle speed at the desired values. After that, the fuel flow rate corresponding to the torque and speed calculated is extracted from the engine fuel map. The engine fuel map, as described above, is provided as an input using GT-POWER simulations and/or experiments. The ALPHA model also includes some adjustments to simulate vehicle overhead functions with extra fuel demands. Vehicle simulations tend to underpredict fuel consumption, which is equivalent to overprediction of fuel economy. The extra fuel demands can come from heavy transient operation; accessory loads (power steering, A/C, electronics, etc.); torque transitions related to performance and drivability; and special controls for emissions and NVH (noise, vibration, and harshness) considerations [122].

4.3.4 Vehicle System

The vehicle system includes the chassis, its mass and forces associated with aerodynamic drag and changes in road grade [101]. The vehicle system also calculates the vehicle speed and distance traveled based on its vehicle speed integrator. The speed integrator estimates the acceleration of the vehicle from input force and the equivalent mass. Additionally, the coast down testing, or aerodynamic drag coefficient and frontal area data are used for load force calculations.

As one can see, a high level of details is involved in the ALPHA model to simulate the behavior which corresponds to vehicle benchmarking and engine experiments. Thus, the existence of a check and balance mechanism seems necessary to make sure that the physics involved is captured properly. The energy auditing component placed in the ALPHA acts as the check and balance verification tool and follows the energy flows. A properly done and verified model generally results in an energy error less than a few hundredths of a percent.

A full understanding of the ALPHA model with all its components is beyond the scope of the current study. This study aims to demonstrate a general understanding of the ALPHA model and use it as a tool toward the analysis of a vehicle equipped with the DM-TJI combustion technology over EPA driving cycles.

4.4 Results and Discussion

The fuel map for the DM-TJI engine is shown in Fig. 4.1. The map was produced for a four-cylinder (2.2-Liter) boosted configuration of the DM-TJI engine under highly dilute conditions up to 40% external exhaust gas recirculation (EGR). Details of model development and numerical approach for the DM-TJI engine can be found in Chapter 3. Figure 4.2 represents the fuel map for the 2.7-Liter EcoBoost® engine. The 2.7-Liter EcoBoost® was benchmarked by the U.S. EPA

NVFEL as an attempt to construct the steady-state fuel consumption map of such an engine [116]. The engine fuel map developed was eventually used as one of the many benchmarked engines (see Table 4.1) to validate the EPA ALPHA model.

The minimum brake specific fuel consumption (BSFC) for the DM-TJI engine shown in Fig. 4.1 is 201.1 g/kW-hr which yields a maximum brake thermal efficiency (BTE) of 41.3% (LHV=43.3 MJ/kg). The minimum BSFC for the Ford 2.7-Liter EcoBoost® in Fig. 4.2 is 227.8, yielding a maximum BTE of 36.5% (LHV=43.3 MJ/kg). The dash-dot grey lines in both figures represent the naturally aspirated curve of the engines. The solid pink lines are the path though the map with the lowest BSFC at a given power. As one can see, the four-cylinder configuration of the DM-TJI engine satisfies the maximum torque requirements of the 2.7-Liter EcoBoost® engine.

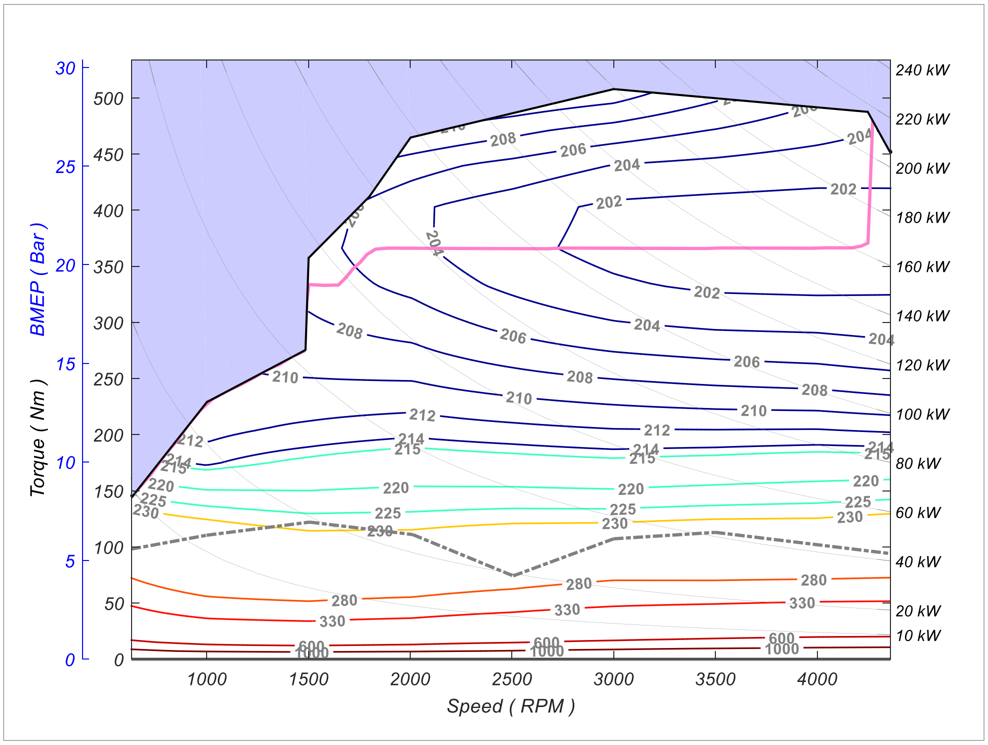

Figure 4.1 Brake specific fuel consumption (BSFC in g/kW/hr) map of the DM-TJI engine in a four-cylinder boosted configuration under highly dilute conditions up to 40% external EGR.

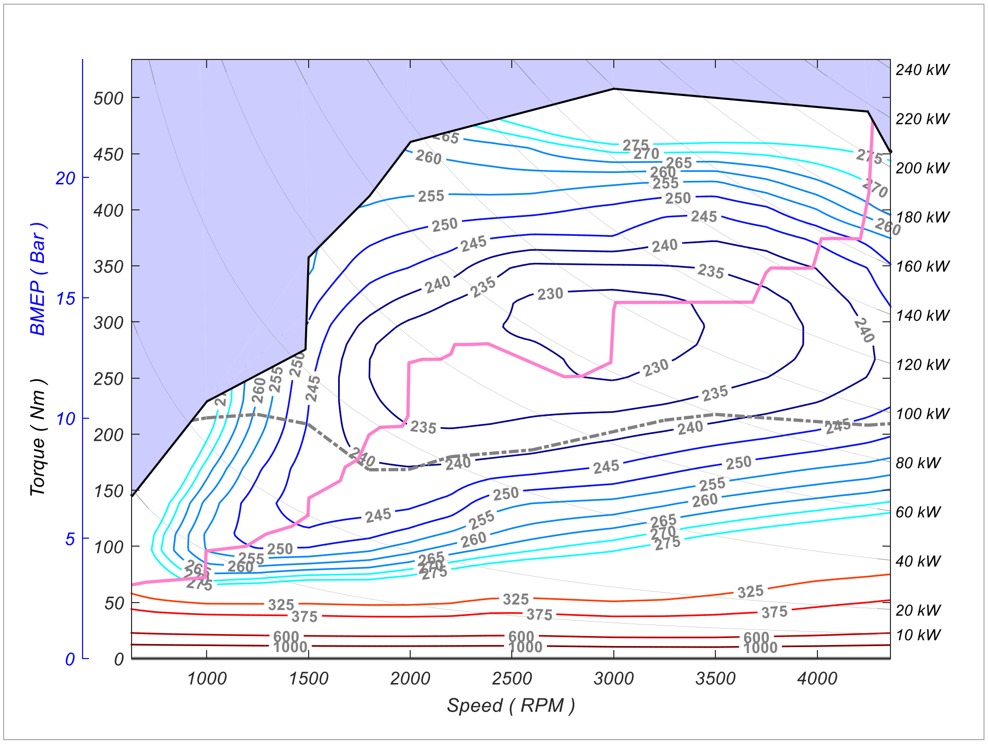

Figure 4.2 Brake specific fuel consumption (BSFC in g/kW/hr) map of the 2.7-Liter EcoBoost® embodied in an F-150 vehicle.

The drive cycle analysis was conducted on the Ford F-150 2.7-Liter vehicle, while the vehicle's original engine was substituted with the fuel map generated for the DM-TJI engine. The analysis was performed and reported over three EPA driving cycles: the federal test procedure (FTP), the highway fuel economy test (HWFET), and the high acceleration US06 driving cycle [124].

The EPA FTP is often called the EPA75 and represents the city driving cycle. The FTP is composed of two phases of EPA urban dynamometer driving schedule (UDDS), followed by the first 505 seconds of the UDDS (phase 1). Figure 4.3 displays the EPA FTP. The HWFET represents highway driving conditions under 60 miles/hr; see Fig. 4.4. The US06 is a high acceleration aggressive driving schedule which is commonly known as "supplemental FTP". The US06 consists of two phases. Figure 4.5 represents the US06 driving schedule.

The results of the drive cycle analysis demonstrate fuel economy improvements for the Ford F-150 vehicle equipped with the DM-TJI combustion technology compared to the vehicle's base engine, the 2.7-Liter EcoBoost®. Table 4.2 summarizes the results obtained over three different driving schedules. The last column in green displays the combined city/highway miles per gallon (MPG) for both engines compared to one another. Overall, the modeling approach used in the current study establishes ~13% fuel economy improvements over the combined city/highway driving schedules.

Table 4.2 Fuel economy test results for the 2.2-Liter DM-TJI engine embodied in an F-150 vehicle.

	FTP Average MPG				HWFET Average MPG	US06 Average MPG			2Cycle Combined MPG
	Phase 1	Phase 2	Phase 3	Total	-	Phase 1	Phase 2	Total	-
2.7-Liter EcoBoost®	23.34	24.22	27.08	24.74	33.75	15.29	23.97	21.29	28.12
2.2-Liter DM-TJI	26.48	28.00	30.62	28.33	36.95	17.57	26.76	23.97	31.65
% Improvement	13.45	15.62	13.09	14.50	9.46	14.90	11.62	12.62	12.55

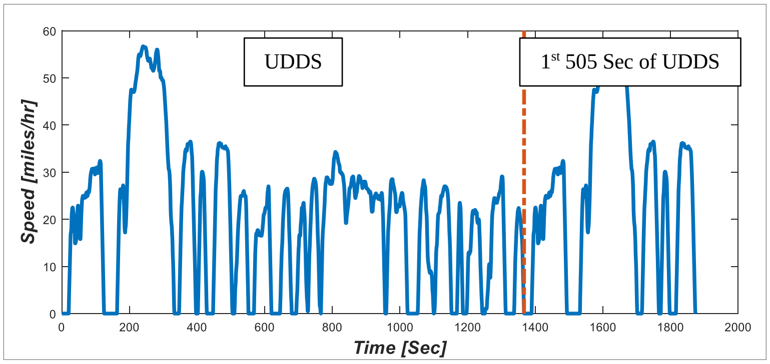

Figure 4.3 The federal test procedure (FTP) which is composed of the urban dynamometer driving schedule (UDDS), followed by the first 505 seconds of the UDDS [124].

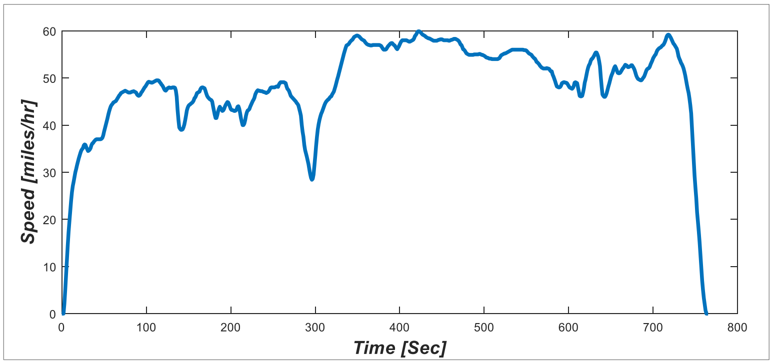

Figure 4.4 The highway fuel economy test driving schedule (HWFET) which represents highway driving conditions under 60 miles/hr [124].

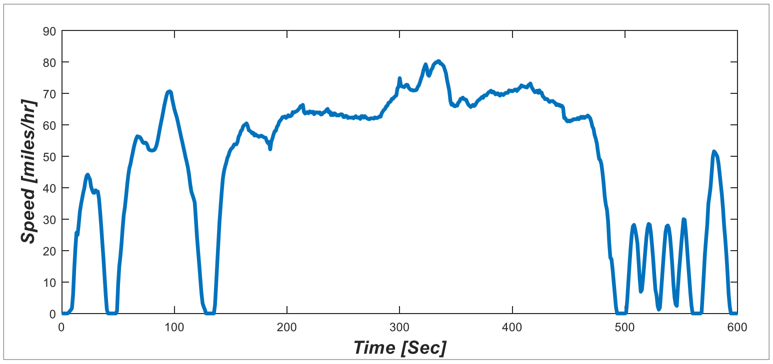

Figure 4.5 The US06 which is a high acceleration aggressive driving schedule and often called as "supplemental FTP" driving schedule [124].

The results obtained by the drive cycle analysis of the DM-TJI engine embodied in a Ford F-150 vehicle could be further improved with some readjustments. The main source of improvements could be the behavior of the DM-TJI engine under the naturally aspirated line in Fig. 4.1. Currently, the fuel economy data under the naturally aspirated line have been extracted from the 2.7-Liter EcoBoost® engine with the same BMEPs required. Unless the valve timings were to optimize, the intake system should be throttled to further decrease loads below the naturally aspirated line of the engine. Performing a valve timing study was beyond the scope of the current project. Throttling the intake system would compromise fuel economy improvements achieved by the DM-TJI system.

The second source of improvements could be engine downsizing. In the current study, power requirements of the Ford F-150 2.7-Liter vehicle were satisfied using a four-cylinder boosted configuration of the DM-TJI engine. Figures 4.6, 4.7, and 4.8 show the generated fuel map of the DM-TJI engine. The loads and speeds associated with power requirements of the engine over EPA driving schedules were also added to these figures. As one can see, engine operations happen below the best efficiency island for both city and highway driving cycles. The US06 driving schedule, shown in Fig. 4.8, makes some use of operating conditions under the best efficiency island. In general, a downsized engine would move the best efficiency island closer to the low-load operating conditions. Such a modification would enhance fuel economy improvements gained by the DM-TJI combustion technology.

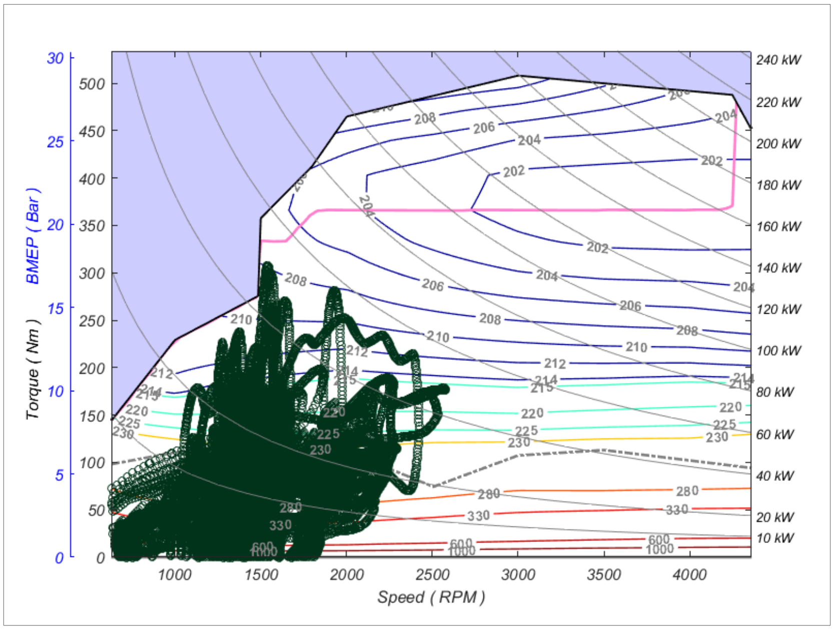

Figure 4.6 Brake specific fuel consumption (BSFC in g/kW/hr) map of the DM-TJI engine in a four-cylinder boosted configuration under highly dilute conditions up to 40% external EGR The green circles display the loads and speeds associated with the engine performance over the EPA federal test procedure, the city cycle.

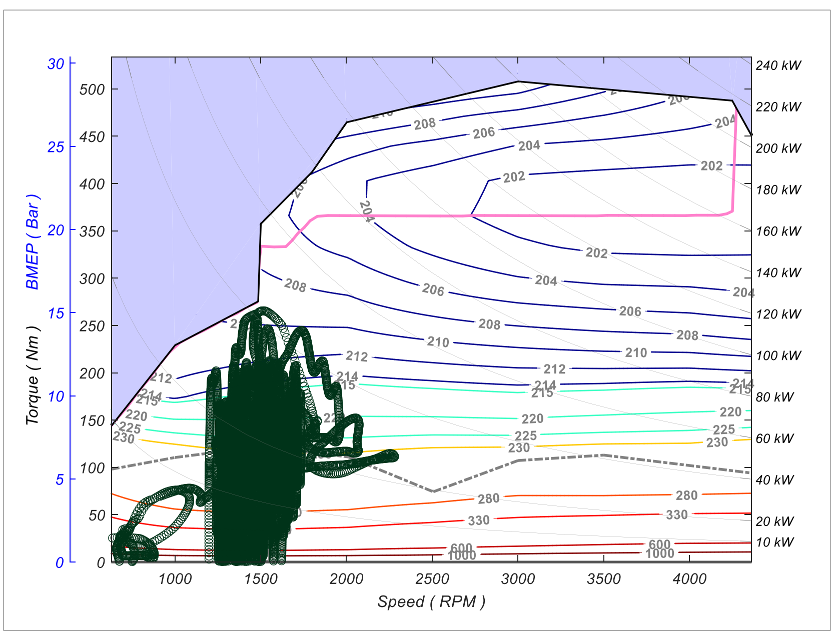

Figure 4.7 Brake specific fuel consumption (BSFC in g/kW/hr) map of the DM-TJI engine in a four-cylinder boosted configuration under highly dilute conditions up to 40% external EGR. The green circles display the loads and speeds associated with the engine performance over the EPA highway fuel economy test.

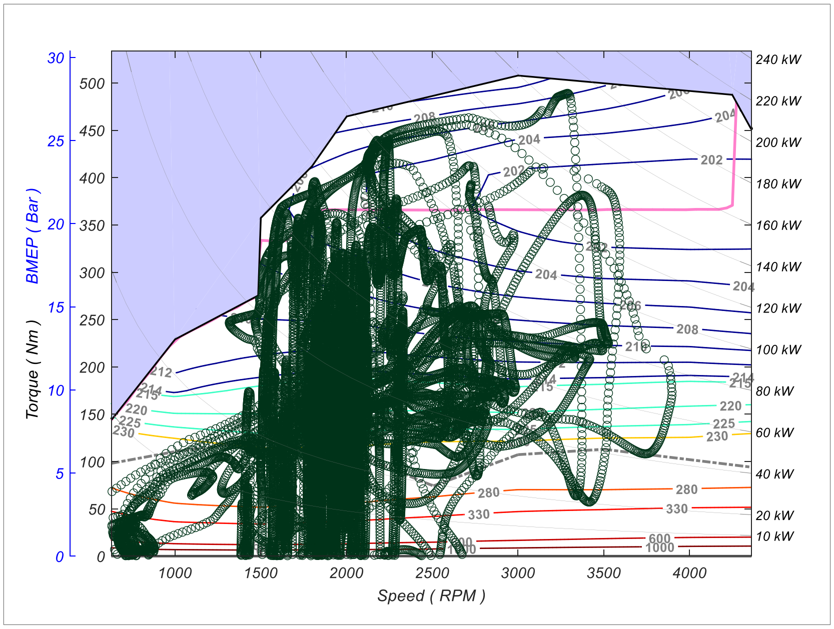

Figure 4.8 Brake specific fuel consumption (BSFC in g/kW/hr) map of the DM-TJI engine in a four-cylinder boosted configuration under highly dilute conditions up to 40% external EGR. The green circles display the loads and speeds associated with the engine performance over the EPA high acceleration US06 driving schedule.

The fuel economy improvements, subsequently, reduce CO2 emission. Table 4.3 compares the results of CO2 emission for the F-150 vehicle from one engine to the other. The DM-TJI combustion technology results in ~11% less CO2 emission over combined city/highway driving cycles.

Table 4.3 CO2 emission test results for the 2.2-Liter DM-TJI engine embodied in an F-150 vehicle.

	FTP Average gCO2/mile				HWFET Average gCO2/mile	US06 Average gCO2/mile			2Cycle Combined gCO2/mile
	Phase 1	Phase 2	Phase 3	Total	-	Phase 1	Phase 2	Total	-
2.7-Liter EcoBoost®	379.11	365.35	326.75	359.20	262.11	578.55	369.07	415.63	316.04
2.2-Liter DM-TJI	334.17	316.00	288.92	313.72	239.47	503.51	330.66	369.05	280.79
% Improvement	-11.86	-13.51	-11.58	-12.66	-8.64	-12.97	-10.41	-11.21	-11.15

4.5 Summary and Conclusion

This chapter described the drive cycle analysis of a vehicle equipped with the DM-TJI combustion technology. The DM-TJI system and its effects on fuel economy and CO2 emission were studied by using the Ford F-150 2.7-Liter EcoBoost® as the base vehicle. The maximum torque requirements of the 2.7-Liter EcoBoost® were satisfied in a four-cylinder boosted configuration of the DM-TJI engine. A maximum of 40% external exhaust gas recirculation (EGR) and 2 bar gauge boost pressure were employed toward the fuel map generation of the DM-TJI engine. The maximum in-cylinder pressures for both pre- and main combustion chambers were bound to 150 bar absolute. The U.S. EPA ALPHA model was utilized as the modeling platform for the vehicle simulation of the DM-TJI engine.

The results of the drive cycle analysis were reported over the EPA driving schedules: the federal test procedure (FTP), the highway fuel economy test (HWFET), and the high acceleration US06 cycle.

- The DM-TJI technology demonstrated fuel economy improvements of 14.5%, 9.5%, and 12.6% over the EPA FTP, HWFET, and US06 driving schedules; respectively. The combined city/highway driving cycles were observed to benefit from 12.6% improvements in fuel consumption compared to the results of the same vehicle with its original engine, the 2.7-Liter EcoBoost®.
- The engine technology enhancement using the DM-TJI system, also, resulted in 11.2% reduction of CO_2 emission over combined city/highway driving schedules.

The benefits achieved by the DM-TJI combustion technology could be further improved by valve timing optimizations and engine downsizing. A valve timing study was not conducted in the current work toward the fuel map generation of the DM-TJI engine. Instead, data regarding fuel consumptions under the naturally aspirated curve of the engine were extracted from the 2.7-Liter EcoBoost® engine. Additionally, operating conditions associated with both city and highway driving schedules were below the best efficiency island of the DM-TJI map generated. Downsizing the engine would move the best efficiency island of the DM-TJI engine closer to the low-load conditions. Such modifications would, beyond doubt, enhance fuel economy gains achieved by the DM-TJI combustion technology, as studied in the current work. The results of the drive cycle analysis for the DM-TJI engine embodied in an F-150 vehicle for both fuel economy and CO_2 emission are used toward the cost-benefit analysis of such a technology in Chapter 5.

CHAPTER 5

COST-BENEFIT ANALYSIS OF A DUAL MODE, TURBULENT JET IGNITION ENGINE

5.1 Introduction

Advanced technologies are needed to improve air quality and promote good use of natural resources. However, implementation of such technologies will add to the cost of vehicle production and subsequently lead to higher retail price of a vehicle. Sales of vehicles with higher retail prices will require acceptance by consumers and the belief that the value added by the increased cost of the technology is economically justifiable. As stated by Carley et al. in their macroeconomic study of federal and state automotive regulations [125]: “from a rational-choice perspective, the new vehicle consumer will purchase a new vehicle with superior fuel saving technology if, other things equal, the present value of the stream of fuel savings is greater than the upfront cost of the technology.” As a result, consumers will have the final say in the success or failure of a new, more expensive vehicle with higher, more efficient technologies. Results of a reliable cost-benefit analysis with clear assumptions, apart from its essentiality for automakers’ decision-making process, may set consumers on the right path toward an informed decision.

The work presented in this chapter describes the cost-benefit analysis of a vehicle equipped with the Dual Mode, Turbulent Jet Ignition (DM-TJI) engine. As stated earlier, the DM-TJI is a promising combustion technology for high-efficiency internal combustion (IC) engines. The results of the cost-benefit analysis performed on the vehicle with a DM-TJI system was compared to those of the vehicle with its original engine. The Ford F-150 2.7-Liter EcoBoost®, as described in Chapter 4, was chosen as the base vehicle for the current study. The Ford F-150 2.7-Liter is an industry-based vehicle with good reputation in both fuel economy and vehicle performance.

This chapter is organized as follows. First, the methodology used is described. After that, results are shown and discussed. The chapter is summarized and concluded at the end.

5.2 Methodology

The current study follows the methodology used by the U.S. EPA in the agency's cost-benefit analysis toward the "Proposed Determination on the Appropriateness of the Model Year 2022-2025 Light-Duty Vehicle Greenhouse Gas Emissions Standards under the Midterm Evaluation" [101]. A subset of economic and other key inputs employed was chosen in the current study toward the cost-benefit analysis of a vehicle equipped with the DM-TJI combustion technology. The results obtained were compared to those of the same vehicle with its original engine. A short description of the elements in use follows. A full description of all the key inputs used in the U.S. EPA cost-benefit analysis can be found in the Technical Support Document (TSD) prepared by that agency [101].

- **The On-Road Fuel Economy "Gap"**

The on-road fuel economy gap addresses the gap between the real world and the EPA standards compliance tests for fuel economy and tailpipe CO_2 emission[1]. A fuel economy factor of 0.77 was used in the Proposed Determination prepared by the U.S. EPA. Thus, a vehicle with a fuel economy compliance test value of 30 miles per gallon (mpg) is projected to have a real world fuel economy of 23 mpg. Such a factor is also translated into an emission factor of 1.3 (1/0.77). As a result, a

---

[1] Laboratory testing cannot project the effects of all the factors involved in real world operation. Particularly, the two-cycle combined city/highway driving schedules used for compliance do not account for the broad range of driver behavior and climatic conditions, typically experienced by U.S. drivers [101].

vehicle with a CO_2 emission compliance test value of 300 grams/mile is anticipated to have a real world CO_2 emission of 390 grams/mile. The same fuel economy factor of 0.77 was employed in the current study.

- **Fuel Prices and the Value of Fuel Savings**

The fuel price projections were extracted from the U.S. Energy Information Administration's (EIA) Annual Energy Outlook (AEO) 2018 [126]. The reported price values in 2017$ were scaled to 2019$, as the current study aims to report all the costs and benefits associated with the analysis in 2019$. The gross domestic product (GDP) chain-type price indices were employed for any price conversion from one year to another. The GDP price index is among measures of inflation in the U.S. economy and quantifies price changes in goods and services purchased by consumers, businesses, government, and foreigners, but not importers. The historical price indices were reported by the U.S. Bureau of Economic Analysis (BEA) and found in the Federal Reserve Economic Data's (FRED) website [127]. Projected values of GDP price indices, on the other hand, were found in the EIA's AEO 2018 [5]. Figure 5.1 presents the gasoline price projections for the years 2020 through 2050. The fuel prices were plotted in 2017 and 2019 dollars.

Studies show that typical new vehicle purchasers possess their vehicle for an average of six to seven years [128], while the maximum lifetime of a vehicle is 30 years for cars and 37 years for trucks [125]. National Research Council (NRC) in its information gathering process [129], "found that auto manufacturers perceive that typical consumers would pay upfront for only one to four years of fuel savings, a fraction of the lifetime-discounted present value." Helfand and Wolverton summarized the evidence from econometric studies of vehicle choice in their study of 2011 [130]. They concluded that "12 studies found significant undervaluing of fuel economy relative to its expected value, 8 studies concluded that consumers were close to the expected value, and 5 studies found consumers significantly overvalued fuel economy.” The authors also explained the complexity of the assessment, leading to the mixed conclusions attained. All things considered, the current study outlines the value of fuel savings in its cost-benefit analysis over both first three years and a full lifetime of the vehicle.

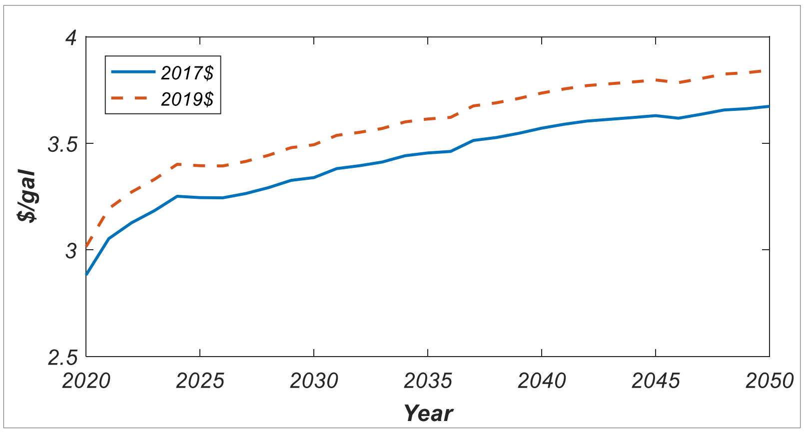

Figure 5.1 Gasoline price projections for the years 2020 through 2050, Source: U.S. Energy Information Administration.

- **Vehicle Mileage Accumulation and Survival Rates**

The vehicle miles traveled (VMT), reported by the U.S. EPA [101] and presented in Table 5.1, were used in estimating the total fuel savings and reduction of CO2 emission, as a result of a vehicle equipped with the DM-TJI combustion technology. The change in fuel consumption and CO2 emission during each of these model years was calculated as the difference between those of the vehicle equipped with a DM-TJI system as compared to the same vehicle with its original engine. The vehicle miles traveled at each model year were weighted by their corresponding survival probabilities reported in Table 5.1, prior to fuel consumption calculation and estimation of CO2 emission. The approach employed leads to the expected, average results over the full life time of a vehicle.

The current study assumes the year 2020 as the first year in which the DM-TJI technology may hit the market. Consequently, the year 2050 completes the first 30-year lifetime of this new technology. As it was mentioned earlier, the results of the cost-benefit analysis are reported for both first three years and the total lifetime of the vehicle to include the hypothesized range of consumers' attitude in foreseeing the value of fuel savings.

Table 5.1 Vehicle survival rates and vehicle miles traveled, Source: Proposed Determination by the U.S. EPA [101].

Vehicle Age	Estimated Survival Fraction (Cars)	Estimated VMT (Cars)
0	1.000	14,102
1	0.997	13,834
2	0.994	13,545
3	0.991	13,236
4	0.984	12,910
5	0.974	12,568
6	0.961	12,213
7	0.942	11,848
8	0.920	11,473
9	0.893	11,092
10	0.862	10,706
11	0.826	10,319
12	0.788	9,931
13	0.718	9,546
14	0.613	9,165
15	0.510	8,791
16	0.415	8,425
17	0.332	8,070
18	0.261	7,728
19	0.203	7,401
20	0.157	7,092
21	0.120	6,804
22	0.092	6,536
23	0.070	6,292
24	0.053	6,075
25	0.040	5,886
26	0.030	5,728
27	0.023	5,602
28	0.013	5,512
29	0.010	5,458
30	0.007	5,458
31	0.002	_

- **Fuel Economy Rebound Effect**

The U.S. EPA Proposed Determination [101] describes the rebound effect as "the additional energy consumption that may arise from the introduction of a more efficient, lower cost energy service which offsets, to some degree, the energy savings benefits of that efficiency improvement." The same document defines three distinct rebound effects: "VMT" rebound effect, "indirect" rebound effect, and "economy-wide" rebound effect.

The VMT rebound effect aims to consider extra energy usage in only the transportation sector, while the indirect rebound effect evaluates the purchase of other goods or services that consume energy with the cost savings from vehicle efficiency improvements. The economy-wide rebound effect covers the total increased demand for energy throughout the whole economy. Energy efficiency improvement may result in reduced market price of energy and, subsequently, increase the total demand for energy consumption [101]. The VMT rebound effect is the only one to be considered in the current analysis. When expressed as positive percentages, the VMT rebound effect is estimated as the percentage increase in vehicle miles traveled that results from a doubling of fuel efficiency, or halving of fuel consumption or per-mile fuel price.

To account for such an effect, a 10-percent value was chosen, which is as well in compliance with the EPA's methodology used in the Proposed Determination [101]. The 10-percent value reasonably compromises between historical estimates of the rebound effect and forecasts of its future values. The rebound effect and literature studies around it are extensively discussed in the Proposed Determination prepared by the U.S. EPA [101].

- **Non-GHG Health and Environmental Impacts**

There are two different approaches to address the effects of non-greenhouse gas (non-GHG) emissions in the cost-benefit analysis performed. The first approach subtracts the cost of any aftertreatment system needed for a vehicle with its original engine from the cost part of the analysis. The aftertreatment systems may include the three-way catalytic converter, NOx trap, gasoline particulate filter (GPF), etc. New technologies like the DM-TJI system may comply with the regulatory requirements for non-GHG emissions without a need for any aftertreatment system. The second approach accounts for the environmental benefits of that new technology compared to its more conventional counterpart and adds the estimated benefits to the benefit part of the cost-benefit analysis.

The author believes that the behavior of a vehicle equipped with the highly-dilute DM-TJI system does not much differ from that of the vehicle with its original engine, when it comes to non-GHG health and environmental impacts. It seems that any aftertreatment system needed for the vehicle with its original engine would be also required for the same vehicle equipped with the DM-TJI technology. Thus, the current study neither subtracts any cost from the cost part of the analysis nor adds any particular benefit to the benefit part of the cost-benefit analysis completed. The validity of the current approach regarding non-GHG health and environmental impacts should be further examined in future.

- **Social Cost of Greenhouse Gas Emissions**

The social cost of CO_2 (SC-CO_2) attempts to put a price on monetized damages arising from carbon emissions. Scientists also estimated the social cost of methane (SC-CH_4) and the social cost of nitrous oxide (SC-N_2O) with respect to climate change. The first attempt to estimate the SC-CO_2 happened during the Obama administration. In 2009, the Obama administration assembled the interagency working group (IWG) on SC-CO_2 in order to standardize the estimates used by federal agencies. The first SC-CO_2 estimates were reported in a Technical Support Document (TSD) issued by the IWG, co-chaired by the Federal Office of Management and Budget

(OMB) and Council of Economic Advisers (CEA) in February 2010 under Executive Order (EO) 12866 [131]. The IWG used three integrated assessment models (IAMs) to evaluate the SC-CO_2: dynamic integrated climate economy model [DICE], policy analysis of the greenhouse effect [PAGE], and climate framework for uncertainty, negotiation, and distribution [FUND] [132]. Each of these models were run 10,000 times based on random draws of their uncertainty parameters, for each of five socioeconomic scenarios, resulting in 150,000 estimates of SC-CO_2. The IAMs were run separately for each year and each of the three discount rates of 2.5%, 3%, and 5% [133]. The average of these estimations at each discount rate has been later summarized in a table as SC-CO_2 at different years. A fourth value has been also reported in the same table as the average of the 95th tail percentile of the results at 3% discount rate.

Reported estimates were revised in 2013 and 2016. The TSD released in August 2016 includes the SC-CH_4 and SC-N_2O, calculated on the same basis as SC-CO_2. However, based on President Trump's executive order 13783 [134] on "promoting energy independence and economic growth," the IWG was disbanded and all the TSDs on social cost of carbon, methane, and nitrous oxide were withdrawn. EO 13783 also directs the agencies, when monetizing the GHG impacts resulting from regulations, to consider the GHG impacts domestically and not internationally. Doing so, the EPA has presented new estimates for the SC-CO_2 in a document titled "Regulatory Impact Analysis for the Review of the Clean Power Plan: Proposal" [135]. In this document, the EPA estimated the cost of one ton of CO_2 to be between $1 and $6 in the year 2020. "That's down from the Obama administration's central (inflation adjusted) 2020 estimate of $45," as described by Chris Mooney in the Energy and Environment newsletter of the Washington Post on October 11th, 2017 [136].

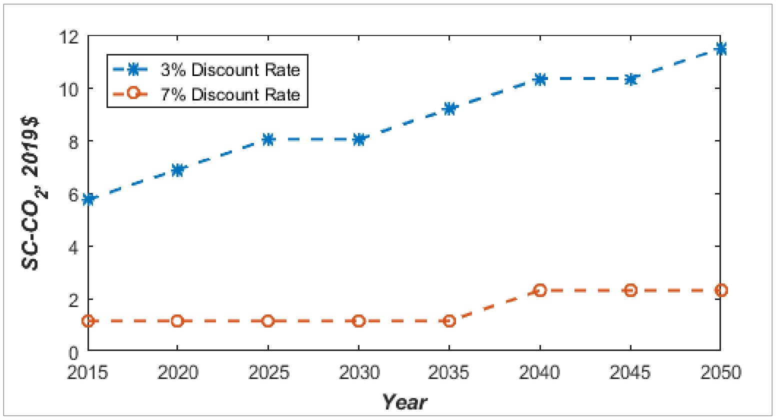

Figure 5.2 New SC-CO2 values reported by the Trump administration in a document titled "Regulatory Impact Analysis for the Review of the Clean Power Plan: Proposal" [135].

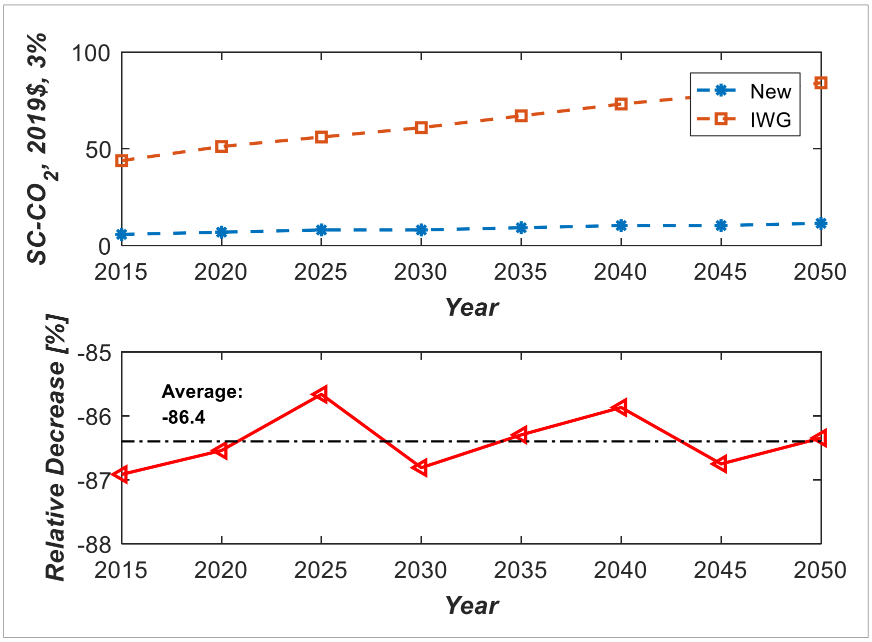

Figure 5.3 New SC-CO2 values at 3% discount rate compared to the former prices for the SC-CO2 reported by the IWG at the same discount rate. The new SC-CO2 values demonstrate an average of 86% reduction compared to the former values.

Figure 5.2 displays the new SC-CO2 calculations, reported by the Trump administration, in 2019$. These SC-CO2 values were originally reported in 2011$. As it was mentioned earlier, all the costs and benefits associated with the current analysis were scaled to 2019$. Figure 5.3 represents the new SC-CO2 values at 3% discount rate compared to the former values reported by the IWG. The prices for IWG SC-CO2, originally reported in 2007$, were also scaled to 2019$. The new SC-CO2 values demonstrate an average of 86% decrease with respect to the former values reported by the IWG in the Obama administration. A sensitivity analysis was performed to observe the results' dependency on SC-CO2. The new SC-CO2 values at 3% discount rate were increased by 600% to match the former SC-CO2 values at the same discount rate, see below:

$$\frac{New\ SC\text{-}CO_2 - Old\ SC\text{-}CO_2}{Old\ SC\text{-}CO_2} \sim -0.86 \tag{5.1}$$

$$\frac{Old\ SC\text{-}CO_2}{New\ SC\text{-}CO_2} \times 100 \sim 700\% \tag{5.2}$$

- **Discounting Future Benefits and Costs**

The discount rate refers to the interest rate used in discounted cash flow analysis to determine the present value of future cash flows. The future costs and benefits associated with all the elements described above were discounted using 3% and 7% discount rates. This approach is consistent with the Office of Management and Budget (OMB) guidance [101]. Equation 5.3 was employed to calculate the present value (PV) of the future cash flows, future value (FV).

$$PV = \frac{FV}{(1+i)^n} \tag{5.3}$$

where, i and n are the discount rate and the number of years passed from present, respectively.

- **The Extra Costs of the DM-TJI Technology**

Aside from key inputs used in the U.S. EPA cost-benefit analysis, the extra costs of the DM-TJI technology were also included in the current study. The cost of the DM-TJI system varies with configuration, including number of cylinders, control strategy, and application such as stationary, light, or heavy duty. An estimate was conducted to evaluate the extra costs of a DM-TJI system in a four-cylinder configuration, compared to the base engine studied (the 2.7-Liter EcoBoost®). The DM-TJI hardware for its newest configuration includes: extra injector, DM-TJI cartridge, valve drive system, air pump, extra assembly, and wiring and miscellaneous small parts. Consequently, the cost of the DM-TJI system in a four-cylinder configuration was estimated to be $78.90 in mass production. Known OEM prices were utilized in the cost calculation where available. The $78.90 estimate does not cover the indirect costs of the technology.

The indirect costs may be related to production (such as research and development), corporate operations (such as salaries, pensions, and health care costs for corporate staff), or selling (such transportation, dealer support and marketing) [101]. The current study employed the indirect cost multipliers (ICMs), developed by the U.S. EPA, to evaluate the indirect costs of the technology; see Table 5.2. The ICMs vary based on the complexity of the technology and the time frame under consideration. As it is explained in the Proposed Determination [101], “near term values account for differences in the levels of R&D, tooling, and other indirect costs that will be incurred. Once the program has been fully implemented, some of the indirect costs will no longer be attributable to the standards and, as such, a lower ICM factor is applied to direct costs.”

Table 5.2 Indirect cost multipliers used in the Proposed Determination by the U.S. EPA [101].

Complexity	Near Term	Long Term
Low	1.24	1.19
Medium	1.39	1.29
High1	1.56	1.35
High2	1.77	1.50

After reviewing this material and determining that the parts to be used in the DM-TJI system have already been put into production, although not in this configuration, an ICM of 1.39 was chosen, representing a medium complexity, near term application. A 1.39 ICM led to $109.67 price estimation of the technology. However, the current study used a cost number of $140.00 for the DM-TJI technology, assuming a potential understatement of ~25%.

5.3 Results and Discussion

Results of the current analysis are reported in two distinct sections. First, current costs and benefits of a DM-TJI system embodied in a Ford F-150 vehicle are described. The results obtained were compared to the results of the same vehicle with its original engine, the 2.7-Liter EcoBoost®. The second section includes potential improvements achieved by such a technology if the design were to optimize.

5.3.1 Costs and Benefits of a DM-TJI System

The two-cycle combined fuel economy of the DM-TJI engine embodied in a Ford F-150 vehicle was reported in Chapter 4, compared to that of the same vehicle with its original engine, the 2.7-Liter EcoBoost®. The two-cycle combined CO_2 emission of both engines was also discussed in the same chapter. The results obtained were used toward the cost-benefit analysis of the DM-TJI engine compared to the 2.7-Liter EcoBoost®. As described in the Methodology Section, a fuel economy factor of 0.77 was employed in the current study, to address the gap between the real world and the EPA standards compliance tests for fuel economy and tailpipe CO_2 emission.

Table 5.3 reports the total gallons of fuel consumed and produced CO_2 emission[2] for both engines over the life time of the vehicle (30 years). The fuel consumption and CO_2 emission were also reported in the same table with the 10-percent rebound effect, to consider the extra energy usage that may arise from the introduction of the DM-TJI system.

The price equivalent of total fuel consumed, and CO_2 produced for both engines is displayed in Fig. 5.4. The price values correspond to the total fuel consumption and CO_2 emission represented

[2] The vehicle miles traveled at each model year were weighted based on their corresponding survival probabilities in these calculations.

in Table 5.3, at two different discount rates. The social cost of CO_2 (SC-CO_2) was calculated based on prices published by the Trump administration (new) and the IWG (the Obama administration). The outcome of a 10-percent rebound effect, as assumed, is also depicted in this figure. The price equivalent of CO_2 emission is extremely low if the new estimates of SC-CO_2 (at either discount rate) were to use. New estimates of social cost of CO_2 at 7% discount rates lead to $47.20 worth of CO_2 for the DM-TJI engine compared to $52.47 for the 2.7-Liter EcoBoost®. These prices cover the whole life time of the F-150 vehicle equipped with the two engines. The highest price values for the produced CO_2 emission were obtained by the IWG SC-CO_2 at 3% discount rate.

Table 5.3 Total fuel consumption and CO_2 emission for the F-150 vehicle with the DM-TJI engine compared to the same vehicle with its original engine, the 2.7-Liter EcoBoost®. The effect of a 10-percent rebound effect is also shown in these calculations.

	Fuel Consumed (# Gallons)	CO_2 Emission (Metric Tons)
DM-TJI	7,345.00	65.28
DM-TJI + 10% Rebound Effect	7,437.20	66.09
EcoBoost 2.7L	8,266.98	73.47

The benefits of the DM-TJI engine compared to the 2.7-Liter EcoBoost® are displayed in Fig. 5.5. As discussed earlier in the Methodology Section, the benefits obtained by less fuel consumption of the DM-TJI engine in comparison with the other engine are reported over both first three years and the whole life time of the vehicle (30 years). The two different reporting periods were considered to include the hypothesized range of consumers' attitude in predicting the value of fuel savings. The social cost of CO_2, however, was calculated based on three different scenarios: the new SC-CO_2 at 3% discount rate, the new SC-CO_2 at 7% discount rate, and the IWG SC-CO_2 at 3% discount rate. The second bar plot in Fig. 5.5 stacked up the benefits associated with the social cost of CO_2 on the benefits gained by fuel savings. The SC-CO_2 values were not added to the results of fuel savings over the first three years, since the results were not to reflect the societal effects of fuel economy improvements but to prepare an answer to the consumer's attitude in foreseeing the value of fuel savings. As discussed in the Methodology Section, automakers claim that consumers consider only a small share of lifetime fuel savings in their purchase decisions. The benefits shown in this figure include the 10-percent rebound effect.

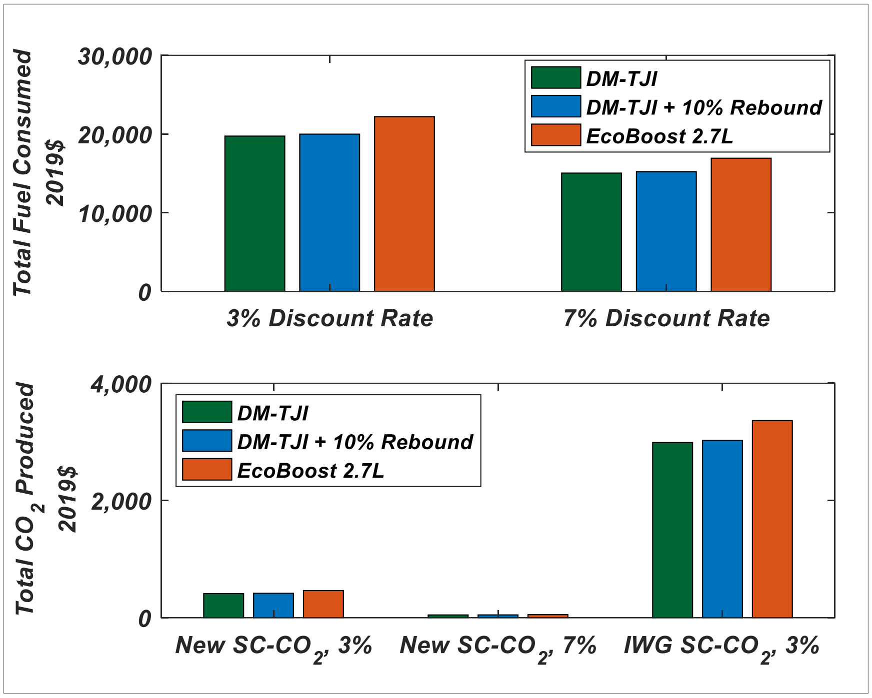

Figure 5.4 Price equivalent of total fuel consumed, and CO2 produced for the DM-TJI engine compared to the 2.7-Liter EcoBoost®. The effect of a 10-percent rebound effect is also depicted.

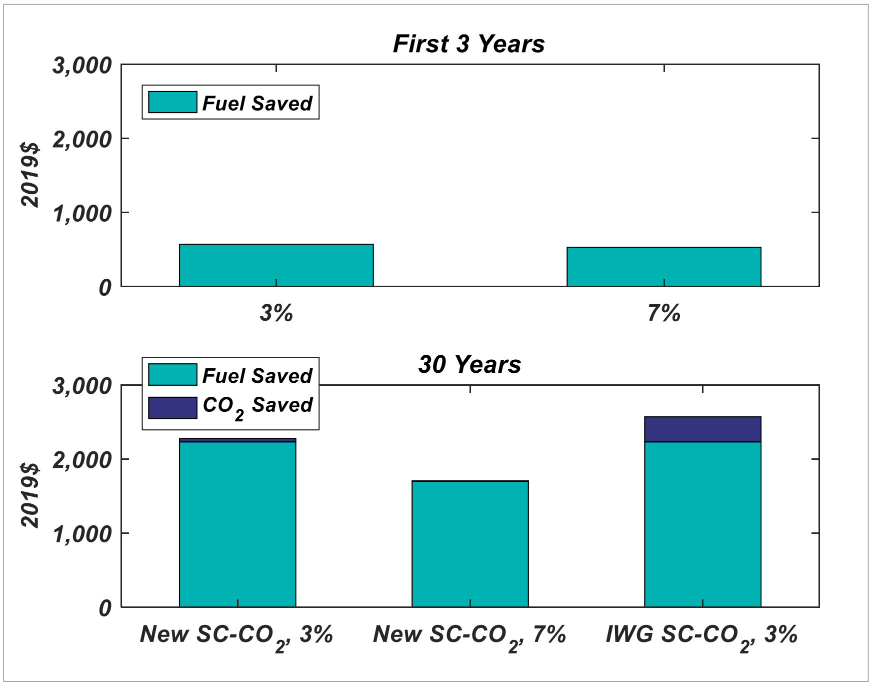

Figure 5.5 Benefits obtained by the DM-TJI engine compared to the 2.7-Liter EcoBoost®. The 10-percent rebound effect was included in these calculations.

The fuel economy improvements result in \$570.75 and \$529.29 worth of fuel savings over the first three years of the vehicle's life time at 3% and 7% discount rates, respectively. The maximum benefits as a summation of both fuel consumption and CO2 emission were observed to be \$2567.27 over the whole life time of the vehicle. The maximum benefits were resulted from the IWG SC-CO2 at 3% discount rate. Recall that the vehicle miles travelled at each model year were weighted with their corresponding survival probabilities to project the average, expected societal benefits, not the maximum possible to gain.

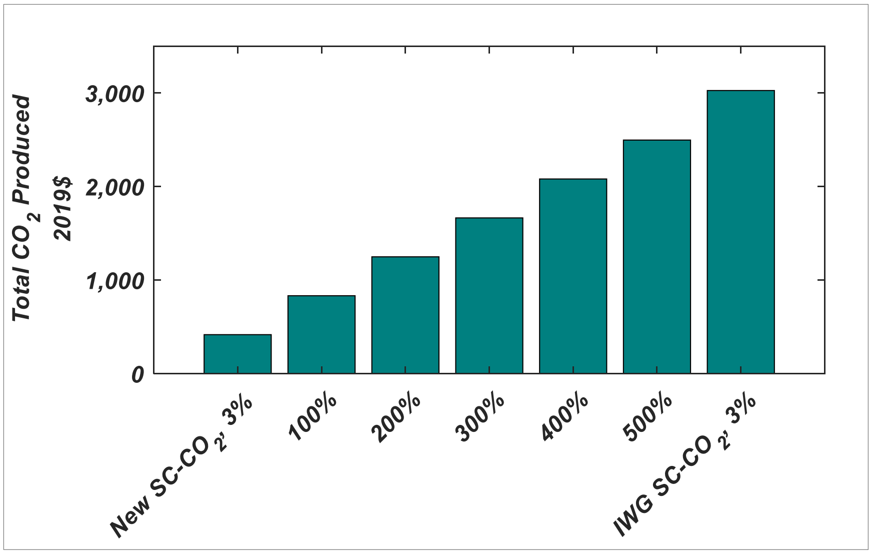

Figure 5.6 Price estimates of CO2 emission for a DM-TJI engine over the life time of the vehicle in which embodied. The new SC-CO2 at 3% discount rate was increased incrementally to match the former SC-CO2 reported by the IWG at the same discount rate. The 10-percent rebound effect was included in these calculations.

A sensitivity analysis was performed to study alternative scenarios between the new SC-CO2 calculated by the Trump administration and the IWG SC-CO2, the Obama administration. The new SC-CO2 values at 3% discount rate were incrementally increased by 600% to match the former SC-CO2 values at the same discount rate. Details of the analysis can be found in the Methodology Section under "Social Cost of Greenhouse Gas Emissions." Figure 5.6 displays the results obtained. The values shown in this figure indicate the price equivalent for CO2 emission of the DM-TJI engine, including the 10-percent rebound effect. The values cover the whole life time of the vehicle. The new SC-CO_2 at 3% discount rate leads to $416.07 worth of CO_2, while the price estimates reported by the IWG result in $3025.83 (~ new SC-$CO_2$ plus 600%). One may realize that the effect of CO_2 emission on any cost-benefit analysis revolving around environmental issues is highly dependent on how to evaluate the cost of CO_2 itself.

Table 5.4 Costs and benefits associated with the Ford F-150 vehicle equipped with the DM-TJI engine over the first three years of the vehicle's life time, compared to the same vehicle with its original engine, the 2.7-Liter EcoBoost®. The 10-percent rebound effect was included in these calculations.

	Costs	Benefits	Net
3% Discount Rate	$140.00	$570.75	$430.75
7% Discount Rate	$140.00	$529.29	$389.29

Table 5.5 Costs and benefits associated with the Ford F-150 vehicle equipped with the DM-TJI engine over the full life time of the vehicle, compared to the same vehicle with its original engine, the 2.7-Liter EcoBoost®. The 10-percent rebound effect was included in these calculations.

	Costs	Benefits	Net
New SC-CO_2, 3% Discount Rate	$140.00	$2,276.10	$2,136.10
New SC-CO_2, 7% Discount Rate	$140.00	$1,703.84	$1,563.84
IWG SC-CO_2, 3% Discount Rate	$140.00	$2,567.27	$2,427.27

The extra costs of a DM-TJI system in a four-cylinder configuration were estimated at $140.00, assuming a potential understatement of ~25%. Table 5.4 reports the costs and benefits associated with the Ford F-150 vehicle equipped with a DM-TJI combustion technology over the first three years of the vehicle's life time. As discussed earlier, the benefits of the technology over the first three years only include the gains obtained in regard to fuel savings. The results of the analysis over the full life time of the vehicle are reported in Table 5.5. The benefits reported in this table include the societal effects of CO_2 emission resulting from three different scenarios discussed for the SC-CO_2. The 10-percent rebound effect was included in these calculations. The last column in green, in both tables, displays the net benefits obtained in the current analysis. The extra costs of a DM-TJI system are compensated, even, with the lowest amount of benefits estimated at 7% discount rate over the first three years of the vehicle's life time. The gasoline price was incrementally decreased to find the maximum drop in fuel prices which makes the DM-TJI technology stay net positive. It turned out that the extra costs and benefits of the DM-TJI system would just cancel each other out if the gasoline price were to drop by 73% compared to the current projections. Such a decrease in the fuel price would lead to a gallon of fuel being worth 80 cents in the year 2020. Even with such low fuel prices, the benefits obtained in fuel savings from a DM-TJI system would pay for the extra costs of the technology over the course of first three years.

5.3.2 Potential Improvements

As discussed in Chapter 4, the results obtained for the current drive cycle analysis could be further improved. Re-defining the DM-TJI engine behavior under the naturally aspirated line of the engine was described as the main source of improvements. The current model defined the behavior of the DM-TJI engine in that region based on data scaling from the 2.7-Liter EcoBoost®. The effect of valve timings to gain potential improvements was explained in Chapter 4. Engine downsizing was also reported as a second source of improvements in the same chapter. In general, the current results of the drive cycle analysis are the first ever reported results for a DM-TJI engine embodied in an industry-based vehicle. As one may always argue, the first designs are almost never the best designs. There is definitely room for improvements regarding the current analysis of the DM-TJI engine.

Figure 5.7 displays the potential increase in benefits of a DM-TJI engine compared to the base engine if the current fuel economy obtained for the DM-TJI engine were to increase by an extra 5 and 10 percent. Table 5.6 reports the same values depicted in Fig. 5.7. Current improvements gained by the DM-TJI engine increase the two-cycle combined fuel economy by ~12.5%; see Chapter 4 for more details. An extra 5-percent improvement compared to the current fuel economy obtained for the DM-TJI engine (31.65 MPG) increases the relative improvement from 12.5% to 18%. An extra 10-percent improvement almost doubles the relative gains in fuel economy for the DM-TJI engine in comparison with the 2.7-Liter EcoBoost®. The extra 10-percent improvement corresponds to ~25% increase in fuel economy of a DM-TJI engine compared to its more traditional counterpart, the 2.7-Liter EcoBoost®. The current analysis considered that a 5-percent fuel economy improvement leads to a 5-percent reduction in CO_2 emission. The same was considered for the 10-percent value.

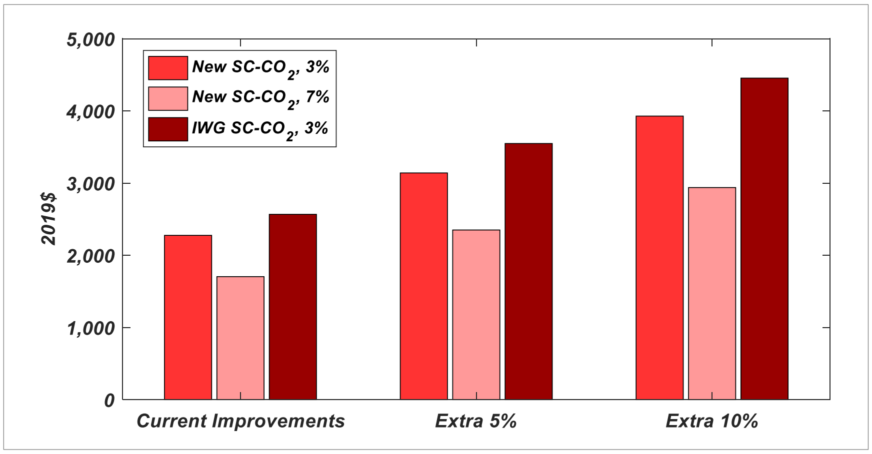

Figure 5.7 Potential improvements in benefits of a DM-TJI engine compared to the base engine if the current fuel economy obtained for the DM-TJI engine were to increase by an extra 5 and 10 percent. The 10-percent rebound effect is included in these calculations.

Table 5.6 Price equivalent of potential increase in benefits for a DM-TJI engine embodied in an F-150 vehicle compared to the same vehicle with its base engine. An assumption was made to increase the current fuel economy obtained for the DM-TJI engine with an extra 5 and 10 percent. The CO_2 emission was assumed to reduce with an extra 5 and 10 percent, accordingly. The 10-percent rebound effect is included in these calculations.

		Current Improvements	Extra 5%	Extra 10%
30 Years	New SC-CO_2, 3% Discount Rate	$2,276.10	$3,140.55	$3,928.35
	New SC-CO_2, 7% Discount Rate	$1,703.84	$2,350.33	$2,938.26
	IWG SC-CO_2, 3% Discount Rate	$2,567.27	$ 3,548.44	$4,454.39

The 25-percent relative improvement in both fuel economy and CO_2 emission for a DM-TJI engine embodied in an F-150 vehicle leads to ~1400 gallons of fuel in savings (an extra 600 gallons in comparison with the original results obtained in this analysis) and reduces CO_2 emission by ~13 metric tons (an extra 6 metric tons in comparison with the original results obtained in this analysis) over a full life time of the vehicle (30 years). The results are in comparison with the same vehicle equipped with the 2.7-Liter EcoBoost® engine. The lifetime-discounted present value of the gains described is reported in Table 5.6 as 4454.39 in 2019$. This is based on estimates for the SC-CO_2

by the IWG at 3% discount rate. Overall, the extra 10-percent fuel economy improvement and reduction in CO_2 emission leads to an extra ~73% increase in benefits compared to the benefits obtained by the current fuel economy of the DM-TJI engine. The extra 73-percent increase in benefits would be attained no matter which SC-CO_2 scenario is chosen; compare the first and third columns in Table 5.6.

5.4 Summary and Conclusion

A subset of the U.S. EPA economic and other key inputs used in their cost-benefit analysis was chosen toward such an analysis performed for a vehicle equipped with the DM-TJI engine. The results obtained were compared to those of the same vehicle with its original engine, the 2.7-Liter EcoBoost®. The extra costs of a DM-TJI system in a four-cylinder configuration were also considered in this analysis as $140.00, assuming a potential understatement of ~25%.

The current study performed for the Ford F-150 vehicle equipped with the DM-TJI technology demonstrates:

- The DM-TJI system embodied in an F-150 vehicle reduces both fuel consumption and CO_2 emission.
- As there are different scenarios available for how to evaluate the social cost of CO_2, the effect of CO_2 emission on any cost-benefit analysis revolving around environmental issues would vary substantially based on which scenario to follow.
- The extra costs of a DM-TJI system were observed to be compensated over the first three years of the vehicle's life time, even with the lowest estimate at 7% discount rate.
- The maximum lifetime-discounted present value of the net benefits of the DM-TJI technology were calculated as $2,427.27 at 3% discount rate, in comparison with the 2.7-

Liter EcoBoost®. The SC-CO_2 reported by the interagency working group (IWG) at 3% discount rate was employed in this calculation.

The current results of the drive cycle analysis are the first-ever reported results for a DM-TJI engine embodied in an industry-based vehicle. Thus, the potential improvements in benefits of such a technology were considered if the fuel economy obtained for the DM-TJI engine were to increase by an extra 5 and 10 percent. An extra 10-percent increase would lead to ~25% improvement for the current fuel economy of the DM-TJI system, compared to the 2.7-Liter EcoBoost®. Such an enhancement would reduce fuel consumption by ~1400 gallons and result in less CO_2 emission by ~13 metric tons over a full life time of the vehicle. The lifetime-discounted present value of the gains described was maximally estimated as 4,454.39 in 2019$. This is based on estimates for the SC-CO_2 by the IWG at 3% discount rate.

CHAPTER 6

CONCLUSIONS AND FUTURE WORK

6.1 Concluding Remarks

The number of vehicles powered by a source of energy other than traditional petroleum fuels, including electric vehicles, will increase as time passes. However, it appears that vehicles run on liquid fuels will be the major source of transportation for years to come. Advanced combustion strategies can improve fuel economy of internal combustion (IC) engines and reduce CO_2 emission. Such technologies can be obtained through highly dilute and low-temperature combustion (LTC) modes in IC engines. The Dual Mode, Turbulent Jet Ignition (DM-TJI) system is a distributed combustion technology to achieve LTC modes in spark ignition (SI) engines. The DM-TJI engine demonstrated the potential to provide diesel-like efficiencies and engine-out emission which can be controlled using a three-way catalytic converter.

In this dissertation, a zero-dimensional/one-dimensional simulation was completed to project the behavior of a DM-TJI engine with a pre-chamber air valve assembly. The simulations performed led to an engine fuel map for the DM-TJI system in a four-cylinder boosted configuration under highly dilute conditions (up to 40% external exhaust gas recirculation). The map developed was further explored via a drive cycle analysis of an industry-based vehicle equipped with the DM-TJI engine. The results obtained for the DM-TJI engine embodied in an industry-based vehicle were compared to the results of the same vehicle with its original engine. The vehicle equipped with the DM-TJI engine offered ~13% improvement in fuel economy and ~11% reduction in CO_2 emission over the EPA combined city/highway driving schedules. The benefits achieved by the DM-TJI system could be further increased by valve timing optimizations at lower loads and engine downsizing. The two-cycle combined fuel economy and CO2 emission, obtained by the drive cycle analysis of the DM-TJI engine, were used to conduct a cost-benefit analysis of such a technology. It appears that the extra costs of a DM-TJI system embodied in an industry-based vehicle could be compensated over the first three years of the vehicle's life time. The results of the cost-benefit analysis demonstrated a maximum of $2,427.27 for the lifetime-discounted present value of the net benefits of the DM-TJI technology, compared to the base engine examined. In this dollar saving estimate, the future benefits of the DM-TJI engine were discounted at 3% discount rate. The lifetime-discounted present value of the gains for a DM-TJI system was maximally estimated as 4,454.39 in 2019$ if the engine design were to optimize. The maximum gains estimated were resulted from an extra 10-perecent improvement in the current fuel economy calculated for the DM-TJI engine.

6.2 Recommendations for Future Work

The pre-chamber evaporation model employed in the current analysis is a simple two-step fuel injection event. Such a model may not precisely capture the fueling phenomenon inside the pre-chamber. An accurate prediction of the fuel behavior inside the pre-chamber is important, as it directly affects the projection of air/fuel ratio at the time of spark occurrence. The importance of this prediction is already known based on both literatures studied in this area and the experiments and numerical simulations conducted in the current work. A physics-based, more detailed evaporation model should further illuminate the mixture status inside the pre-chamber at the time of spark event. However, considering the number of calibrating parameters involved in this type of simulation, a suggestion is made to independently calibrate the evaporation model through optical studies of the pre-chamber itself.

The predictive, generalized model proposed for a DM-TJI engine was extracted based on the results obtained at low loads and low speeds. The behavior of a DM-TJI engine would differ, particularly, at high loads and low speeds in which the knocking behavior is more possible to occur. Additionally, the generalization defined for such a model is obtained based on experimental data under lean operating conditions. The behavior of the engine under highly dilute conditions may deviate from what is described. The validity of the proposed model should be examined by expanding the experiments over the entire engine fuel map, while including the charge dilution.

The amount of exhaust gas recirculation (EGR) trapped in the pre-chamber was limited to 30% over the course of simulations performed. The 30-percent limit was considered to ensure a successful initiation of combustion processes. However, the 30-percent EGR presents the average status of the charge trapped in the pre-chamber. There may be some stratifications involved in the vicinity of the spark plug, leading to less EGR being exposed to the spark plug at the time of ignition in the pre-chamber. Further studies should be conducted both experimentally and via three-dimensional simulations to clarify the charge status in the pre-chamber at the time of spark occurrence.

Fuel economy improvements and reductions in CO_2 emission achieved by the current analysis could be further increased by modifying the engine fuel map developed for the DM-TJI engine. The current model defined the engine behavior under the naturally aspirated curve of the engine based on experimental data from the base engine. A valve timing study should be performed to calculate the fuel economy for a DM-TJI engine in that region. Additionally, engine downsizing should increase the total gains attained, as it moves the best efficiency island of the map closer to the low-load operating conditions. In the current analysis, neither the city driving cycle (the federal test procedure, FTP) nor the highway driving schedule (the highway fuel economy test, HWFET) makes use of the operating conditions under the best efficiency island of the map developed.

All in all, the future is broad, and the path is there - only to be paved!

APPENDIX

APPENDIX A

NUMERICAL RESULTS UNDER HIGHLY DILUTE CONDITIONS

Table A.1 Energy requirements for the pre-chamber air valve.

Speed [rpm]	IMEPg [bar]	PreCh Valve Volume Flow Rate [SCFM]	PreCh Upstream Press [barA]	Watts Needed for 1 SCFM	1 Cyl - Watts	4 Cyl - Watts	Total Overhead Power for PreCh [Watts]	bar Equiv for Delivering Total Overhead Power	PreCh Work % of IMEPg
1000	7.09	0.44	5.38	105.17	45.89	183.55	262.09	0.14	2.01
1000	11.30	0.98	8.97	144.51	141.17	564.69	643.22	0.35	3.09
2000	7.56	0.67	6.73	121.60	81.60	326.41	404.95	0.11	1.46
2000	11.23	0.84	8.45	140.72	117.88	471.52	550.06	0.15	1.33
2000	15.30	1.22	12.46	171.00	209.20	836.79	915.33	0.25	1.63
2000	19.02	1.30	13.31	177.44	231.53	926.14	1004.67	0.27	1.44
2000	22.77	1.81	18.27	209.00	379.08	1516.34	1594.87	0.43	1.90
2000	25.70	0.64	7.94	134.12	85.52	342.06	420.60	0.11	0.44
2000	27.91	0.27	5.71	109.06	29.02	116.10	194.63	0.05	0.19
2000	30.28	0.20	5.60	107.91	22.09	88.38	166.92	0.05	0.15
3000	7.46	0.87	7.85	133.08	115.88	463.52	542.06	0.10	1.32
3000	11.38	0.95	8.99	144.62	136.73	546.90	625.44	0.11	1.00
3000	15.16	1.46	13.26	177.07	258.10	1032.42	1110.96	0.20	1.33
3000	18.85	1.53	14.30	183.22	279.58	1118.30	1196.84	0.22	1.15
3000	22.81	1.86	17.48	203.88	379.60	1518.40	1596.94	0.29	1.27
3000	25.20	0.77	8.48	141.02	109.26	437.03	515.57	0.09	0.37
3000	27.75	0.38	6.79	122.25	46.26	185.05	263.59	0.05	0.17
3000	30.25	0.27	5.09	100.82	27.39	109.57	188.10	0.03	0.11
3000	32.49	0.34	6.12	114.76	39.09	156.38	234.91	0.04	0.13

Table A.1 (cont'd)

4000	7.36	0.85	7.40	128.85	109.47	437.87	516.41	0.07	0.95
4000	11.15	0.84	7.64	131.31	110.91	443.65	522.19	0.07	0.64
4000	14.93	1.39	12.44	170.91	237.76	951.02	1029.56	0.14	0.94
4000	18.87	1.33	12.46	171.03	228.33	913.31	991.84	0.13	0.71
4000	22.71	1.88	16.90	200.12	375.75	1502.99	1581.53	0.21	0.95
4000	25.61	0.77	8.98	144.55	111.53	446.10	524.64	0.07	0.28
4000	28.15	0.41	6.05	113.77	46.79	187.15	265.69	0.04	0.13
4000	30.62	0.29	5.68	108.77	31.93	127.74	206.27	0.03	0.09

Table A.2 Fuel consumption calculations under highly dilute conditions.

Speed [rpm]	IMEPg [bar]	External EGR [%]	Intake Press [kPaA]	Cylinder Max Press [bar]	Mean Piston Speed [m/s]	NMEP [bar]	FMEP Chen-Flynn [bar]	BMEP WO PreCh Air Work [bar]	BMEP W PreCh Air Work [bar]	Torque [Nm]	PreCh Fuel [mg]	MainCh Fuel [mg]	Gross Indicated Eff [%]	Brake Eff [%]	BSFC [g/kW-hr]
1000	7.09	40.00	100.00	49.28	3.17	7.09	-0.75	6.34	6.19	108.84	0.99	22.16	39.11	34.18	243.79
1000	11.30	40.00	150.00	76.26	3.17	11.30	-0.86	10.44	10.09	177.24	0.99	31.61	44.27	39.54	210.78
2000	7.56	40.00	100.00	48.40	6.33	7.56	-1.00	6.56	6.45	113.31	0.99	21.80	42.38	36.15	230.49
2000	11.23	40.00	150.00	78.34	6.33	11.23	-1.12	10.11	9.96	174.95	0.99	32.25	43.16	38.28	217.70
2000	15.30	40.00	200.00	104.10	6.33	15.30	-1.22	14.07	13.82	242.89	1.63	43.15	43.65	39.45	211.25
2000	19.02	40.00	250.00	132.65	6.33	19.02	-1.34	17.68	17.41	305.87	1.86	53.59	43.82	40.11	207.75
2000	22.77	40.00	300.00	144.87	6.33	22.77	-1.39	21.38	20.95	368.03	2.33	63.59	44.13	40.60	205.24
2000	25.70	30.00	300.00	149.01	6.33	25.70	-1.40	24.29	24.18	424.87	1.31	74.94	43.06	40.52	205.65
2000	27.91	20.00	300.00	143.26	6.33	27.91	-1.38	26.53	26.48	465.19	0.99	84.48	41.72	39.58	210.53
2000	30.28	10.00	300.00	145.32	6.33	30.28	-1.39	28.89	28.85	506.85	0.99	93.56	40.92	38.98	213.77
3000	7.46	40.00	100.00	48.15	9.50	7.46	-1.25	6.21	6.11	107.31	0.99	20.89	43.55	35.66	233.67
3000	11.38	40.00	150.00	76.27	9.50	11.38	-1.37	10.02	9.91	174.06	1.03	31.79	44.32	38.57	216.07
3000	15.16	40.00	200.00	106.36	9.50	15.16	-1.49	13.68	13.48	236.78	1.37	42.01	44.66	39.69	209.94
3000	18.85	40.00	250.00	130.24	9.50	18.85	-1.58	17.27	17.05	299.55	1.71	51.78	45.02	40.73	204.61
3000	22.81	40.00	300.00	146.14	9.50	22.81	-1.64	21.16	20.87	366.74	1.97	62.68	45.08	41.26	201.98
3000	25.20	30.00	300.00	147.89	9.50	25.20	-1.65	23.55	23.45	412.08	1.04	71.76	44.23	41.16	202.45
3000	27.75	20.00	300.00	146.96	9.50	27.75	-1.65	26.10	26.06	457.81	0.99	81.30	43.09	40.46	205.97
3000	30.25	10.00	300.00	149.72	9.50	30.25	-1.66	28.59	28.55	501.70	0.99	91.75	41.68	39.34	211.81
3000	32.49	0.00	300.00	148.33	9.50	32.49	-1.65	30.84	30.80	541.15	0.99	99.92	41.15	39.00	213.68
4000	7.36	40.00	100.00	46.55	12.67	7.36	-1.50	5.86	5.79	101.70	0.99	20.35	44.06	34.66	240.41
4000	11.15	40.00	150.00	73.40	12.67	11.15	-1.61	9.54	9.47	166.41	0.99	30.88	44.69	37.97	219.49
4000	14.93	40.00	200.00	101.45	12.67	14.93	-1.72	13.21	13.07	229.68	1.19	40.88	45.36	39.71	209.86
4000	18.87	40.00	250.00	128.95	12.67	18.87	-1.83	17.04	16.90	297.01	1.21	51.78	45.50	40.76	204.43

Table A.2 (cont'd)

4000	22.71	40.00	300.00	149.38	12.67	22.71	-1.91	20.80	20.59	361.71	1.65	61.77	45.76	41.48	200.90
4000	25.61	30.00	300.00	148.48	12.67	25.61	-1.91	23.70	23.63	415.16	0.99	72.22	44.70	41.24	202.06
4000	28.15	20.00	300.00	148.82	12.67	28.15	-1.91	26.24	26.20	460.38	0.99	81.30	43.71	40.69	204.82
4000	30.62	10.00	300.00	147.96	12.67	30.62	-1.91	28.72	28.69	504.08	0.99	90.84	42.61	39.92	208.75

Table A.3 Combustion characteristics under highly dilute conditions.

Speed [rpm]	IMEPg [bar]	BMEP W PreCh Air Work [bar]	Gross Indicated Eff [%]	Brake Eff [%]	SPK [CADaTDCF]	* Purge Valve Timing [CADaTDCF]	PreCh Lambda @SPK [-]	CA50 [CADaTDCF]	Burn 10-90 [CAD]	Maximum Rate of Pressure Rise [bar/deg]
1000	7.09	6.19	39.11	34.18	-21.30	-112.92	0.93	8.33	25.50	1.59
1000	11.30	10.09	44.27	39.54	-19.05	-117.26	0.91	7.05	23.54	4.07
2000	7.56	6.45	42.38	36.15	-18.09	-111.46	0.95	9.02	24.75	2.09
2000	11.23	9.96	43.16	38.28	-18.69	-118.30	0.94	6.33	24.23	4.15
2000	15.30	13.82	43.65	39.45	-12.61	-93.22	0.95	6.89	22.15	8.14
2000	19.02	17.41	43.82	40.11	-14.16	-104.15	0.92	6.05	22.89	10.13
2000	22.77	20.95	44.13	40.60	-8.56	-101.48	0.95	9.67	23.34	17.53
2000	25.70	24.18	43.06	40.52	-9.00	-102.35	0.94	10.59	24.35	14.60
2000	27.91	26.48	41.72	39.58	-7.89	-104.41	0.96	13.53	26.30	12.90
2000	30.28	28.85	40.92	38.98	-7.29	-102.86	0.94	14.52	26.29	13.58
3000	7.46	6.11	43.55	35.66	-19.98	-114.44	0.96	8.69	24.21	2.09
3000	11.38	9.91	44.32	38.57	-17.60	-90.32	0.95	7.16	22.92	4.44
3000	15.16	13.48	44.66	39.69	-18.00	-112.74	0.93	5.56	22.62	6.93
3000	18.85	17.05	45.02	40.73	-14.29	-99.15	0.93	6.23	21.67	10.35
3000	22.81	20.87	45.08	41.26	-11.22	-95.45	0.96	9.05	23.08	14.55
3000	25.20	23.45	44.23	41.16	-11.35	-109.22	0.96	10.34	24.20	19.00
3000	27.75	26.06	43.09	40.46	-10.63	-97.37	0.95	12.32	25.92	12.90
3000	30.25	28.55	41.68	39.34	-9.72	-116.40	0.91	13.40	26.36	13.77
3000	32.49	30.80	41.15	39.00	-8.70	-103.70	0.95	15.01	26.33	13.10
4000	7.36	5.79	44.06	34.66	-23.15	-107.62	0.89	9.35	24.88	1.68
4000	11.15	9.47	44.69	37.97	-24.69	-110.26	0.95	7.92	25.37	2.86
4000	14.93	13.07	45.36	39.71	-20.17	-97.55	0.96	6.82	23.28	5.57
4000	18.87	16.90	45.50	40.76	-21.69	-96.00	0.96	6.41	24.14	6.74
4000	22.71	20.59	45.76	41.48	-15.61	-100.15	0.95	7.91	22.73	11.14

Table A.3 (cont'd)

4000	25.61	23.63	44.70	41.24	-15.50	-97.26	0.92	10.24	24.47	9.85
4000	28.15	26.20	43.71	40.69	-14.19	-111.96	0.91	11.89	25.44	10.71
4000	30.62	28.69	42.61	39.92	-12.70	-108.40	0.89	13.68	26.35	10.99

* The purge valve timings are defined as the location for the maximum of the pre-chamber valve lift profile with respect to top dead center of fire (TDCF).

Table A.4 Friction calculations using Chen-Flynn Model.

Speed [rpm]	IMEPg [bar]	Cylinder Max Press [bar]	Mean Piston Speed [m/s]	Ford F-150 Closed Throttle (CT) Curve [bar]	FMEP Chen-Flynn [bar]	CT vs. Chen-Flynn Relative Diff [%]
1000	7.09	49.28	3.17	-1.09	-0.75	31.15
1000	11.30	76.26	3.17	-1.09	-0.86	21.25
2000	7.56	48.40	6.33	-1.50	-1.00	33.31
2000	11.23	78.34	6.33	-1.50	-1.12	25.33
2000	15.30	104.10	6.33	-1.50	-1.22	18.46
2000	19.02	132.65	6.33	-1.50	-1.34	10.85
2000	22.77	144.87	6.33	-1.50	-1.39	7.59
2000	25.70	149.01	6.33	-1.50	-1.40	6.49
2000	27.91	143.26	6.33	-1.50	-1.38	8.02
2000	30.28	145.32	6.33	-1.50	-1.39	7.47
3000	7.46	48.15	9.50	-1.76	-1.25	28.83
3000	11.38	76.27	9.50	-1.76	-1.37	22.44
3000	15.16	106.36	9.50	-1.76	-1.49	15.60
3000	18.85	130.24	9.50	-1.76	-1.58	10.17
3000	22.81	146.14	9.50	-1.76	-1.64	6.56
3000	25.20	147.89	9.50	-1.76	-1.65	6.16
3000	27.75	146.96	9.50	-1.76	-1.65	6.37
3000	30.25	149.72	9.50	-1.76	-1.66	5.74
3000	32.49	148.33	9.50	-1.76	-1.65	6.06
4000	7.36	46.55	12.67	-2.03	-1.50	26.13
4000	11.15	73.40	12.67	-2.03	-1.61	20.84
4000	14.93	101.45	12.67	-2.03	-1.72	15.31
4000	18.87	128.95	12.67	-2.03	-1.83	9.89
4000	22.71	149.38	12.67	-2.03	-1.91	5.87
4000	25.61	148.48	12.67	-2.03	-1.91	6.05

Table A.4 (cont'd)

4000	28.15	148.82	12.67	-2.03	-1.91	5.98
4000	30.62	147.96	12.67	-2.03	-1.91	6.15

REFERENCES

REFERENCES

[1] 2015, “Quadrennial Technology Review 2015,” U.S. Department of Energy [Online]. Available: https://www.energy.gov/quadrennial-technology-review-2015. [Accessed: 23-Jul-2018].

[2] 2015, “Reducing Light-Duty Vehicle Energy Use and GHG Emissions,” U.S. Department of Transportation, Volpe National Transportation Systems Center [Online]. Available: https://www.volpe.dot.gov/news/reducing-light-duty-vehicle-energy-use-and-ghg-emissions. [Accessed: 23-Jul-2018].

[3] “Mobility of the Future,” MIT Energy Initiative [Online]. Available: http://energy.mit.edu/research/mobility-future-study/. [Accessed: 23-Jul-2018].

[4] O'Leary, M. B., 2018, “3Q: John Heywood on the Future of the Internal Combustion Engine,” MIT News | Massachusetts Institute of Technology [Online]. Available: http://news.mit.edu/2018/3q-mit-john-heywood-future-of-internal-combustion-engine-0418. [Accessed: 23-Jul-2018].

[5] 2018, “Annual Energy Outlook 2018,” U.S. Energy Information Administration [Online]. Available: https://www.eia.gov/outlooks/aeo/. [Accessed: 23-Jul-2018].

[6] Fraser, N., Blaxill, H., Lumsden, G., and Bassett, M., 2009, “Challenges for Increased Efficiency through Gasoline Engine Downsizing,” SAE International Journal of Engines, 2(1), pp. 991–1008.

[7] Estefanous, F., Mekhael, S., Badawy, T., Henein, N., and Zahdeh, A., 2014, “Multisensing Fuel Injector in Turbocharged Gasoline Direct Injection Engines,” J. Eng. Gas Turbines Power, 136(11), pp. 111502-111502–7.

[8] Vedula, R. T., Song, R., Stuecken, T., Zhu, G. G., and Schock, H., 2017, “Thermal Efficiency of a Dual-Mode Turbulent Jet Ignition Engine under Lean and near-Stoichiometric Operation,” International Journal of Engine Research, 18(10), pp. 1055–1066.

[9] De Boer, C., Bonar, G., Sasaki, S., and Shetty, S., 2013, “Application of Supercritical Gasoline Injection to a Direct Injection Spark Ignition Engine for Particulate Reduction,” SAE Technical Paper No. 2013-01-0257.

[10] Disch, C., Kubach, H., Spicher, U., Pfeil, J., Altenschmidt, F., and Schaupp, U., 2013, “Investigations of Spray-Induced Vortex Structures during Multiple Injections of a DISI Engine in Stratified Operation Using High-Speed-PIV,” SAE Technical Paper No. 2013-01-0563.

[11] Doornbos, G., Hemdal, S., and Dahl, D., 2015, "Reduction of Fuel Consumption and Engine-out NOx Emissions in a Lean Homogeneous GDI Combustion System, Utilizing Valve Timing and an Advanced Ignition System," SAE Technical Paper No. 2015-01-0776.

[12] Costa, M., Catapano, F., Marseglia, G., Sorge, U., Sementa, P., and Vaglieco, B. M., 2015, "Experimental and Numerical Investigation of the Effect of Split Injections on the Performance of a GDI Engine Under Lean Operation," SAE Technical Paper No. 2015-24-2413.

[13] Berni, F., Breda, S., D'Adamo, A., Fontanesi, S., and Cantore, G., 2015, "Numerical Investigation on the Effects of Water/Methanol Injection as Knock Suppressor to Increase the Fuel Efficiency of a Highly Downsized GDI Engine," SAE Technical Paper No. 2015-24-2499.

[14] Lucchini, T., D'Errico, G., Onorati, A., Bonandrini, G., Venturoli, L., and Di Gioia, R., 2012, "Development of a CFD Approach to Model Fuel-Air Mixing in Gasoline Direct-Injection Engines," SAE Technical Paper No. 2012-01-0146.

[15] Fatouraie, M., Wooldridge, M. S., Petersen, B. R., and Wooldridge, S. T., 2015, "Spray Development and Wall Impingement of Ethanol and Gasoline in an Optical Direct Injection Spark Ignition Engine," p. ASME Paper No. ICEF2015-1053, p. V001T02A004.

[16] Cho, K.-W., Assanis, D., Filipi, Z., Szekely, G., Najt, P., and Rask, R., 2008, "Experimental Investigation of Combustion and Heat Transfer in a Direct-Injection Spark Ignition Engine via Instantaneous Combustion Chamber Surface Temperature Measurements," Proceedings of the Institution of Mechanical Engineers, Part D: Journal of Automobile Engineering, 222(11), pp. 2219–2233.

[17] Brunt, M. F. J., and Platts, K. C., 1999, "Calculation of Heat Release in Direct Injection Diesel Engines," SAE Technical Paper No. 1999-01-0187.

[18] Egnell, R., 2001, "Comparison of Heat Release and NOx Formation in a DI Diesel Engine Running on DME and Diesel Fuel," SAE Technical Paper No. 2001-01-0651.

[19] Dowell, P. G., Akehurst, S., and Burke, R. D., 2017, "An Improved Rate of Heat Release Model for Modern High-Speed Diesel Engines," J. Eng. Gas Turbines Power, 139(9), pp. 092805-092805–14.

[20] Lindström, F., Angstrom, H.-E., Kalghatgi, G., and Möller, C. E., 2005, "An Empirical SI Combustion Model Using Laminar Burning Velocity Correlations," SAE Technical Paper No. 2005-01-2106.

[21] Hellström, E., Stefanopoulou, A., and Jiang, L., 2014, "A Linear Least-Squares Algorithm for Double-Wiebe Functions Applied to Spark-Assisted Compression Ignition," J. Eng. Gas Turbines Power, 136(9), pp. 091514-091514–7.

[22] Prakash, N., Martz, J. B., and Stefanopoulou, A. G., 2015, “A Phenomenological Model for Predicting the Combustion Phasing and Variability of Spark Assisted Compression Ignition (SACI) Engines,” p. ASME Paper No. DSCC2015-9883, p. V001T11A004.

[23] Spicher, U., Reissing, J., Kech, J. M., and Gindele, J., 1999, “Gasoline Direct Injection (GDI) Engines - Development Potentialities,” SAE Technical Paper No. 1999-01-2938.

[24] Huegel, P., Kubach, H., Koch, T., and Velji, A., 2015, “Investigations on the Heat Transfer in a Single Cylinder Research SI Engine with Gasoline Direct Injection,” SAE International Journal of Engines, 8(2), pp. 557–569.

[25] Stuhldreher, M., Schenk, C., Brakora, J., Hawkins, D., Moskalik, A., and DeKraker, P., 2015, “Downsized Boosted Engine Benchmarking and Results,” SAE Technical Paper No. 2015-01-1266.

[26] Heywood, J., 1988, Internal Combustion Engine Fundamentals, McGraw-Hill Education, New York.

[27] Gatowski, J. A., Balles, E. N., Chun, K. M., Nelson, F. E., Ekchian, J. A., and Heywood, J. B., 1984, “Heat Release Analysis of Engine Pressure Data,” SAE Technical Paper No. 841359.

[28] Chang, J., Güralp, O., Filipi, Z., Assanis, D. N., Kuo, T.-W., Najt, P., and Rask, R., 2004, “New Heat Transfer Correlation for an HCCI Engine Derived from Measurements of Instantaneous Surface Heat Flux,” SAE Technical Paper No. 2004-01-2996.

[29] Yun, H. J., and Mirsky, W., 1974, “Schlieren-Streak Measurements of Instantaneous Exhaust Gas Velocities from a Spark-Ignition Engine,” SAE Technical Paper No. 741015.

[30] Reddy, P. R., Krishna, D. M., Mallan, K. R. G., and Ganesan, V., 1993, “Evaluation of Combustion Parameters in Direct Injection Diesel Engines - An Easy and Reliable Method,” SAE Technical Paper No. 930605.

[31] Hariyanto, A., Bagiasna, K., Asharimurti, I., Wijaya, A. O., Reksowardoyo, I. K., and Arismunandar, W., 2007, “Application of Wavelet Analysis to Determine the Start of Combustion of Diesel Engines,” SAE Technical Paper No. 2007-01-3556.

[32] Shen, Y., Schock, H. J., and Oppenheim, A. K., 2003, “Pressure Diagnostics of Closed System in a Direct Injection Spark Ignition Engine,” SAE Technical Paper No. 2003-01-0723.

[33] Bitar, E. Y., Oppenheim, A. K., and Schock, H. J., 2006, “Model for Control of Combustion in a Piston Engine,” SAE Technical Paper No. 2006-01-0401.

[34] Katrašnik, T., Trenc, F., and Oprešnik, S. R., 2005, “A New Criterion to Determine the Start of Combustion in Diesel Engines,” J. Eng. Gas Turbines Power, 128(4), pp. 928–933.

[35] Ghojel, J. I., 2010, "Review of the Development and Applications of the Wiebe Function: A Tribute to the Contribution of Ivan Wiebe to Engine Research," International Journal of Engine Research, 11(4), pp. 297–312.

[36] Assanis, D. N., Filipi, Z. S., Fiveland, S. B., and Syrimis, M., 2003, "A Predictive Ignition Delay Correlation Under Steady-State and Transient Operation of a Direct Injection Diesel Engine," J. Eng. Gas Turbines Power, 125(2), pp. 450–457.

[37] Vedula, R. T., Song, R., Stuecken, T., Zhu, G. G., and Schock, H., 2017, "Thermal Efficiency of a Dual-Mode Turbulent Jet Ignition Engine under Lean and near-Stoichiometric Operation," International Journal of Engine Research.

[38] Song, R., Gentz, G., Zhu, G., Toulson, E., and Schock, H., 2017, "A Control-Oriented Model of Turbulent Jet Ignition Combustion in a Rapid Compression Machine," Proceedings of the Institution of Mechanical Engineers, Part D: Journal of Automobile Engineering, 231(10), pp. 1315–1325.

[39] Attard, W., 2012, "Turbulent Jet Ignition Pre-Chamber Combustion System for Spark Ignition Engines."

[40] Attard, W. P., and Parsons, P., 2010, "A Normally Aspirated Spark Initiated Combustion System Capable of High Load, High Efficiency and Near Zero NOx Emissions in a Modern Vehicle Powertrain," SAE International Journal of Engines, 3(2), pp. 269–287.

[41] Attard, W. P., and Parsons, P., 2010, "Flame Kernel Development for a Spark Initiated Pre-Chamber Combustion System Capable of High Load, High Efficiency and Near Zero NOx Emissions," SAE International Journal of Engines, 3(2), pp. 408–427.

[42] Attard, W. P., Fraser, N., Parsons, P., and Toulson, E., 2010, "A Turbulent Jet Ignition Pre-Chamber Combustion System for Large Fuel Economy Improvements in a Modern Vehicle Powertrain," SAE International Journal of Engines, 3(2), pp. 20–37.

[43] Attard, W. P., Bassett, M., Parsons, P., and Blaxill, H., 2011, "A New Combustion System Achieving High Drive Cycle Fuel Economy Improvements in a Modern Vehicle Powertrain," SAE Technical Paper No. 2011-01-0664.

[44] Attard, W. P., Kohn, J., and Parsons, P., 2010, "Ignition Energy Development for a Spark Initiated Combustion System Capable of High Load, High Efficiency and Near Zero NOx Emissions," SAE International Journal of Engines, 3(2), pp. 481–496.

[45] Toulson, E., Schock, H. J., and Attard, W. P., 2010, "A Review of Pre-Chamber Initiated Jet Ignition Combustion Systems," SAE Technical Paper No. 2010-01-2263.

[46] Oppenheim, A. K., 2013, Combustion in Piston Engines: Technology, Evolution, Diagnosis and Control, Springer Science & Business Media.

[47] Gussak, L. A., Turkish, M. C., and Siegla, D. C., 1975, "High Chemical Activity of Incomplete Combustion Products and a Method of Prechamber Torch Ignition for

Avalanche Activation of Combustion in Internal Combustion Engines," SAE Technical Paper No. 750890.

[48] Vedula, R. T., 2016, "Optical Investigations and Efficiency Measurements of a Dual-Mode Turbulent Jet Ignition Engine under Lean and High-EGR Near-Stoichiometric Conditions," Mechanical Engineering – Doctor of Philosophy, Michigan State University.

[49] Yamaguchi, S., Ohiwa, N., and Hasegawa, T., 1985, "Ignition and Burning Process in a Divided Chamber Bomb," Combustion and Flame, 59(2), pp. 177–187.

[50] Gussak, L. A., Karpov, V. P., Slutskii, V. G., and Spasskii, A. I., 1984, "Burning Rate and Stability in Forechamber Flame Ignition in an Internal-Combustion Engine," Combustion, Explosion, and Shock Waves (Historical Archive), 19(5), pp. 628–630.

[51] Gussak, L. A., Ryabikov, O. B., Politenkova, G. G., and Furman, G. A., 1974, "Yield of Atomic Hydrogen During Combustion of Methane and Hydrogen Mixtures with Air," Russian Chemical Bulletin (Historical Archive), 23(2), pp. 451–452.

[52] Gussak, L. A., Karpov, V. P., and Tikhonov, Y. V., 1979, "The Application of Lag-Process in Prechamber Engines," SAE Technical Paper No. 790692.

[53] Gussak, L. A., 1977, "LAG-Process of Combustion and Its Application in Automobile Engines," IMechE, C257/76, pp. 137–145.

[54] Gussak, L. A., 1983, "The Role of Chemical Activity and Turbulence Intensity in Prechamber-Torch Organization of Combustion of a Stationary Flow of a Fuel-Air Mixture," SAE Technical Paper No. 830592.

[55] Gussak, L. A., Ryabikov, O. B., Politenkova, G. G., and Furman, G. A., 1973, "Effect of Adding Individual Combustion Products on Combustion of Methane — Air Mixture," Russ Chem Bull, 22(9), pp. 2128–2128.

[56] Maxson, J. A., Hensinger, D. M., Hom, K., and Oppenheim, A. K., 1991, "Performance of Multiple Stream Pulsed Jet Combustion Systems," SAE Technical Paper No. 910565.

[57] Maxson, J. A., and Oppenheim, A. K., 1991, "Pulsed Jet Combustion—Key to a Refinement of the Stratified Charge Concept," Symposium (International) on Combustion, 23(1), pp. 1041–1046.

[58] Hensinger, D. M., Maxson, J. A., Hom, K., and Oppenheim, A. K., 1992, "Jet Plume Injection and Combustion," SAE Transactions, 101, pp. 571–580.

[59] Murase, E., and Hanada, K., 2000, "Enhancement of Combustion by Injection of Radicals," SAE Technical Paper No. 2000-01-0194.

[60] Murase, E., and Hanada, K., 2002, "Control of the Start of HCCI Combustion by Pulsed Flame Jet," SAE Technical Paper No. 2002-01-2867.

[61] Murase, E., and Hanada, K., 2002, “Ignition Timing Control of Homogeneous Charge Compression Ignition Engines by Pulsed Flame Jets,” Combustion Science and Technology, 174(5–6), pp. 129–140.

[62] Murase, E., Ono, S., Hanada, K., Yun, J. H., and Oppenheim, A. K., 1996, “Performance of Pulsed Combustion Jet at High Pressures and Temperatures,” JSAE Review, 17(3), pp. 245–250.

[63] Murase, E., Ono, S., Hanada, K., and Oppenheim, A. K., 1994, “Pulsed Combustion Jet Ignition in Lean Mixtures,” SAE Technical Paper No. 942048.

[64] Oppenheim, A. K., Beltramo, J., Faris, D. W., Maxson, J. A., Hom, K., and Stewart, H. E., 1989, “Combustion by Pulsed Jet Plumes - Key to Controlled Combustion Engines,” SAE Technical Paper No. 890153.

[65] Latsch, R., 1984, “The Swirl-Chamber Spark Plug: A Means of Faster, More Uniform Energy Conversion in the Spark-Ignition Engine,” SAE Technical Paper No. 840455.

[66] Dober, G. G., and Watson, H. W., 1999, “Modelling the Flame Enhancement of a HAJI Equipped Spark Ignition Engine,” IPC-10.

[67] Glasson, N., Lumsden, G., Dingli, R., and Watson, H., 1996, “Development of the HAJI System for a Multi-Cylinder Spark Ignition Engine,” SAE Technical Paper No. 961104.

[68] Hamori, F., and Watson, H. C., 2006, “Hydrogen Assisted Jet Ignition for the Hydrogen Fuelled SI Engine,” Lyon, France.

[69] Kyaw, Z. H., and Watson, H. C., 1992, “Hydrogen Assisted Jet Ignition for near Elimination of NOx and Cyclic Variability in the S.I. Engine,” Symposium (International) on Combustion, 24(1), pp. 1449–1455.

[70] Lawrence, J., and Watson, H. C., 1998, “Hydrocarbon Emissions from a HAJI Equipped Ultra-Lean Burn SI Engine,” SAE Technical Paper No. 980044.

[71] Toulson, E., 2008, “Applying Alternative Fuels in Place of Hydrogen to the Jet Ignition Process,” Department of Mechanical and Manufacturing Engineering – Doctor of Philosophy, University of Melbourne.

[72] Toulson, E., Watson, H. C., and Attard, W. P., 2007, “The Lean Limit and Emissions at Near-Idle for a Gasoline HAJI System with Alternative Pre-Chamber Fuels,” SAE Technical Paper No. 2007-24-0120.

[73] Toulson, E., Watson, H. C., and Attard, W. P., 2008, “The Lean Limit and Emissions of a Gasoline HAJI System That Employs Syngas in Place of Hydrogen as the Prechamber Fuel,” Munich, Germany, pp. F2008-SC-002.

[74] Toulson, E., Watson, H. C., and Attard, W. P., 2009, “Gas Assisted Jet Ignition of Ultra-Lean LPG in a Spark Ignition Engine,” SAE Technical Paper No. 2009-01-0506.

[75] Lezanski, T., Kesler, M., Rychter, T., Teodorczyk, A., and Wolanski, P., 1993, “Performance of Pulsed Jet Combustion (PJC) System in a Research Engine,” SAE Technical Paper No. 932709.

[76] Wolanski, P., and Oppenheim, A. K., 1999, “Controlled Combustion Engines (CCE),” p. SAE Technical Paper No. 1999-01-0324.

[77] Kesler, M., and Rychter, T. J., 1995, “A Jet Dispersed Combustion (JDC) Method to Stimulate Lean Burning in SI Piston Engines,” SAE Technical Paper No. 951006.

[78] Kito, S., Wakai, K., Takahashi, S., Fukaya, N., and Takada, Y., 2000, “Ignition Limit of Lean Mixture by Hydrogen Flame Jet Ignition,” JSAE Review, 21(3), pp. 373–378.

[79] Wakai, K., Kito, S., and Sumida, I., 1993, “Effect of Small Hydrogen Jet Flame on Augmentation of Lean Combustion,” SAE Technical Paper No. 931943.

[80] Couet, S., Higelin, P., and Moreau, B., 2001, “APIR: A New Firing Concept for the Internal Combustion Engines - Sensitivity to Knock and in-Cylinder Aerodynamics,” SAE Technical Paper No. 2001-01-1954.

[81] Robinet, C., Higelin, P., Moreau, B., Pajot, O., and Andrzejewski, J., 1999, “A New Firing Concept for Internal Combustion Engines: ‘I’APIR,’” SAE Technical Paper No. 1999-01-0621.

[82] Geiger, J., Pischinger, S., Böwing, R., Koß, H.-J., and Thiemann, J., 1999, “Ignition Systems for Highly Diluted Mixtures in SI-Engines,” SAE Technical Paper No. 1999-01-0799.

[83] Kettner, M., Rothe, M., Velji, A., Spicher, U., Kuhnert, D., and Latsch, R., 2005, “A New Flame Jet Concept to Improve the Inflammation of Lean Burn Mixtures in SI Engines,” SAE Technical Paper No. 2005-01-3688.

[84] Weng, V., Gindele, J., Töpfer, G., Spicher, U., Latsch, R., and Kuhnert, D., 1999, “Investigation of the Bowl-Prechamber-Ignition (BPI) Concept in a Direct Injection Gasoline Engine at Part Load,” p. Technical Paper No. 1999-01-3658.

[85] Najt, P. M., Rask, R. B., and Reuss, D. L., 2003, “Dual Mode Engine Combustion Process.”

[86] Kojic, A., Hathout, J.-P., Cook, D., and Ahmed, J., 2005, “Control of Auto-Ignition Timing for Homogeneous Combustion Jet Ignition Engines.”

[87] Kojic, A., Hathout, J.-P., Cook, D., and Ahmed, J., 2005, “Control of Auto-Ignition Timing for Combustion in Piston Engines by Prechamber Compression Ignition.”

[88] Getzlaff, J., Pape, J., Gruenig, C., Kuhnert, D., and Latsch, R., 2007, “Investigations on Pre-Chamber Spark Plug with Pilot Injection,” SAE Technical Paper No. 2007-01-0479.

[89] Lumsden, G., and Watson, H. C., 1995, “Optimum Control of an S.I. Engine with a Λ=5 Capability,” SAE Technical Paper No. 950689.

[90] Durling, H., 2005, “Igniter for Internal Combustion Engines Operating over a Wide Range of Air Fuel Ratios.”

[91] Durling, H. E., Johnston, R. P., and Polikarpus, K. K., 1995, “Torch Jet Spark Plug.”

[92] Durling, H. E., and Ralph, J. G., 2001, “Directed Jet Spark Plug.”

[93] Blank, D. A., 2007, “Combustion Control via Homogeneous Combustion Radical Ignition (Hcri) or Partial Hcri in Cyclic Ic Engines.”

[94] Blank, D. A., 2007, “Radical Controlled Autoignition in a HCRI Hydrogen DI Four-Stroke Diesel Engine with Reduced Heat Rejection,” SAE Technical Paper No. 2007-01-0013.

[95] Blank, D. A., and Pouring, A. A., 2004, “Radical Controlled Autoignition at Reduced Compression Ratios in a Hydrogen D.I. Diesel Engine with Piston Micro-Chambers,” SAE Technical Paper No. 2004-01-1846.

[96] Gandhi, H. S., Graham, G. W., and McCabe, R. W., 2003, “Automotive Exhaust Catalysis,” Journal of Catalysis, 216(1), pp. 433–442.

[97] Cho, H. M., and He, B.-Q., 2007, “Spark Ignition Natural Gas Engines—A Review,” Energy Conversion and Management, 48(2), pp. 608–618.

[98] Ortiz-Soto, E. A., Lavoie, G. A., Wooldridge, M. S., and Assanis, D. N., 2018, “Thermodynamic Efficiency Assessment of Gasoline Spark Ignition and Compression Ignition Operating Strategies Using a New Multi-Mode Combustion Model for Engine System Simulations,” International Journal of Engine Research, p. 1468087417752195.

[99] Song, R., Vedula, R. T., Zhu, G., and Schock, H., 2017, “A Control-Oriented Combustion Model for a Turbulent Jet Ignition Engine Using Liquid Fuel,” International Journal of Engine Research, p. 1468087417731698.

[100] Song, R., and Zhu, G., 2017, “Control-Oriented Crank-Resolved and State-Space Models for a Gasoline Turbulent Jet Ignition Engine,” 2017 American Control Conference (ACC), pp. 967–972.

[101] 2016, “Proposed Determination on the Appropriateness of the Model Year 2022-2025 Light-Duty Vehicle Greenhouse Gas Emissions Standards under the Midterm Evaluation,” U.S. Environmental Protection Agency, Office of Transportation and Air Quality, Assessment and Standards Division [online]. Available: https://nepis.epa.gov/Exe/ZyPDF.cgi?Dockey=P100Q3L4.pdf. [Accessed: 03-Oct-2018].

[102] “Downloads - The Trusted Leader in Measurement & Calibration Solutions,” Meriam Process Technologies [Online]. Available: https://www.meriam.com/resources/download/. [Accessed: 03-Oct-2018].

[103] Dowell, P. G., Akehurst, S., and Burke, R. D., 2017, "Characterisation and Optimisation of a Real-Time Diesel Engine Model," Proceedings of the Institution of Mechanical Engineers, Part D: Journal of Automobile Engineering, 231(14), pp. 1913–1934.

[104] Hendricks, E., and Sorenson, S. C., 1990, "Mean Value Modelling of Spark Ignition Engines," SAE Technical Paper No. 900616.

[105] Hunt, G., Truscott, A., and Noble, A., 2004, "An In-Cycle Hardware in the Loop (HiL) Simulator for Future Engine Control Strategy Development," SAE Technical Paper No. 2004-01-0418.

[106] "GT-POWER Engine Simulation Software," Gamma Technologies [Online]. Available: https://www.gtisoft.com/gt-suite-applications/propulsion-systems/gt-power-engine-simulation-software/. [Accessed: 31-Jul-2018].

[107] Ortiz-Soto, E. A., Lavoie, G. A., Wooldridge, M. S., and Assanis, D. N., 2018, "Thermodynamic Efficiency Assessment of Gasoline Spark Ignition and Compression Ignition Operating Strategies Using a New Multi-Mode Combustion Model for Engine System Simulations," International Journal of Engine Research, p. 1468087417752195.

[108] Deb, K., and Jain, H., 2014, "An Evolutionary Many-Objective Optimization Algorithm Using Reference-Point-Based Nondominated Sorting Approach, Part I: Solving Problems With Box Constraints," IEEE Transactions on Evolutionary Computation, 18(4), pp. 577–601.

[109] "Horsepower Required for Compressing Air," Womack Machine Supply Company [Online]. Available: https://www.womackmachine.com/engineering-toolbox/data-sheets/horsepower-required-for-compressing-air/. [Accessed: 19-Sep-2018].

[110] Tolou, S., Vedula, R. T., Schock, H., Zhu, G., Sun, Y., and Kotrba, A., 2018, "Combustion Model for a Homogeneous Turbocharged Gasoline Direct-Injection Engine," J. Eng. Gas Turbines Power, 140(10), pp. 102804-102804–10.

[111] Lavoie, G. A., Ortiz-Soto, E., Babajimopoulos, A., Martz, J. B., and Assanis, D. N., 2013, "Thermodynamic Sweet Spot for High-Efficiency, Dilute, Boosted Gasoline Engines," International Journal of Engine Research, 14(3), pp. 260–278.

[112] "Pickup Artist: How The Ford F-Series Took Over America," NPR.org [Online]. Available: https://www.npr.org/2018/09/12/647158228/pickup-artist-how-the-ford-f-series-took-over-america. [Accessed: 09-Jan-2019].

[113] "Ford F-150: The Most Fuel-Efficient Full-Size Truck—But Not For Long," Observer [Online]. Available: https://observer.com/2018/06/ford-f-150-the-most-fuel-efficient-full-size-truck-but-not-for-long/. [Accessed: 09-Jan-2019].

[114] "2019 Ford® F-150 Truck | Power Features | Ford.Com," Ford Motor Companies [Online]. Available:

https://www.ford.com/trucks/f150/features/power/#2_7_turbocharged_ecoboost. [Accessed: 13-Dec-2018].

[115] "Advanced Light-Duty Powertrain and Hybrid Analysis (ALPHA) Tool," U.S. Environmental Protection Agency [Online]. Available: https://www.epa.gov/regulations-emissions-vehicles-and-engines/advanced-light-duty-powertrain-and-hybrid-analysis-alpha. [Accessed: 08-Aug-2018].

[116] Dekraker, P., Stuhldreher, M., and Kim, Y., 2017, "Characterizing Factors Influencing SI Engine Transient Fuel Consumption for Vehicle Simulation in ALPHA," SAE International Journal of Engines, 10(2), pp. 529–540.

[117] "Surface Fitting Using Gridfit," MathWorks, MATLAB Central, File Exchange [Online]. Available: https://www.mathworks.com/matlabcentral/fileexchange/8998-surface-fitting-using-gridfit. [Accessed: 09-Jan-2019].

[118] Chen, S. K., and Flynn, P. F., 1965, "Development of a Single Cylinder Compression Ignition Research Engine," SAE Technical Paper No. 650733.

[119] de O. Carvalho, L., de Melo, T. C. C., and de Azevedo Cruz Neto, R. M., 2012, "Investigation on the Fuel and Engine Parameters That Affect the Half Mass Fraction Burned (CA50) Optimum Crank Angle," SAE Technical Paper No. 2012-36-0498.

[120] Zhu, G. G., Daniels, C. F., and Winkelman, J., 2003, "MBT Timing Detection and Its Closed-Loop Control Using In-Cylinder Pressure Signal," SAE Technical Paper No. 2003-01-3266.

[121] Ma, F., Wang, Y., Wang, J., Ding, S., Wang, Y., and Zhao, S., 2008, "Effects of Combustion Phasing, Combustion Duration, and Their Cyclic Variations on Spark-Ignition (SI) Engine Efficiency," Energy Fuels, 22(5), pp. 3022–3028.

[122] Barba, D., 2016, "ALPHA Effectiveness Modeling: Current and Future Light-Duty Vehicle & Powertrain Technologies."

[123] Dekraker, P., Kargul, J., Moskalik, A., Newman, K., Doorlag, M., and Barba, D., 2017, "Fleet-Level Modeling of Real World Factors Influencing Greenhouse Gas Emission Simulation in ALPHA," SAE International Journal of Fuels and Lubricants, 10(1), pp. 217–235.

[124] "Dynamometer Drive Schedules," U.S. Environmental Protection Agency [Online]. Available: https://www.epa.gov/vehicle-and-fuel-emissions-testing/dynamometer-drive-schedules. [Accessed: 20-Dec-2018].

[125] Carley, S., Duncan, D., Graham, J. D., Siddiki, S., and Zirogiannis, N., 2017, A Macroeconomic Study of Federal and State Automotive Regulations with Recommendations for Analysts, Regulators, and Legislators, Indiana University, School of Public and Environmental Affairs.

[126] 2018, "Annual Energy Outlook 2018 | Table: Petroleum and Other Liquid Prices," U.S. Energy Information Administration [Online]. Available: https://www.eia.gov/outlooks/aeo/data/browser/#/?id=12-AEO2018&region=0-0&cases=ref2018&start=2016&end=2050&f=A&linechart=~ref2018-d121317a.30-12-AEO2018&map=&ctype=linechart&sourcekey=0. [Accessed: 20-Dec-2018].

[127] "Table 1.1.9. Implicit Price Deflators for Gross Domestic Product: Quarterly" FRED, Economic Research, Federal Reserve Bank of ST.LOUIS [Online]. Available: https://fred.stlouisfed.org/release/tables?rid=53&eid=13116. [Accessed: 20-Dec-2018].

[128] McAlinden S., Baron, J., Chen, Y., 2011, "The U.S. Automotive Market and Industry in 2025," Center for Automotive Research.

[129] National Research Council, 2015, Cost, Effectiveness, and Deployment of Fuel Economy Technologies for Light-Duty Vehicles, The National Academies Press, Washington, D.C.

[130] Helfand, G., and Wolverton, A., 2011, "Evaluating the Consumer Response to Fuel Economy: A Review of the Literature," National Center for Environmental Economics.

[131] 2010, "Technical Support Document: - Social Cost of Carbon for Regulatory Impact Analysis - Under Executive Order 12866-," Interagency Working Group on Social Cost of Carbon, U.S. Government [online]. Available: https://www.epa.gov/sites/production/files/2016-12/documents/scc_tsd_2010.pdf. [Accessed: 07-Aug-2018].

[132] 2013, "Technical Support Document: - Technical Update of the Social Cost of Carbon for Regulatory Impact Analysis - Under Executive Order 12866-," Interagency Working Group on Social Cost of Carbon, U.S. Government [online]. Available: https://environblog.jenner.com/files/technical-update-of-the-social-cost-of-carbon-for-regulatory-impact-analysis-under-executive-order-12866.pdf. [Accessed: 07-Aug-2018].

[133] National Academies of Sciences, Engineering, Medicine, 2017, Valuing Climate Damages: Updating Estimation of the Social Cost of Carbon Dioxide, The National Academies Press, Washington, D.C.

[134] 2017, "82 FR 16093 - Promoting Energy Independence and Economic Growth," Executive Office of the President [online]. Available: file:///C:/Users/toloused.ME639/Zotero/storage/ZT8ZUZ26/promoting-energy-independence-and-economic-growth.html/. [Accessed: 07-Aug-2018].

[135] 2017, "EPA-452/R-17-004 | Regulatory Impact Analysis for the Review of the Clean Power Plan: Proposal," U.S. Environmental Protection Agency, Office of Air Quality Planning and Standards, Health and Environmental Impacts Division [online]. Available: https://www.epa.gov/sites/production/files/2017-10/documents/ria_proposed-cpp-repeal_2017-10_0.pdf. [Accessed: 07-Aug-2018].

[136] Mooney, C., 2017, "New EPA Document Reveals Sharply Lower Estimate of the Cost of Climate Change," The Washington Post [Online]. Available:

https://www.washingtonpost.com/news/energy-environment/wp/2017/10/11/new-epa-document-reveals-sharply-lower-estimate-of-the-cost-of-climate-change/. [Accessed: 07-Aug-2018].